Molecular Simulation and Integral Equation Studies of the Solute-Solute Effective Interactions in Water and Simple Liquids

March, 2025

Hidefumi NAITO

Graduate School of Natural Science and Technology
(Doctor's Cource)

OKAYAMA UNIVERSITY

Contents

Chapter 1

General Introduction

1.1 BACKGROUND

This thesis aims to gain a detailed understanding of the nature of intermolecular interactions in solutions.

Intermolecular interactions between solute molecules in a solvent are qualitatively different from those in a vacuum.[1] The difference between them is due to the solvent-induced interaction. The direct pair interaction between atoms or molecules in a vacuum is modeled by several analytical expressions, such as the square-well, Morse, and Lennard-Jones potentials, with a few parameters. However, it is difficult to express the solute-solute effective potential analytically because the strength of the effective interaction depends on several factors, for example, temperature, pressure, salt concentration, molecular size, molecular shape, and solvent species. Numerous experimental and simulation studies have thus been done to elucidate the nature of the solute-solute effective interaction.

When the solvent is water, and the solute molecule is hydrophobic, i.e., poorly soluble in water, the solute-solute effective interaction is referred to as the hydrophobic interaction. Amphiphilic molecules (surfactants, phospholipids, $\cdots$) also interact with each other via the hydrophobic interaction between their nonpolar groups. This interaction is the driving forces for the formation of various aggregates by surfactant molecules, such as spherical and rod micelles, vesicles, and flat lamellae, and for the formation of lipid bilayers by phospholipids.

It had long been recognized that the hydrophobic interaction was the dominant factor in stabilizing the folded configurations of proteins. This idea originated from an article in 1959 by Kauzmann.[2] At that time, the hydrophobic interaction was called the hydrophobic bond. He first concluded that *"hydrogen bonds, taken by themselves* (= proteins), *give a marginal stability to ordered structures, which may be enhanced or disrupted by interactions of side-chains"* (W. Kauzmann, Adv. Protein Chem., 1959). Then, he speculated that *"the hydrophobic bond is probably one of the more important factors involved in stabilizing the folded configuration in many native proteins"* (W. Kauzmann, Adv. Protein Chem., 1959) since most of the hydrophobic parts of proteins are inside the folded protein structure.

Ben-Naim doubted the importance of hydrophobic interactions in the structural stability of proteins. He analyzed in detail all the possible solvent-induced interactions between hydrophobic groups, hydrophilic groups, and hydrophobic and hydrophilic groups. As a result, he indicated that the solvent-induced interaction involving the hydrophilic groups might be more crucial in protein folding[1] because *"1. Direct HBs (= hydrogen bonds) between two HϕI (= hydrophilic) groups had a significant Gibbs energy change (not insignificant as concluded by Kauzmann and many others)."* and *"2. Some experimental results indicated that SII (= solvent-induced interactions) between HϕI groups might be very strong, perhaps even stronger than the corresponding interaction between two HϕO (= hydrophobic) groups"* (A. Ben-Naim, Springer Nature, 2023). The effective interaction between polar moieties of amphiphilic molecules in water is called the hydrophilic interaction. In any case, the solvent-induced interaction has significant effects on protein folding.

As mentioned above, the strength of solute-solute effective interactions in a solvent depends on various thermodynamic and microscopic factors. The present work focuses on the effect of solute size. Here, we enumerate the previous studies. Lum, Chandler, and Weeks found the crossover occurring in the particle size effect on the solvation of hard-sphere particles in water on nanometer length scales ($\simeq$ 1 nm):[3] For large particles, the solvation free energy μ^* is proportional to the surface area of the particle. On the other hand, for small particles, μ^*, scaled by the surface area, varies rapidly as a function of particle radius. They also calculated the free energy for water confined by two hard plates and showed that the drying transition between the plate surfaces derives strong between them.[3]

Scheraga et al. measured the effective potential for hydrocarbon pairs of different sizes in water.[4], [5] They indicated that the solvent-induced interaction in water is attractive for small-sized solutes, while it becomes repulsive for large-sized solutes such as C_{60} fullerene (its diameter is about 1 nm). Zangi also calculated the free energy profile for a pair of graphene sheets in water as a function of the distance between two sheets.[6] They clarified that the driving force of the association of small sheets is the entropy change. In contrast,

that of large sheets is the enthalpy change. These studies make clear that the nature of the inter-solute effective pair interaction is different for small and large solutes.

The objective of this study is to understand how the strength of the solvent-induced interaction varies with solute size and clarify the thermodynamic and microscopic factors determining its size dependence. The remainder of this chapter is organized as follows. Section 1.2 presents several statistical mechanical equations used in the later chapters. Section 1.3 shows the outline of the rest of the thesis, which consists of four chapters.

1.2 THEORETICAL BACKGROUND

At least there are two approaches to quantify the strength of the solute-solute effective interaction in a solvent: One is the potential $w(r)$ of mean force, and the other is the osmotic second virial coefficient B. This section first demonstrates the statistical mechanical expression of $w(r)$, which is defined by the radial distribution function. We can interpret that the effective potential $w(r)$ is the free energy change in decreasing the solute-solute distance from infinite separation to the specific distance r. Second, we derive the statistical mechanical formula of B based on the Kirkwood-Buff theory of solution.[7] The derivations described below are based on the references by Ben-Naim.[1], [8]

1.2.1 Radial Distribution Function and Potential of Mean Force

Firstly, we introduce the concepts of the radial distribution function and the potential of mean force. For simplicity, we consider a canonical ensemble consisting of N spherical particles in a system with a fixed volume V at a constant temperature T. The coordinate of the particle i is described by $\boldsymbol{r_i} = (x_i, y_i, z_i)$.

The probability density $Pr(\boldsymbol{r}_1, \boldsymbol{r}_2, \cdots, \boldsymbol{r}_N)$ of finding N particles at a particular configuration $\boldsymbol{r}_1, \boldsymbol{r}_2, \cdots, \boldsymbol{r}_N$ is expressed as

$$Pr(\boldsymbol{r}_1, \boldsymbol{r}_2, \cdots, \boldsymbol{r}_N) = \frac{\exp\left[-\beta U_N(\boldsymbol{r}_1, \boldsymbol{r}_2, \cdots, \boldsymbol{r}_N)\right]}{\int\int\cdots\int \exp\left[-\beta U_N(\boldsymbol{r}_1, \boldsymbol{r}_2, \cdots, \boldsymbol{r}_N)\right] d\boldsymbol{r}_1 d\boldsymbol{r}_2 \cdots d\boldsymbol{r}_N}, \tag{1.1}$$

where β is the inverse temperature $1/kT$, k is Boltzmann's constant, $U_N(\boldsymbol{r}_1, \boldsymbol{r}_2, \cdots, \boldsymbol{r}_N)$

is the total potential energy of the interactions between all the N particles, and $d\boldsymbol{r}_i$ is an infinitesimal volume element for the particle i. In the following discussion, we denote $\boldsymbol{r}_1, \boldsymbol{r}_2, \cdots, \boldsymbol{r}_N$ as $\boldsymbol{r}^N$ and $d\boldsymbol{r}_1 d\boldsymbol{r}_2 \cdots d\boldsymbol{r}_N$ as $d\boldsymbol{r}^N$.

Here, we consider the probability density $P^{(1)}(\boldsymbol{r}_1)$ of finding the specific particle "1" at the particular location $\boldsymbol{r}_1$. It is obtained by integrating $Pr(\boldsymbol{r}^N)$ over the configurations of the remaining $N-1$ particles:

$$P^{(1)}(\boldsymbol{r}_1) = \int \cdots \int Pr(\boldsymbol{r}^N) d\boldsymbol{r}_2 \cdots d\boldsymbol{r}_N. \tag{1.2}$$

$P^{(1)}(\boldsymbol{r}_1)d\boldsymbol{r}_1$ is the probability of finding the particle "1" at $\boldsymbol{r}_1$ in the volume element $d\boldsymbol{r}_1$.

The probability $P^{(1)}(\boldsymbol{r}_i)d\boldsymbol{r}_i$ is not depend on the notation i because all the particles in the one-component system are identical. Therefore, the probability density $\rho^{(1)}(\boldsymbol{r}')$ of finding any particle at the location $\boldsymbol{r}'$ is $P^{(1)}(\boldsymbol{r}')$ times the number N of particles:

$$\rho^{(1)}(\boldsymbol{r}') = NP^{(1)}(\boldsymbol{r}') = N \int \cdots \int Pr(\boldsymbol{r}', \boldsymbol{r}_2, \cdots, \boldsymbol{r}_N) d\boldsymbol{r}_2 \cdots d\boldsymbol{r}_N. \tag{1.3}$$

Clearly, $\rho^{(1)}(\boldsymbol{r}')d\boldsymbol{r}'$ is the probability of finding any particle at $\boldsymbol{r}'$ in $d\boldsymbol{r}'$.

The normalization condition for $\rho^{(1)}(\boldsymbol{r}')$ is

$$\int \rho^{(1)}(\boldsymbol{r}') d\boldsymbol{r}' = N \int P^{(1)}(\boldsymbol{r}') d\boldsymbol{r}' = N \tag{1.4}$$

because the probability of finding the specific particle in the system is unity, i.e., $\int P^{(1)}(\boldsymbol{r}')d\boldsymbol{r}' = \int Pr(\boldsymbol{r}^N)d\boldsymbol{r}^N = 1$. For a homogeneous fluid, $\rho^{(1)}(\boldsymbol{r}')$ takes the same value at any $\boldsymbol{r}'$. In this case,

$$\rho^{(1)}(\boldsymbol{r}') = \frac{N}{\int d\boldsymbol{r}'} = \frac{N}{V} = \rho. \tag{1.5}$$

Eq. (1.5) implies that $\rho^{(1)}(\boldsymbol{r}')$ for a homogeneous fluid is equal to the bulk density ρ.

Next, we discuss the pair distribution function. As well as the expression for $P^{(1)}(\boldsymbol{r}')$, the probability density $P^{(2)}(\boldsymbol{r}', \boldsymbol{r}'')$ of finding the specific particle "1" at the location $\boldsymbol{r}'$

and the other specific particle "2" at $\boldsymbol{r}''$ is

$$P^{(2)}(\boldsymbol{r}', \boldsymbol{r}'') = \int \cdots \int Pr(\boldsymbol{r}', \boldsymbol{r}'', \boldsymbol{r}_3, \cdots, \boldsymbol{r}_N) d\boldsymbol{r}_3 \cdots d\boldsymbol{r}_N. \tag{1.6}$$

$P^{(2)}(\boldsymbol{r}', \boldsymbol{r}'')d\boldsymbol{r}'d\boldsymbol{r}''$ is the probability of finding the particles "1" and "2" at the locations $\boldsymbol{r}'$ and $\boldsymbol{r}''$ in the volume elements $d\boldsymbol{r}'$ and $d\boldsymbol{r}''$.

The probability $P^{(2)}(\boldsymbol{r}', \boldsymbol{r}'')d\boldsymbol{r}'d\boldsymbol{r}''$ is the same for any pair of particles because the one-component system consists of all identical particles. The number of events of finding a particle in $d\boldsymbol{r}'$ and another particle in $d\boldsymbol{r}''$ is ${}_N\mathrm{P}_2 = N(N-1)$. The probability of finding any particle at $\boldsymbol{r}'$ in $d\boldsymbol{r}'$ and any other particle at $\boldsymbol{r}''$ in $d\boldsymbol{r}''$ is thus given by

$$\rho^{(2)}(\boldsymbol{r}', \boldsymbol{r}'')d\boldsymbol{r}'d\boldsymbol{r}'' = N(N-1)P^{(2)}(\boldsymbol{r}', \boldsymbol{r}'')d\boldsymbol{r}'d\boldsymbol{r}''. \tag{1.7}$$

$$\rho^{(2)}(\boldsymbol{r}', \boldsymbol{r}'') = N(N-1) \int \cdots \int Pr(\boldsymbol{r}', \boldsymbol{r}'', \boldsymbol{r}_3, \cdots, \boldsymbol{r}_N) d\boldsymbol{r}_3 \cdots d\boldsymbol{r}_N. \tag{1.8}$$

Eq. (1.8) defines the pair distribution function $\rho^{(2)}(\boldsymbol{r}', \boldsymbol{r}'')$. The normalization condition for $\rho^{(2)}(\boldsymbol{r}', \boldsymbol{r}'')$ is

$$\int\int \rho^{(2)}(\boldsymbol{r}', \boldsymbol{r}'')d\boldsymbol{r}'d\boldsymbol{r}'' = N(N-1) \int\int P^{(2)}(\boldsymbol{r}', \boldsymbol{r}'')d\boldsymbol{r}'d\boldsymbol{r}'' = N(N-1) \tag{1.9}$$

because $\int\int P^{(2)}(\boldsymbol{r}', \boldsymbol{r}'')d\boldsymbol{r}'d\boldsymbol{r}'' = \int Pr(\boldsymbol{r}^N)d\boldsymbol{r}^N = 1$.

Now we consider the correlation between the two events: One is the event of finding a particle at $\boldsymbol{r}'$ in $d\boldsymbol{r}'$, and the other is the event of finding another particle at $\boldsymbol{r}''$ in $d\boldsymbol{r}''$. In general, the correlation $g(X, Y)$ between two events X and Y is defined as

$$g(X, Y) \equiv \frac{Pr(X \cap Y)}{Pr(X)Pr(Y)}, \tag{1.10}$$

where $Pr(X)$ and $Pr(Y)$ are the probabilities of two events X and Y, respectively, and $Pr(X \cap Y)$ is the probability of the intersection of these two events. When the two events are independent of each other, $Pr(X \cap Y) = Pr(X)Pr(Y)$. Therefore, $g(X, Y) = 1$ means no correlation between two events, X and Y.

Based on Eq. (1.10), the correlation $g(\boldsymbol{r}', \boldsymbol{r}'')$ between the event of finding a particle in $d\boldsymbol{r}'$ and that of finding another particle in $d\boldsymbol{r}''$ is

$$g(\boldsymbol{r}', \boldsymbol{r}'') = \frac{\rho^{(2)}(\boldsymbol{r}', \boldsymbol{r}'')d\boldsymbol{r}'d\boldsymbol{r}''}{\rho^{(1)}(\boldsymbol{r}')d\boldsymbol{r}'\rho^{(1)}(\boldsymbol{r}'')d\boldsymbol{r}''} = \frac{\rho^{(2)}(\boldsymbol{r}', \boldsymbol{r}'')}{\rho^{(1)}(\boldsymbol{r}')\rho^{(1)}(\boldsymbol{r}'')}. \tag{1.11}$$

$g(\boldsymbol{r}', \boldsymbol{r}'')$ is referred to as the pair correlation function. Two events are independent if the distance between two particles is infinite. In this case, the probability $\rho^{(2)}(\boldsymbol{r}', \boldsymbol{r}'')d\boldsymbol{r}'d\boldsymbol{r}''$ is equal to $\rho^{(1)}(\boldsymbol{r}')d\boldsymbol{r}'$ times $\rho^{(1)}(\boldsymbol{r}'')d\boldsymbol{r}''$, and so $g(\boldsymbol{r}', \boldsymbol{r}'') = 1$.

Finally, we show the definition of the radial distribution function. Consider the conditional probability $\rho(\boldsymbol{r}''|\boldsymbol{r}')d\boldsymbol{r}''$ of finding a particle at the location $\boldsymbol{r''}$ in the volume element $d\boldsymbol{r}''$ under the condition that there is a particle at $\boldsymbol{r}'$ in $d\boldsymbol{r}'$. This conditional probability is defined as

$$\rho(\boldsymbol{r}''|\boldsymbol{r}')d\boldsymbol{r}'' \equiv \frac{\rho^{(2)}(\boldsymbol{r}', \boldsymbol{r}'')d\boldsymbol{r}'d\boldsymbol{r}''}{\rho^{(1)}(\boldsymbol{r}')d\boldsymbol{r}'} = \rho^{(1)}(\boldsymbol{r}'')g(\boldsymbol{r}', \boldsymbol{r}'')d\boldsymbol{r}''. \tag{1.12}$$

When the system is homogeneous and isotropic, $\rho^{(1)}(\boldsymbol{r}'')$ reduces to the bulk density ρ. This system also holds the translational invariance, which allows taking the coordinate $\boldsymbol{r}'$ of one particle as the origin of the other coordinates $\boldsymbol{r}'', \boldsymbol{r}_3, \cdots, \boldsymbol{r}_N$ of the remaining $N-1$ particles. Therefore, the argument of $g(\boldsymbol{r}', \boldsymbol{r}'')$ and $\rho(\boldsymbol{r}''|\boldsymbol{r}')$ can be changed from $\boldsymbol{r}', \boldsymbol{r}''$ to the single variable $r = |\boldsymbol{r}'' - \boldsymbol{r}'|$. Then,

$$g(r) = \frac{\rho(r)}{\rho}. \tag{1.13}$$

$\rho(r)$ is the density of particles apart from the particle at the origin as a function of the inter-particle distance r. Eq. (1.13) defines the radial distribution function $g(r)$ as the ratio of the local density $\rho(r)$ and the bulk density ρ.

Now, we extend the discussion from a one-component system to a two-component system consisting of solute and solvent particles. Consider a canonical ensemble of two solute particles and N solvent particles in a system of a fixed volume V at a constant temperature T. The coordinate of the solvent particle i is described by $\boldsymbol{r_i}$. The two solute

particles labeled by a and b are fixed at $\boldsymbol{r}_a$ and $\boldsymbol{r}_b$, respectively.

Here, we introduce the canonical partition function $Q(\boldsymbol{r}_a, \boldsymbol{r}_b)$ for our two-component system:

$$Q(\boldsymbol{r}_a, \boldsymbol{r}_b) = \frac{1}{h^{3N} N!} \int \int \exp\left[-\beta \left[\sum_{i=1}^{N} \frac{\boldsymbol{p}_i^2}{2m} + U(\boldsymbol{r}_a, \boldsymbol{r}_b, \boldsymbol{r}^N)\right]\right] d\boldsymbol{p}^N d\boldsymbol{r}^N, \tag{1.14}$$

where h is the Planck constant, $\boldsymbol{p}_i$ is the momentum of the solvent particle i, and m is the mass of a solvent particle. $\sum_{i=1}^{N} \frac{\boldsymbol{p}_i^2}{2m}$ is the total kinetic energy of all the solvent particles, and $U(\boldsymbol{r}_a, \boldsymbol{r}_b, \boldsymbol{r}^N)$ is the total potential energy of the interactions between all the solute and solvent particles.

In Eq. (1.14), the integration over the momenta $\boldsymbol{p}^N = (\boldsymbol{p}_1, \boldsymbol{p}_2, \cdots, \boldsymbol{p}_N)$ is independent of that over the configurations $\boldsymbol{r}^N$:

$$\begin{aligned}
&\int \exp\left[-\beta \sum_{i=1}^{N} \frac{\boldsymbol{p}_i^2}{2m}\right] d\boldsymbol{p}^N \\
&= \int \int \cdots \int \exp\left[-\frac{\boldsymbol{p}_1^2 + \boldsymbol{p}_2^2 + \cdots + \boldsymbol{p}_N^2}{2mkT}\right] d\boldsymbol{p}_1 d\boldsymbol{p}_2 \cdots d\boldsymbol{p}_N = \left[\int \exp\left[-\frac{\boldsymbol{p}_1^2}{2mkT}\right] d\boldsymbol{p}_1\right]^N \\
&= \left[\int_{-\infty}^{\infty} \int_{-\infty}^{\infty} \int_{-\infty}^{\infty} \exp\left[-\frac{p_{1x}^2 + p_{1y}^2 + p_{1z}^2}{2mkT}\right] dp_{1x} dp_{1y} dp_{1z}\right]^N = \left[\int_{-\infty}^{\infty} \exp\left[-\frac{p_{1x}^2}{2mkT}\right] dp_{1x}\right]^{3N} \\
&= \sqrt{2\pi mkT}^{\,3N}
\end{aligned} \tag{1.15}$$

with $\boldsymbol{p}_i = (p_{ix}, p_{iy}, p_{iz})$. Therefore,

$$Q(\boldsymbol{r}_a, \boldsymbol{r}_b) = \frac{1}{\lambda^{3N} N!} \int \exp\left[-\beta U(\boldsymbol{r}_a, \boldsymbol{r}_b, \boldsymbol{r}^N)\right] d\boldsymbol{r}^N, \tag{1.16}$$

where $\lambda = h/\sqrt{2\pi mkT}$ is the thermal de Broglie wavelength of the solvent particle.

The Helmholtz free energy $A(\boldsymbol{r}_a, \boldsymbol{r}_b)$ of the canonical system is related to the canonical partition function $Q(\boldsymbol{r}_a, \boldsymbol{r}_b)$ by

$$\begin{aligned}
A(\boldsymbol{r}_a, \boldsymbol{r}_b) &= -kT \ln Q(\boldsymbol{r}_a, \boldsymbol{r}_b) \\
&= -kT \ln \left[\int \exp\left[-\beta U(\boldsymbol{r}_a, \boldsymbol{r}_b, \boldsymbol{r}^N)\right] d\boldsymbol{r}^N\right] + kT \ln (\lambda^{3N} N!).
\end{aligned} \tag{1.17}$$

The remainder of this section demonstrates the expression and interpretation of the potential of mean force. The probability density $Pr(\boldsymbol{r}_a, \boldsymbol{r}_b)$ of finding two solute particles a and b at the locations $\boldsymbol{r}_a$ and $\boldsymbol{r}_b$ is

$$Pr(\boldsymbol{r}_a, \boldsymbol{r}_b) = \frac{\int \exp\bigl[-\beta U(\boldsymbol{r}_a, \boldsymbol{r}_b, \boldsymbol{r}^N)\bigr] d\boldsymbol{r}^N}{\int\int\int \exp\bigl[-\beta U(\boldsymbol{r}_a, \boldsymbol{r}_b, \boldsymbol{r}^N)\bigr] d\boldsymbol{r}_a d\boldsymbol{r}_b d\boldsymbol{r}^N}. \tag{1.18}$$

The pair correlation function $g(\boldsymbol{r}_a, \boldsymbol{r}_b)$ is now defined as

$$g(\boldsymbol{r}_a, \boldsymbol{r}_b) \equiv \frac{Pr(\boldsymbol{r}_a, \boldsymbol{r}_b) d\boldsymbol{r}_a d\boldsymbol{r}_b}{Pr(r_{ab} \to \infty) d\boldsymbol{r}_a d\boldsymbol{r}_b}, \tag{1.19}$$

where $Pr(r_{ab} \to \infty)$ is the probability density of finding two solute particles when the solute-solute separation $r_{ab} = |\boldsymbol{r}_b - \boldsymbol{r}_a|$ is infinite. We insert Eq. (1.18) into Eq. (1.19), then

$$g(\boldsymbol{r}_a, \boldsymbol{r}_b) = \frac{\int \exp\bigl[-\beta U(\boldsymbol{r}_a, \boldsymbol{r}_b, \boldsymbol{r}^N)\bigr] d\boldsymbol{r}^N}{\int \exp\bigl[-\beta U(r_{ab} \to \infty, \boldsymbol{r}^N)\bigr] d\boldsymbol{r}^N}. \tag{1.20}$$

Here, we consider the mean force $\langle F_a \rangle$ acting on the particle a in the two-component solution when the locations of two solute particles a and b are fixed at $\boldsymbol{r}_a$ and $\boldsymbol{r}_b$, respectively. $\langle F_a \rangle$ is the ensemble average of the force $F_a = -\nabla_a U(\boldsymbol{r}_a, \boldsymbol{r}_b, \boldsymbol{r}^N)$:

$$\begin{aligned} \langle F_a \rangle &= \frac{\int \bigl[-\nabla_a U(\boldsymbol{r}_a, \boldsymbol{r}_b, \boldsymbol{r}^N)\bigr] \exp\bigl[-\beta U(\boldsymbol{r}_a, \boldsymbol{r}_b, \boldsymbol{r}^N)\bigr] d\boldsymbol{r}^N}{\int \exp\bigl[-\beta U(\boldsymbol{r}_a, \boldsymbol{r}_b, \boldsymbol{r}^N)\bigr] d\boldsymbol{r}^N} \\ &= \nabla_a \left\{ \frac{1}{\beta} \ln \left[\int \exp\bigl[-\beta U(\boldsymbol{r}_a, \boldsymbol{r}_b, \boldsymbol{r}^N)\bigr] d\boldsymbol{r}^N \right] \right\}, \end{aligned} \tag{1.21}$$

where ∇_a is the differentiation with respect to $\boldsymbol{r}_a$.

The potential $w(\boldsymbol{r}_a, \boldsymbol{r}_b)$, which gives the mean force by $\langle F_a \rangle = -\nabla_a w(\boldsymbol{r}_a, \boldsymbol{r}_b)$, is now

$$w(\boldsymbol{r}_a, \boldsymbol{r}_b) = -kT \ln \left[\int \exp\bigl[-\beta U(\boldsymbol{r}_a, \boldsymbol{r}_b, \boldsymbol{r}^N)\bigr] d\boldsymbol{r}^N \right] + f(\boldsymbol{r}_b) \tag{1.22}$$

with $f(\boldsymbol{r}_b)$ being an arbitrary function of $\boldsymbol{r}_b$. Inserting Eq. (1.20) into Eq. (1.22) derives

the relationship between $w(\boldsymbol{r}_a, \boldsymbol{r}_b)$ and $g(\boldsymbol{r}_a, \boldsymbol{r}_b)$:

$$\begin{aligned} w(\boldsymbol{r}_a, \boldsymbol{r}_b) &= -kT \ln \left[g(\boldsymbol{r}_a, \boldsymbol{r}_b) \int \exp\left[-\beta U(r_{ab} \to \infty, \boldsymbol{r}^N)\right] d\boldsymbol{r}^N \right] + f(\boldsymbol{r}_b) \\ &= -kT \ln g(\boldsymbol{r}_a, \boldsymbol{r}_b) - kT \ln \left[\int \exp\left[-\beta U(r_{ab} \to \infty, \boldsymbol{r}^N)\right] d\boldsymbol{r}^N \right] + f(\boldsymbol{r}_b) \\ &= -kT \ln g(\boldsymbol{r}_a, \boldsymbol{r}_b) + w(r_{ab} \to \infty). \end{aligned} \tag{1.23}$$

In Eq. (1.23), $w(r_{ab} \to \infty)$ is the potential represented by Eq. (1.22) when the separation between two particles a and b is infinite. If we set $w(r_{ab} \to \infty) = 0$, then

$$w(\boldsymbol{r}_a, \boldsymbol{r}_b) = -kT \ln g(\boldsymbol{r}_a, \boldsymbol{r}_b). \tag{1.24}$$

$w(\boldsymbol{r}_a, \boldsymbol{r}_b)$ is the potential of mean force for pairs of solute particles a and b.

Eq. (1.24) can be rewritten by combining it with Eqs. (1.20) and (1.17) as

$$\begin{aligned} w(\boldsymbol{r}_a, \boldsymbol{r}_b) &= -kT \ln \left[\frac{\int \exp\left[-\beta U(\boldsymbol{r}_a, \boldsymbol{r}_b, \boldsymbol{r}^N)\right] d\boldsymbol{r}^N}{\int \exp\left[-\beta U(r_{ab} \to \infty, \boldsymbol{r}^N)\right] d\boldsymbol{r}^N} \right] \\ &= \left\{ -kT \ln \left[\int \exp\left[-\beta U(\boldsymbol{r}_a, \boldsymbol{r}_b, \boldsymbol{r}^N)\right] d\boldsymbol{r}^N \right] + kT \ln\left(\lambda^{3N} N!\right) \right\} \\ &\quad - \left\{ -kT \ln \left[\int \exp\left[-\beta U(r_{ab} \to \infty, \boldsymbol{r}^N)\right] d\boldsymbol{r}^N \right] + kT \ln\left(\lambda^{3N} N!\right) \right\} \\ &= A(\boldsymbol{r}_a, \boldsymbol{r}_b) - A(r_{ab} \to \infty), \end{aligned} \tag{1.25}$$

where $A(\boldsymbol{r}_a, \boldsymbol{r}_b)$ is the Helmholtz free energy of the two-component system consisting of N solvent particles and two solute particles a and b at fixed locations $\boldsymbol{r}_a$ and $\boldsymbol{r}_b$, respectively. Eq. (1.25) indicates that $w(\boldsymbol{r}_a, \boldsymbol{r}_b)$ is the free energy change when two solute particles approach each other from infinite separation to a fixed configuration $\boldsymbol{r}_a, \boldsymbol{r}_b$, and $w(r_{ab} \to \infty)$ in Eq. (1.23) is actually zero because $A(r_{ab} \to \infty) - A(r_{ab} \to \infty) = 0$.

When the two-component system is homogeneous and isotropic, Eq. (1.24) reduces to

$$w(r) = -kT \ln g(r) \tag{1.26}$$

with $r = r_{ab} = |\boldsymbol{r}_b - \boldsymbol{r}_a|$. $g(r)$ is the radial distribution function for pairs of solute particles

in a solvent.

1.2.2 Kirkwood-Buff Theory

The Kirkwood-Buff theory is one of the most important theories of liquids. It relates several thermodynamic quantities to the Kirkwood-Buff (KB) integral in the grand canonical ensemble.[7] The KB integral G_{ij} is defined as

$$G_{ij} \equiv \int \left[\overline{g_{ij}(r)} - 1\right] d\boldsymbol{r}, \tag{1.27}$$

where $\overline{g_{ij}(r)}$ is the radial distribution function for a pair of species i and j in the grand canonical system.

In the previous section, we considered the canonical ensemble consisting of N identical particles. Recall that the normalization conditions for $\rho^{(1)}(\boldsymbol{r}')$ and $\rho^{(2)}(\boldsymbol{r}', \boldsymbol{r}'')$ in the canonical system are

$$\int \rho^{(1)}(\boldsymbol{r}') d\boldsymbol{r}' = N \tag{1.28}$$

and

$$\int \int \rho^{(2)}(\boldsymbol{r}', \boldsymbol{r}'') d\boldsymbol{r}' d\boldsymbol{r}'' = N(N-1), \tag{1.29}$$

respectively.

Now, we extend the discussion from the canonical one-component system to the grand canonical two-component system consisting of solvent and solute molecules. The latter system is characterized by the thermodynamic variables V, T, μ_1, and μ_2, where μ_1 and μ_2 are the chemical potentials of the solvent and the solute, respectively.

This section presents the three expressions for the thermodynamic quantities in terms of the KB integral; the isothermal compressibility of the pure solvent, the partial molecular volume of the solute at infinite dilution, and the osmotic second virial coefficient. We will use these expressions in later chapters.

By analogy with Eq. (1.28), the normalization condition for $\overline{\rho_i^{(1)}(\boldsymbol{r}')}$ of the molecular

species i in the grand canonical system is

$$\int \overline{\rho_i^{(1)}(\boldsymbol{r}')} d\boldsymbol{r}' = \langle N_i \rangle, \tag{1.30}$$

where N_i is the number of the molecule i. $\langle \cdots \rangle$ means an average in the grand canonical ensemble. The normalization condition for the pair distribution function $\overline{\rho_{ij}^{(2)}(\boldsymbol{r}', \boldsymbol{r}'')}$ for pairs of molecular species i and j in the grand canonical system is also an analog of Eq. (1.29):

$$\begin{aligned} \int \int \overline{\rho_{ij}^{(2)}(\boldsymbol{r}', \boldsymbol{r}'')} d\boldsymbol{r}' d\boldsymbol{r}'' &= \begin{cases} \langle N_i N_j \rangle & \text{if } i \neq j \\ \langle N_i (N_i - 1) \rangle & \text{if } i = j \end{cases} \\ &= \langle N_i N_j \rangle - \langle N_i \rangle \delta_{ij}, \end{aligned} \tag{1.31}$$

where δ_{ij} is the Kronecker delta function.

The pair correlation function $\overline{g_{ij}(\boldsymbol{r}', \boldsymbol{r}'')}$ for pairs of species i and j in the grand canonical ensemble is defined by $\overline{\rho_i^{(1)}(\boldsymbol{r}')}$ and $\overline{\rho_{ij}^{(2)}(\boldsymbol{r}', \boldsymbol{r}'')}$ as

$$\overline{g_{ij}(\boldsymbol{r}', \boldsymbol{r}'')} \equiv \frac{\overline{\rho_{ij}^{(2)}(\boldsymbol{r}', \boldsymbol{r}'')} d\boldsymbol{r}' d\boldsymbol{r}''}{\overline{\rho_i^{(1)}(\boldsymbol{r}')} d\boldsymbol{r}' \overline{\rho_j^{(1)}(\boldsymbol{r}'')} d\boldsymbol{r}''}. \tag{1.32}$$

This equation is similar to Eq. (1.11) in the canonical ensemble. When the system is homogeneous and isotropic, $\overline{\rho_i^{(1)}(\boldsymbol{r}')}$ is equal to the average number density $\rho_i = \langle N_i \rangle / V$ of the molecule i. In the same system, $\overline{\rho_{ij}^{(2)}(\boldsymbol{r}', \boldsymbol{r}'')}$ and $\overline{g_{ij}(\boldsymbol{r}', \boldsymbol{r}'')}$ are the functions of the single parameter $r = |\boldsymbol{r}'' - \boldsymbol{r}'|$, and Eq. (1.32) reduces to

$$\overline{\rho_{ij}^{(2)}(r)} = \rho_i \rho_j \overline{g_{ij}(r)}. \tag{1.33}$$

$\overline{g_{ij}(r)}$ is the radial distribution function for pairs of molecular species i and j in the grand canonical ensemble.

Here, we take the following difference

$$\Delta \equiv \int\int \overline{\rho_{ij}^{(2)}(\boldsymbol{r}', \boldsymbol{r}'')} d\boldsymbol{r}' d\boldsymbol{r}'' - \int \overline{\rho_i^{(1)}(\boldsymbol{r}')} d\boldsymbol{r}' \int \overline{\rho_j^{(1)}(\boldsymbol{r}'')} d\boldsymbol{r}''. \tag{1.34}$$

Substituting Eqs. (1.30) and (1.31) into Eq. (1.34) gives

$$\Delta = \langle N_i N_j \rangle - \langle N_i \rangle \langle N_j \rangle - \langle N_i \rangle \delta_{ij}. \tag{1.35}$$

We also combine Eq. (1.34) with $\overline{\rho_i^{(1)}(\boldsymbol{r}')} = \rho_i$ and Eq. (1.33) to obtain Δ for the homogeneous and isotropic system:

$$\Delta = \int\int \Big[\rho_i \rho_j \overline{g_{ij}(r)} - \rho_i \rho_j\Big] d\boldsymbol{r}' d\boldsymbol{r}'' = \rho_i \rho_j V \int \Big[\overline{g_{ij}(r)} - 1\Big] d\boldsymbol{r} \tag{1.36}$$

with $\boldsymbol{r} = \boldsymbol{r}'' - \boldsymbol{r}'$.

Eqs. (1.35) and (1.36) show that the fluctuation in the number of molecules, i.e., $\langle N_i N_j \rangle - \langle N_i \rangle \langle N_j \rangle$, is related to the KB integral $G_{ij} = \int [\overline{g_{ij}(r)} - 1] d\boldsymbol{r}$ by

$$\frac{\langle N_i N_j \rangle - \langle N_i \rangle \langle N_j \rangle}{V} = \rho_i \rho_j G_{ij} + \rho_i \delta_{ij}. \tag{1.37}$$

Next, we relate $\langle N_i N_j \rangle - \langle N_i \rangle \langle N_j \rangle$ to the thermodynamic quantity. The thermodynamic potential in the grand canonical ensemble is the grand potential from which all the thermodynamic quantities can be derived. This potential is related to the grand canonical partition function. For our system, the partition function $\Xi(\mu_1, \mu_2)$ is given by

$$\Xi(\mu_1, \mu_2) = \sum_{N_1=0}^{\infty} \sum_{N_2=0}^{\infty} Q(N_1, N_2) \exp\big[\beta(\mu_1 N_1 + \mu_2 N_2)\big], \tag{1.38}$$

where $Q(N_1, N_2)$ is the canonical partition function for the system consisting of N_1 solvent molecules and N_2 solute molecules. The grand potential $\Omega(\mu_1, \mu_2)$ is then

$$\Omega(\mu_1, \mu_2) = -kT \ln \Xi(\mu_1, \mu_2). \tag{1.39}$$

Now, we consider the average number $\langle N_i \rangle$ of the molecule i in the two-component system. The statistical mechanical formula for $\langle N_i \rangle$ is the ensemble average:

$$\langle N_i \rangle = \frac{1}{\Xi(\mu_1, \mu_2)} \sum_{N_1=0}^{\infty} \sum_{N_2=0}^{\infty} N_i Q(N_1, N_2) \exp\left[\beta(\mu_1 N_1 + \mu_2 N_2)\right], \tag{1.40}$$

and the thermodynamic expression is

$$\langle N_i \rangle = -\left[\frac{\partial \Omega(\mu_1, \mu_2)}{\partial \mu_i}\right]_{V,T,\mu_{j\neq i}} = \frac{kT}{\Xi(\mu_1, \mu_2)} \left[\frac{\partial \Xi(\mu_1, \mu_2)}{\partial \mu_i}\right]_{V,T,\mu_{j\neq i}}. \tag{1.41}$$

Here, we define the following quantity I_{ij}, including the differentiation of $\langle N_i \rangle$ with respect to μ_j:

$$I_{ij} \equiv \frac{kT}{V}\left[\frac{\partial \langle N_i \rangle}{\partial \mu_j}\right]_{V,T,\mu_{k\neq j}} = kT\left[\frac{\partial \rho_i}{\partial \mu_j}\right]_{T,\mu_{k\neq j}}. \tag{1.42}$$

This equation can be rewritten as

$$\begin{aligned}
I_{ij} &= \frac{kT}{V\Xi} \sum_{N_1} \sum_{N_2} N_i Q \left[\frac{\partial\big(\exp\left[\beta(\mu_1 N_1 + \mu_2 N_2)\right]\big)}{\partial \mu_j}\right]_{V,T,\mu_{k\neq j}} \\
&\quad + \frac{kT}{V}\left[\frac{\partial(1/\Xi)}{\partial \mu_j}\right]_{V,T,\mu_{k\neq j}} \sum_{N_1} \sum_{N_2} N_i Q \exp\left[\beta(\mu_1 N_1 + \mu_2 N_2)\right] \\
&= \frac{1}{V\Xi} \sum_{N_1} \sum_{N_2} N_i N_j Q \exp\left[\beta(\mu_1 N_1 + \mu_2 N_2)\right] \\
&\quad - \frac{1}{V\Xi} \sum_{N_1} \sum_{N_2} N_i Q \exp\left[\beta(\mu_1 N_1 + \mu_2 N_2)\right] \times \frac{kT}{\Xi}\left[\frac{\partial \Xi}{\partial \mu_j}\right]_{V,T,\mu_{k\neq j}} \\
&= \frac{\langle N_i N_j \rangle - \langle N_i \rangle \langle N_j \rangle}{V},
\end{aligned} \tag{1.43}$$

where $\langle N_i N_j \rangle$ is the ensemble average of the product $N_i N_j$.

We combine Eqs. (1.37) and (1.43) to obtain the relationship between the thermodynamic quantity I_{ij} and the KB integral G_{ij}:

$$I_{ij} = \rho_i \rho_j G_{ij} + \rho_i \delta_{ij}. \tag{1.44}$$

Now, we define the quantity I^{ij} to transform Eq. (1.44) from the condition at constant

chemical potential to that at constant number of molecules:

$$I^{ij} \equiv \frac{V}{kT}\left[\frac{\partial \mu_i}{\partial \langle N_j \rangle}\right]_{V,T,\langle N_{k\neq j}\rangle} = \frac{1}{kT}\left[\frac{\partial \mu_i}{\partial \rho_j}\right]_{T,\rho_{k\neq j}}. \tag{1.45}$$

The sum of the products $I_{ik}I^{kj}$ is 1 when $i = j$ and 0 when $i \neq j$:

$$\sum_{k=1}^{2} I_{ik}I^{kj} = \sum_{k=1}^{2}\left[\frac{\partial \rho_i}{\partial \mu_k}\right]_{T,\mu_{l\neq k}}\left[\frac{\partial \mu_k}{\partial \rho_j}\right]_{T,\rho_{m\neq j}} = \frac{\partial \rho_i}{\partial \rho_j} = \delta_{ij}. \tag{1.46}$$

From Eq. (1.46), we can obtain the expressions for I^{11}, I^{12}, I^{21}, I^{22} in terms of I_{ij}:

$$I^{11} = \frac{I_{22}}{\det\{I_{ij}\}}, \quad I^{12} = -\frac{I_{12}}{\det\{I_{ij}\}}, \quad I^{21} = -\frac{I_{21}}{\det\{I_{ij}\}}, \quad I^{22} = \frac{I_{11}}{\det\{I_{ij}\}}, \tag{1.47}$$

where $\det\{I_{ij}\}$ is the determinant of the matrix $\{I_{ij}\}$:

$$\det\{I_{ij}\} = I_{11}I_{22} - I_{12}I_{21}. \tag{1.48}$$

I^{ij} in Eq. (1.45) is defined at constant volume V. We change the independent variable from V to the pressure p. If the chemical potential μ_i of the molecular species i is a function of p, T, and $N_{j\neq i}$, the total derivative of μ_i is given by

$$d\mu_i = \left[\frac{\partial \mu_i}{\partial p}\right]_{T,N_{j\neq i}} dp + \left[\frac{\partial \mu_i}{\partial T}\right]_{p,N_{j\neq i}} dT + \left[\frac{\partial \mu_i}{\partial N_j}\right]_{p,T} dN_j. \tag{1.49}$$

Then, the derivative of μ_i with respect to N_j at constant V, T, and $N_{k\neq j}$ is

$$\left[\frac{\partial \mu_i}{\partial N_j}\right]_{V,T,N_{k\neq j}} = \left[\frac{\partial \mu_i}{\partial p}\right]_{T,N_1,N_2}\left[\frac{\partial p}{\partial N_j}\right]_{V,T,N_{k\neq j}} + \left[\frac{\partial \mu_i}{\partial N_j}\right]_{p,T,N_{k\neq j}}. \tag{1.50}$$

We also use two equations to change the independent variable. One is the following identity,

$$\left[\frac{\partial p}{\partial N_j}\right]_{V,T,N_{k\neq j}}\left[\frac{\partial N_j}{\partial V}\right]_{p,T,N_{k\neq j}}\left[\frac{\partial V}{\partial p}\right]_{T,N_1,N_2} = -1, \tag{1.51}$$

and the other is the Maxwell relation,

$$\left[\frac{\partial \mu_i}{\partial p}\right]_{T,N_1,N_2} = \left[\frac{\partial V}{\partial N_i}\right]_{p,T,N_{j\neq i}} \equiv v_i, \tag{1.52}$$

where v_i is the partial molecular volume of the molecular species i.

From Eqs. (1.45), (1.50), (1.51), and (1.52), we obtain

$$\mu_{ij} \equiv \left[\frac{\partial \mu_i}{\partial N_j}\right]_{p,T,N_{k\neq j}} = \frac{kT}{V} I^{ij} - \frac{v_i v_j}{V\chi}, \tag{1.53}$$

where χ is the isothermal compressibility of the two-component system, defined by

$$\chi \equiv -\frac{1}{V}\left[\frac{\partial V}{\partial p}\right]_{T,N_1,N_2}. \tag{1.54}$$

We now have three equations to obtain the relationship between the KB integral G_{ij} and the thermodynamic quantities v_i and χ. The first equation is Eq. (1.53). The second is derived from the Gibbs-Duhem equation at constant pressure and temperature:

$$\sum_{i=1}^{2} \rho_i d\mu_i = 0 \quad \rightarrow \quad \sum_{i=1}^{2} \rho_i \left[\frac{\partial \mu_i}{\partial N_j}\right]_{p,T,N_{k\neq j}} = \sum_{i=1}^{2} \rho_i \mu_{ij} = 0. \tag{1.55}$$

The third is the identity for the partial molecular volume v_i:

$$\sum_{i=1}^{2} \rho_i v_i = 1. \tag{1.56}$$

By solving the simultaneous equation consisting of Eqs. (1.53), (1.55), and (1.56), we can obtain the expressions of χ and v_i in terms of I^{ij}:

$$kT\chi = \left[\sum_{i=1}^{2}\sum_{j=1}^{2} \rho_i \rho_j I^{ij}\right]^{-1}. \tag{1.57}$$

$$v_i = \sum_{k=1}^{2} \rho_k I^{ki} \left[\sum_{i=1}^{2}\sum_{j=1}^{2} \rho_i \rho_j I^{ij}\right]^{-1}. \tag{1.58}$$

Eqs. (1.44) and (1.47) are used to rewrite Eqs. (1.57) and (1.58) using G_{ij}. The

denominator in Eq. (1.57) is

$$\begin{aligned}\sum_{i=1}^{2}\sum_{j=1}^{2}\rho_i\rho_j I^{ij} &= \rho_1^2 I^{11} + \rho_1\rho_2 I^{12} + \rho_2\rho_1 I^{21} + \rho_2^2 I^{22} = \frac{\rho_1^2 I_{22} + \rho_2^2 I_{11} - \rho_1\rho_2(I_{12}+I_{21})}{I_{11}I_{22} - I_{12}I_{21}} \\ &= \frac{\rho_1^2\rho_2^2 G_{22} + \rho_1^2\rho_2 + \rho_1^2\rho_2^2 G_{11} + \rho_1\rho_2^2 - \rho_1\rho_2(\rho_1\rho_2 G_{12} + \rho_1\rho_2 G_{21})}{\rho_1^2\rho_2^2 G_{11}G_{22} + \rho_1^2\rho_2 G_{11} + \rho_1\rho_2^2 G_{22} + \rho_1\rho_2 - \rho_1^2\rho_2^2 G_{12}G_{21}} \\ &= \frac{\rho_1 + \rho_2 + \rho_1\rho_2(G_{11} + G_{22} - 2G_{12})}{1 + \rho_1 G_{11} + \rho_2 G_{22} + \rho_1\rho_2(G_{11}G_{22} - G_{12}^2)}. \end{aligned} \tag{1.59}$$

Note that $G_{12} = G_{21}$ because of Eq. (1.37). In the limit of the infinite dilution of the solute, i.e., $\rho_2 \to 0$, Eq. (1.57) reduces to

$$kT\chi^0 = \frac{1}{\rho_1^0} + G_{11}^0, \tag{1.60}$$

where χ^0 is the isothermal compressibility of the pure solvent, ρ_1^0 is the number density of the pure solvent, and G_{11}^0 is the KB integral for the pure solvent.

The partial molecular volume v_2 of the solute is expressed as

$$\begin{aligned} v_2 &= kT\chi\left[\rho_1 I^{12} + \rho_2 I^{22}\right] = kT\chi\frac{\rho_2 I_{11} - \rho_1 I_{12}}{I_{11}I_{22} - I_{12}I_{21}} \\ &= kT\chi\frac{\rho_1^2\rho_2 G_{11} + \rho_1\rho_2 - \rho_1^2\rho_2 G_{12}}{\rho_1^2\rho_2^2 G_{11}G_{22} + \rho_1^2\rho_2 G_{11} + \rho_1\rho_2^2 G_{22} + \rho_1\rho_2 - \rho_1^2\rho_2^2 G_{12}G_{21}} \\ &= kT\chi\frac{1 + \rho_1(G_{11} - G_{12})}{1 + \rho_1 G_{11} + \rho_2 G_{22} + \rho_1\rho_2(G_{11}G_{22} - G_{12}^2)}. \end{aligned} \tag{1.61}$$

In the limit of $\rho_2 \to 0$,

$$v_2^0 = kT\chi^0\frac{1 + \rho_1^0 G_{11}^0 - \rho_1^0 G_{12}^0}{1 + \rho_1^0 G_{11}^0} = kT\chi^0 - G_{12}^0, \tag{1.62}$$

where v_2^0 and G_{12}^0 are the partial molecular volume of the solute and the KB integral between solvent and solute molecules, respectively, at infinite dilution.

At the end of this section, we derive the statistical mechanical expression for the osmotic second virial coefficient B. In thermodynamics, B is defined as the coefficient of

the density expansion of the osmotic pressure Π:

$$\Pi = kT(\rho_2 + B\rho_2^2 + C\rho_2^3 \cdots) \qquad \text{at constant } T \text{ and } \mu_1, \tag{1.63}$$

where ρ_2 is the number density of the solute, μ_1 is the chemical potential of the solvent, and C is called the osmotic third virial coefficient. Π is the difference between the two pressures $p(\rho_2)$ and $p(\rho_2 = 0)$: The former is the pressure of the solution at concentration ρ_2, and the latter is that of the pure solvent. The osmotic virial coefficients B, C, $\cdots$ quantify the deviation from van't Hoff's law ($\Pi = kT\rho_2$), which holds for dilute solutions.

We start from the Gibbs-Duhem equation at constant T:

$$dp = \rho_1 d\mu_1 + \rho_2 d\mu_2 \qquad \rightarrow \qquad \left[\frac{\partial p}{\partial \rho_2}\right]_{T,\mu_1} = \rho_2 \left[\frac{\partial \mu_2}{\partial \rho_2}\right]_{T,\mu_1}. \tag{1.64}$$

The left-hand side of Eq. (1.64) is rewritten as

$$\left[\frac{\partial p(\rho_2)}{\partial \rho_2}\right]_{T,\mu_1} = \left[\frac{\partial \big[p(\rho_2) - p(\rho_2 = 0)\big]}{\partial \rho_2}\right]_{T,\mu_1} = \left[\frac{\partial \Pi}{\partial \rho_2}\right]_{T,\mu_1} = kT(1 + 2B\rho_2 + \cdots). \tag{1.65}$$

The first equality is because the pressure of the pure solvent, $p(\rho_2 = 0)$, is independent of ρ_2. On the rightmost side of Eq. (1.65), the second and higher-order terms of ρ_2 are negligible when ρ_2 is small enough.

The right-hand side of Eq. (1.64) contains the inverse of the quantity I_{22} defined by Eq. (1.42):

$$\rho_2 \left[\frac{\partial \mu_2}{\partial \rho_2}\right]_{T,\mu_1} = \frac{kT\rho_2}{I_{22}}. \tag{1.66}$$

Eq. (1.44) indicates that I_{22} relates to the solute-solute KB integral G_{22}. In the limit of $\rho_2 \to 0$,

$$\lim_{\rho_2 \to 0} \left(\rho_2 \left[\frac{\partial \mu_2}{\partial \rho_2}\right]_{T,\mu_1} \right) = \lim_{\rho_2 \to 0} \Big(kT \big[1 + \rho_2 G_{22}\big]^{-1} \Big) = kT(1 - \rho_2 G_{22}^0), \tag{1.67}$$

where G_{22}^0 is the KB integral between solute molecules at infinite dilution.

From Eqs. (1.64), (1.65), and (1.67), we can obtain the expression of the osmotic B

in terms of the KB integral G_{22}^0:

$$B = -\frac{1}{2} G_{22}^0. \tag{1.68}$$

This equation is also obtained from the McMillan-Mayer theory.[9] Using the definitions of the KB integral and the potential $w(r)$ of mean force, Eq. (1.68) is rewritten as

$$B = -\frac{1}{2} \lim_{\rho_2 \to 0} \int \left[\exp\left[-\frac{w(r)}{kT} \right] - 1 \right] d\boldsymbol{r}. \tag{1.69}$$

Eq. (1.69) relates the solute-solute effective potential $w(r)$ to the osmotic B.

1.3 OUTLINE OF THESIS

The main focus of the present work is on the effect of solute size on the solute-solute effective interaction in water, aqueous solutions, and simple liquids. Extensive results obtained from molecular simulation and integral equation theory demonstrate that the nature of the effective interaction differs for small and large solutes.

In Chapter 2, we quantify the strength of the effective interaction in water and a nonpolar solvent. Based on molecular dynamics simulation, we calculate the potentials $w(r)$ of mean force and the osmotic second virial coefficients B for nonpolar solutes with different diameters σ. The simulation results suggest a power-law relationship between B and σ, partially in agreement with the theoretical prediction.[10]

Chapter 3 focuses on the size dependence of the solute-solute effective potentials $w(r)$ in water. $w(r)$ has several minima and maxima as a function of the inter-solute distance r, which correspond to the structural change of water near the solute pair depending on r. Molecular dynamics studies show that the thermodynamic and microscopic factors determining the magnitudes of the minima and maxima of $w(r)$ vary as the solute size σ increases up to C_{60} fullerene's size. We also investigate the effect of the solute-water attraction.

In Chapter 4, we verify the universality of the power-law relationship between the osmotic B and the solute diameter σ. Based on the integral equation theory, we solve

the Ornstein-Zernike equation with the MHNC closure[11] to calculate B for hard-sphere particles with different diameters σ from 1 to 50 times larger than the hard-sphere diameter of a solvent particle. We also use the Monte Carlo simulation, the Asakura-Oosawa theory,[12] and the Boubík-Mansoori-Carnahan-Starling-Leland equation of state[13], [14] to compare their numerical results.

Finally, Chapter 5 presents the study of the effective interaction between 1-propanol molecules in the aqueous solution. 1-Propanol and water are miscible at any concentration, but at the molecular level, 1-propanol molecules locally aggregate, especially at low alcohol concentrations. Molecular simulation results show that the aggregation of 1-propanol molecules is due to the effective interaction between the hydrophobic groups of these molecules, i.e., the hydrophobic interaction.

Chapter 2

Solute-Solute Effective Interactions Varying with Solute Size in Water and Simple Liquid

Abstract

We performed molecular simulations to investigate the solute size dependence of the strength of effective interactions between nonpolar solutes in water and a nonpolar solvent. The potentials $w(r)$ of mean force and the osmotic second virial coefficients B are evaluated for the solute particles of different diameters, from the size of methane to that of C_{60} fullerene. When the solute-solvent attraction is the same as the methane-water interaction, the first minimum of $w(r)$ and the osmotic B are negative and decrease as the solute diameter σ increases. The magnitude of B becomes larger with σ following the power law $B \propto \sigma^{\alpha}$ with $\alpha = 6$ or 7. We also examine the size dependence of $w(r)$ varying with the strength of the solute-solvent attraction. Simulation results show that there would be a threshold for the magnitude ϵ_{uv} of the solute-water attraction to change the character of $w(r)$: If ϵ_{uv} is set below or above the threshold, the solute-solute effective interaction becomes more attractive or more repulsive, respectively, as σ increases. The effect of the solute-solvent pair interaction on the σ dependence of $w(r)$ and B in a nonpolar solvent is similar to that in water.

Publications

- Hidefumi Naito, Ryuichi Okamoto, Tomonari Sumi, and Kenichiro Koga, "Osmotic second virial coefficients for hydrophobic interactions as a function of solute size", *The Journal of Chemical Physics*, 2022, **156**, 221104 (5 pages).

- Hidefumi Naito, Tomonari Sumi, and Kenichiro Koga, "How do water-mediated interactions and osmotic second virial coefficients vary with particle size?", *Faraday Discussions*, 2024, **249**, 440-452.

2.1 INTRODUCTION

The solute-solute effective interaction in a solution is qualitatively different from the direct pair interaction in a vacuum. An example is the hydrophobic interaction, which is the effective interaction between apolar molecules, or apolar moieties of amphiphilic molecules, in water or aqueous solutions. Hydrophobic interactions are the driving force for various aggregates of surfactants and play a role in the structural stability and the function of proteins in vivo. Recent reviews outline the topic for the study of hydrophobic interactions.[1], [15]–[18]

One way to quantify the strength of the inter-solute effective interaction is the measurement of the potential $w(r)$ of mean force for pairs of solutes in a solvent, which is a function of the solute-solute separation r. The effective potential $w(r)$ is related to the radial distribution function $g(r)$ as $w(r) = -kT \ln g(r)$, where k is Boltzmann's constant and T is the temperature. The depth of the first minimum of $w(r)$ quantifies the stability of a contact pair of solutes.

The osmotic second virial coefficient B also quantifies the strength of effective interactions between solutes. B and $w(r)$ are related by[9]

$$B = -\frac{1}{2}\lim_{\rho\to 0}\int\left[\exp\left[-\frac{w(r)}{kT}\right]-1\right]d\tau = -\frac{1}{2}\lim_{\rho\to 0}\int_0^\infty [g(r)-1]4\pi r^2 dr = -\frac{1}{2}G, \qquad (2.1)$$

where ρ is the number density of the solute, $d\tau$ is the infinitesimal volume element, and G is the Kirkwood-Buff integral[7] between solute molecules at infinite dilution. If B is negative, then the solute-solute effective pair interaction is attractive, and otherwise (except for $B = 0$), that interaction is repulsive.

Due to the extremely low solubility of hydrophobic solutes in water, $g(r)$ and B for them have been obtained from theoretical calculation and molecular simulation instead of experimental measurements. The osmotic B for several molecules has been calculated based on the molecular simulation[19]–[26] and the equation of state.[27]–[31] However, the data of B are still sparse to understand how the microscopic properties of solute molecules affect the strength of solute-solute effective interactions.

Here, we focus on the effective interaction between solute molecules varying with solute size and the effect of the solute-solvent attraction on that size dependence. The molecular size effects on the peak heights of $g(r)$ and $w(r)$ have been studied.[4]–[6], [32]–[34] For example, E. Sobolewski and coworkers calculated $w(r)$ for pairs of hydrocarbons with different carbon numbers in water based on the molecular simulation.[4], [5] They clarified that the water-mediated contribution to the contact minimum of $w(r)$ changes from negative (attractive) to positive (repulsive) with increasing the carbon number of the solutes. The solute-size effects on $w(r)$ in simple liquids have also been a crucial matter in the theory of liquids.[35]–[41] The solute size dependence of hydrophobic hydration, which is related to the stability of a nonpolar molecule in water, has also been extensively discussed.[3], [42]–[52] In contrast, there are few investigations for the size dependence of B.

This paper demonstrates the simulation results of the effective potential $w(r)$ and the osmotic B for Lennard-Jones (LJ) particles with different LJ diameters σ ranging from methane size to C_{60} fullerene size in water and a LJ solvent. We discuss the σ dependence of the first minimum of $w(r)$ and the osmotic B. The latter dependence is obtained as a quantitative power law relationship $B \propto \sigma^{\alpha}$. We also investigate the σ dependence of $w(r)$ varying with the strength of the solute-solvent attraction.

2.2 COMPUTATIONAL DETAILS

2.2.1 Molecular Dynamics Simulation of Aqueous Solutions

The simulation system consists of water molecules represented by the TIP4P (**T**ransferable **I**ntermolecular **P**otential **4** **P**oint)/2005 force field[53] and spherical solute particles. Two solute particles interact through the Lennard-Jones (LJ) potential:

$$\phi_{ij}^{\mathrm{LJ}}(r) = 4\epsilon_{ij}\left[\left(\frac{\sigma_{ij}}{r}\right)^{12} - \left(\frac{\sigma_{ij}}{r}\right)^{6}\right], \tag{2.2}$$

where σ_{ij} is the LJ diameter for pairs of species i and j, and ϵ_{ij} is the well depth of $\phi_{ij}^{\mathrm{LJ}}(r)$. The pair interaction between the solute particle and water molecules is represented by

the LJ potential $\phi_{\rm uv}^{\rm LJ}(r)$ or the repulsive Weeks-Anderson-Chandler (WCA) potential:[54]

$$\phi_{ij}^{\rm WCA}(r) = \begin{cases} \phi_{ij}^{\rm LJ}(r) + \epsilon_{ij} & (r < 2^{\frac{1}{6}}\sigma_{ij}) \\ 0 & (r \geq 2^{\frac{1}{6}}\sigma_{ij}). \end{cases} \tag{2.3}$$

The reference LJ parameters to examine the size effect are the TraPPE-UA (**Tra**nsferable **P**otentials for **P**hase **E**quilibria **-** **U**nited-**A**tom) force field[55] of methane, which are $\sigma_{\rm m} = 0.373$ nm and $\epsilon_{\rm m} = 1.23$ kJ mol^{-1}. The solute LJ diameters σ are set to $\sigma/\sigma_{\rm m} =$ 1, 1.2, 1.3, 1.5, 1.6, 2, 2.5, and 3. The energy parameter ϵ for a pair of LJ solutes is fixed to $\epsilon_{\rm m}$. For the pair interactions between the solute particle and water molecules, the size parameter $\sigma_{\rm uv}$ is set to $(\sigma + \sigma_{\rm w})/2$, where $\sigma_{\rm w} = 0.31589$ nm is the LJ diameter of the oxygen atom of the TIP4P/2005 water. The energy parameter $\epsilon_{\rm uv}$ for the reference solute is given by $\epsilon_0 = \sqrt{\epsilon_{\rm m}\epsilon_{\rm w}}$ using $\epsilon_{\rm w} = 0.775$ kJ mol^{-1} of the TIP4P/2005 model. We set $\epsilon_{\rm uv}/\epsilon_0 = 1$, 2, and 3 to investigate the effect of the solute-water attraction. We also consider the "repellent" solutes with diameters $\sigma/\sigma_{\rm m} = 1$, 2, and 3: They interact with the oxygen atom of water molecules through the repulsive WCA potential $\phi_{\rm uv}^{\rm WCA}(r)$ in Eq. (2.3) with $\epsilon_{\rm uv}/\epsilon_0 = 1$.

We performed isobaric-isothermal molecular dynamics (MD) simulations using GROMACS (**GRO**ningen **MA**chine for **C**hemical **S**imulations) 2018.[56] The three-dimensional periodic boundary condition was applied to the cubic or rectangular solid simulation box. The number $N_{\rm w}$ of water molecules and the number N of solute particles in the solutions depend on the values of σ and $\epsilon_{\rm uv}$ as shown in Table 2.1. The pressure is set to 1 bar by the Parrinello-Rahman method. The temperature is maintained at 300 K by the Nosé-Hoover method. The duration time t of the production run is $t = 100$ ns for the simulations of the model systems with $N \geq 20$. For the systems of the LJ particles with $\sigma/\sigma_{\rm m} = 1.5$ and 1.6, $t = 200$ ns. For those with $N = 2$, we performed the umbrella sampling simulation.[57], [58] t for each umbrella window is 20 ns except for the system of a pair of WCA solutes with $\sigma/\sigma_{\rm m} = 1$, in which case $t = 10$ ns. The time step interval of each simulation is 0.001 ps. We recorded the configurations of water and solute molecules every 0.05 ps to calculate the solute-solute radial distribution function $g(r)$.

Table 2.1: The number N_{w} of water molecules and the number N of solute particles depending on the solute LJ diameter σ and solute-water LJ energy parameter ϵ_{uv} in the model solutions. The "LJ" solutes interact with the oxygen atom of water molecules via the LJ potential $\phi_{\mathrm{uv}}^{\mathrm{LJ}}(r)$, and the "WCA" solutes interact with that via the repulsive WCA potential $\phi_{\mathrm{uv}}^{\mathrm{WCA}}(r)$.

Solute	$\sigma/\sigma_{\mathrm{m}}$	$\epsilon_{\mathrm{uv}}/\epsilon_0$	N_{w}	N
LJ	1, 1.2, 1.3	1	4000	40
LJ	1.5, 1.6	1	4000	20
LJ	2, 2.5, 3	1	8000	2
LJ	1	2, 3	4000	20
LJ	2	2, 3	8000	40
LJ	3	2, 3	16000	80
WCA	1	1	4000	2
WCA	2, 3	1	8000	2

In the umbrella sampling simulations, the harmonic potential was applied to constrain the distance between two solute particles. The spring constant of that potential is 1000 kJ mol^{-1} nm^{-2}. The constraint distance between the LJ solutes ranges from 0.6 to 2.9 nm for $\sigma/\sigma_{\mathrm{m}} = 2$, from 0.7 to 2.8 nm for $\sigma/\sigma_{\mathrm{m}} = 2.5$, and from 0.8 to 3.1 nm for $\sigma/\sigma_{\mathrm{m}} = 3$, in 0.1 nm increments. For the WCA solutes, the inter-solute distance is constrained, ranging from 0.2 to 2.5 nm for $\sigma/\sigma_{\mathrm{m}} = 1$, from 0.6 to 2.9 nm for $\sigma/\sigma_{\mathrm{m}} = 2$, and from 0.8 to 3.1 nm for $\sigma/\sigma_{\mathrm{m}} = 3$. The potential $w(r)$ of mean force was obtained from the umbrella sampling data using the weighted histogram analysis method.[59], [60]

The radial distribution functions $g(r)$ obtained from the MD simulations with $N \geq 20$ are in the model solutions with finite concentrations of the solute, but those in an infinitely dilute solutions are necessary to compute the osmotic second virial coefficients B. We employed the following method[19] to calculate $g(r)$ for hydrophobic solutes in water at infinite dilution. For the systems of LJ particles with $\sigma/\sigma_{\mathrm{m}} = 1$, 1.2, 1.3, 1.5, 1.6, and $\epsilon_{\mathrm{uv}}/\epsilon_0 = 1$, the solute-solute pair potential $\phi_{\mathrm{uu}}^{\mathrm{LJ}}(r)$ was replaced by some repulsive potential $\phi_{\mathrm{uu}}^{\mathrm{rep}}(r)$. We calculated the required $g(r)$ using the radial distribution function

$g^{\mathrm{rep}}(r)$ obtained from the simulation with $\phi_{\mathrm{uu}}^{\mathrm{rep}}(r)$ by

$$g(r) = g^{\mathrm{rep}}(r) \exp\left[-\frac{\phi_{\mathrm{uu}}^{\mathrm{att}}(r)}{kT}\right], \tag{2.4}$$

where $\phi_{\mathrm{uu}}^{\mathrm{att}}(r) = \phi_{\mathrm{uu}}^{\mathrm{LJ}}(r) - \phi_{\mathrm{uu}}^{\mathrm{rep}}(r)$.

Here, we derive Eq. (2.4). The effective potential $w(r)$ for the LJ particles is the sum of the direct part $\phi_{\mathrm{uu}}^{\mathrm{LJ}}(r)$ and the solvent-mediated part $w^*(r) = w(r) - \phi_{\mathrm{uu}}^{\mathrm{LJ}}(r)$. When the repulsive potential $\phi_{\mathrm{uu}}^{\mathrm{rep}}(r)$ is applied during the simulation, the direct part of the resulting effective potential $w^{\mathrm{rep}}(r)$ is different from that of $w(r)$, but the solvent-mediated part $w^*(r)$ should be identical. Therefore, $g(r)$ can be expressed as

$$\begin{aligned} g(r) &= \exp\left[-\frac{w(r)}{kT}\right] = \exp\left[-\frac{w^*(r) + \phi_{\mathrm{uu}}^{\mathrm{LJ}}(r)}{kT}\right] \\ &= \exp\left[-\frac{w^{\mathrm{rep}}(r) - \phi_{\mathrm{uu}}^{\mathrm{rep}}(r) + \phi_{\mathrm{uu}}^{\mathrm{LJ}}(r)}{kT}\right] \\ &= g^{\mathrm{rep}}(r) \exp\left[-\frac{\phi_{\mathrm{uu}}^{\mathrm{att}}(r)}{kT}\right] \end{aligned} \tag{2.5}$$

with $g^{\mathrm{rep}}(r) = \exp[-w^{\mathrm{rep}}(r)/kT]$.

We assume that $g^{\mathrm{rep}}(r)$ is close to that at infinite dilution because the solutes repelling each other do not tend to aggregate. For the LJ particles with $\sigma/\sigma_{\mathrm{m}} = 1$, 1.2, and 1.3, $\phi_{\mathrm{uu}}^{\mathrm{rep}}(r)$ is the repulsive WCA potential $\phi_{\mathrm{uu}}^{\mathrm{WCA}}(r)$ in Eq. (2.3), while for the solutes with $\sigma/\sigma_{\mathrm{m}} = 1.5$ and 1.6, $\phi_{\mathrm{uu}}^{\mathrm{rep}}(r) = 4\epsilon(\sigma/r)^{12}$.

All the LJ and WCA pair potentials were truncated at the cutoff distance r_{cut} varying with the solute size: $r_{\mathrm{cut}} = 1.3$ nm for the aqueous solutions of solute particles with $\sigma/\sigma_{\mathrm{m}} = 1$, 1.2, 1.3, 1.5, and 1.6, $r_{\mathrm{cut}} = 2$ nm for those with $\sigma/\sigma_{\mathrm{m}} = 2$ and 2.5, and $r_{\mathrm{cut}} = 2.4$ nm for those with $\sigma/\sigma_{\mathrm{m}} = 3$. The Coulomb potentials were treated using the particle mesh Ewald method. The cutoff distances of those potentials in the real space are equal to the r_{cut} of the LJ pair potentials.

2.2.2 Molecular Dynamics Simulation of Lennard-Jones Mixtures

We also studied the nonpolar solutions to compare the size effects on the effective potential $w(r)$ and the osmotic B in a simple liquid with those in water. A simple liquid mixture consists of solute and solvent particles interacting through the LJ potentials. All the quantities of this system are given in reduced units using the LJ parameters $\sigma_{\rm v}$ and $\epsilon_{\rm v}$ of the solvent particle. The solute LJ diameters are $\sigma^* \equiv \sigma/\sigma_{\rm v} = 1$, 2, and 3, with the solute-solute energy parameter $\epsilon^* \equiv \epsilon/\epsilon_{\rm v} = 1$. The LJ parameters between solute and solvent particles are set to $\sigma^*_{\rm uv} = (\sigma^* + 1)/2$ and $\epsilon^*_{\rm uv} \equiv \epsilon_{\rm uv}/\epsilon_{\rm v} = 0.5$, 1, 2. The temperature and the number density of the solvent for the model mixtures are $T^* \equiv kT/\epsilon_{\rm v} = 1.5$ and $\rho^*_{\rm v} \equiv \rho_{\rm v}\sigma^3_{\rm v} = 0.8$, respectively. $\rho^*_{\rm v} = 0.8$ is close to the density of the LJ fluid at the triple point, and $T^* = 1.5$ is higher than the critical point.[61] At this state point, Kimura and Yoshimura obtained the solute-solute radial distribution functions $g(r)$ for $\sigma^* = 0.5$, 1, 1.5, $\epsilon^* = 1$, and $\epsilon^*_{\rm uv} = 1$, 2 based on the integral equation theory.[62]

MD simulations of the LJ mixtures at constant volume and temperature were performed using GROMACS 2018.[56] The numbers of solvent and solute particles are given in Table 2.2. The duration time $t^* \equiv t\sqrt{\epsilon_{\rm v}/(m\sigma^2_{\rm v})}$ of the production run and the cutoff distance $r^*_{\rm cut} \equiv r_{\rm cut}/\sigma_{\rm v}$ of the LJ potentials vary with solute size, where m is the weight of a solvent particle. For the systems of LJ solutes with $\sigma^* = 1$, $t^* = 84659$ and $r^*_{\rm cut} = 3.077$, and for $\sigma^* = 2$ and 3, $t^* = 169318$ and $r^*_{\rm cut} = 6.154$. For the solutes with $\sigma^* = 3$, the LJ potential $\phi^{\rm LJ}_{\rm uu}(r)$ was replaced by the repulsive WCA potential $\phi^{\rm WCA}_{\rm uu}(r)$ in Eq. (2.3), and

Table 2.2: The number $N_{\rm v}$ of solvent particles with the LJ parameters $\sigma_{\rm v}$ and $\epsilon_{\rm v}$ and the N of solute particles with different LJ parameters $\sigma^* = \sigma/\sigma_{\rm v}$ and $\epsilon^*_{\rm uv} = \epsilon_{\rm uv}/\epsilon_{\rm v}$ in the LJ mixtures.

Solute	σ^*	$\epsilon^*_{\rm uv}$	$N_{\rm v}$	N
LJ	1	0.5, 1, 2	5000	20
LJ	2	0.5, 1, 2	10000	20
LJ	3	0.5, 1, 2	20000	40

we converted the resulting radial distribution function $g^{\mathrm{rep}}(r)$ to $g(r)$ based on Eq. (2.4).

2.2.3 Osmotic Second Virial Coefficient

Eq. (2.1) implies that the osmotic second virial coefficient B can be obtained from the volume integral of the difference between the radial distribution function $g(r)$ and unity. If we calculate B based on Eq. (2.1) using the numerical integration with respect to r, however, the solute-solute Kirkwood-Buff (KB) integral G might diverge. There are at least three reasons for this behavior:

1. $g(r)$ does not converge to 1 in a closed system.
2. Statistical errors in $g(r)$ at large distances r become enlarged by the factor of r^2.
3. The finite-size effect are there in any simulation.

We employed the following method to overcome these problems. The long-range behavior of $g(r)$ was corrected so that the average of $g(r)$ over a given range at large distances becomes 1.[19] Then, we used a sophisticated method proposed by Krüger et al.[63], [64] to evaluate G at the thermodynamic limit from the KB integral $G(L)$ for a finite volume:

$$G(L) = \int_0^L [g(r) - 1] 4\pi r^2 \left[1 - \frac{3}{2}\left(\frac{r}{L}\right) + \frac{1}{2}\left(\frac{r}{L}\right)^3 \right] dr, \tag{2.6}$$

$$G(L)L = GL + D, \tag{2.7}$$

where L is the upper limit of the integral in Eq. (2.6) and D is a constant. From Eq. (2.6) coupled with the corrected $g(r)$, we obtain $G(L)$ as a function of L. Then $G(L)L$ is plotted against L, and we find a certain range of L where the linear relationship of Eq. (2.7) holds. The linear fit in this L range gives the required KB integral G to obtain the osmotic B.

2.3 RESULTS AND DISCUSSION

The first investigation is the solute-size effect on the strength of the effective interaction between nonpolar solutes in water. Figure 2.1(a) shows the radial distribution functions

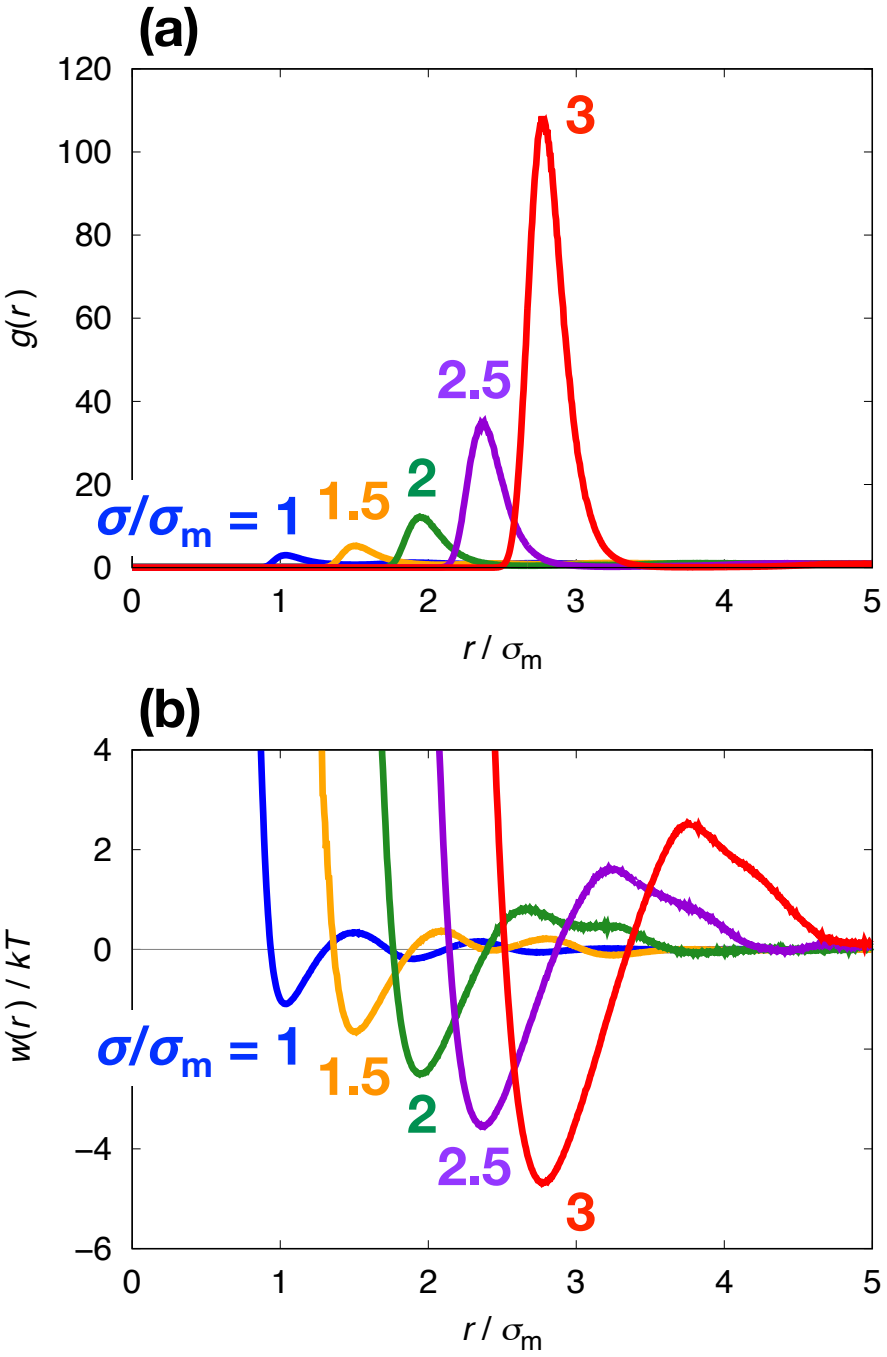

Figure 2.1: (a) The solute-solute radial distribution functions $g(r)$ for Lennard-Jones (LJ) particles of different sizes in water at 1 bar and 300 K. The solute LJ diameters are $\sigma/\sigma_{\mathrm{m}} = 1$, 1.5, 2, 2.5, and 3, where $\sigma_{\mathrm{m}} = 0.373$ nm is the LJ diameter of the TraPPE-UA model for methane.[55] (b) The corresponding solute-solute effective potentials $w(r) = -kT \ln g(r)$. Reproduced from Ref. [65] with permission from the Royal Society of Chemistry.

$g(r)$ for pairs of Lennard-Jones (LJ) particles with different LJ diameters σ in water. The solute size ranges from methane size ($\sigma/\sigma_{\rm m} = 1$) to C_{60} fullerene size ($\sigma/\sigma_{\rm m} = 3$). For all solutes, the depth ϵ of the solute-solute pair potential is set to $\epsilon_{\rm m} = 1.23$ kJ mol^{-1}, and that of the solute-water one $\epsilon_{\rm uv}$ is fixed at $\epsilon_0 = 0.977$ kJ mol^{-1}. It is clear that the first peak height of $g(r)$ increases with increasing σ: Its magnitude is 2.99, 5.25, 12.24, 35.01, and 108.01 for the LJ particles with $\sigma/\sigma_{\rm m} = 1$, 1.5, 2, 2.5, and 3, respectively.

The corresponding effective potentials $w(r)$ varying with solute size are shown in Figure 2.1(b). The first minimum of $w(r)$ monotonically decreases as the solute size increases: $w(r)/kT$ = -1.10, -1.66, -2.50, -3.56, and -4.69 at $\sigma/\sigma_{\rm m} = 1$, 1.5, 2, 2.5, and 3, respectively.

The decrease of the minimum is due to the water-mediated contribution $w^*(r) = w(r) - \phi_{\rm uu}^{\rm LJ}(r)$ to the effective potential because the direct pair potentials $\phi_{\rm uu}^{\rm LJ}(r)$ have the same well depth $\epsilon = \epsilon_{\rm m}$ for all-size solutes. The observed solvent-mediated attractions would be due to the excluded volume effect:[12] Each solute has an excluded volume from which the centers of solvent molecules are excluded (green circle in Figure 2.2(a)). When two solutes are close to each other, the two excluded volumes overlap (dark green in Figure 2.2(b)). The larger the overlapping volume with decreasing the solute-solute separation, the greater the configurational entropy of the solvent molecules. Therefore, the solvation free energy of the pair of solutes is lower with decreasing the distance.[66], [67]

When we apply the Asakura-Oosawa (AO) theory to a hard-sphere mixture consisting of solvent particles and a pair of solutes, the effective potential $w^{\rm AO}(r)$ at the contact distance $r = \sigma$ (σ is the hard-sphere diameter of the solute particle) is:[12]

$$\frac{w^{\rm AO}(\sigma)}{\eta kT} = -\frac{3}{2}\left(\frac{\sigma}{\sigma_{\rm v}}\right) - 1, \tag{2.8}$$

where $\sigma_{\rm v}$ is the hard-sphere diameter of the solvent particle and η is the packing fraction of the solvent. The AO potential $w^{\rm AO}(\sigma)$ shows similar size dependence to the contact minimum of the effective potential $w(r)$ in water (Figure 2.1(b)): They decrease with increasing solute size. However, the σ dependence of the first minimum of $w(r)$ in water is stronger than linear dependence, so the magnitude of the solvent-mediated contribution

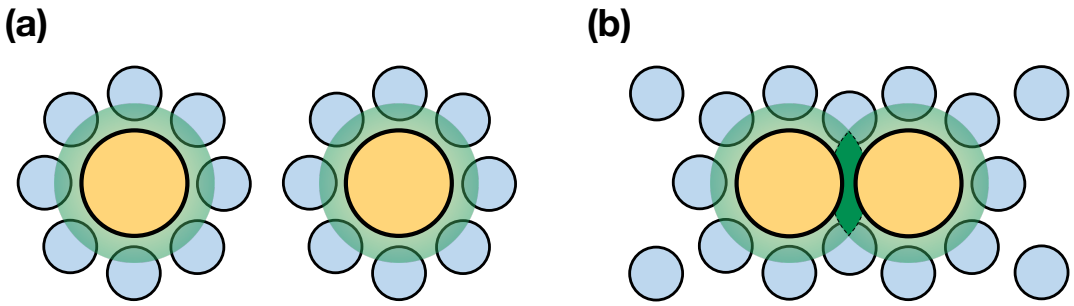

Figure 2.2: A simple illustration of the excluded volume effect.[12] Two yellow circles represent a pair of solute particles, and blue circles represent solvent molecules. Green circles are the excluded volume spheres of the solute particles, from which the centers of solvent molecules are excluded. Two solutes are (a) far apart and (b) close together. In the latter case, the two excluded volumes overlap (shown in dark green).

to the effective interaction is much stronger than the AO potential.

Figure 2.1(b) also shows that the first maximum of $w(r)$ is positive and ascends with increasing σ. In addition, the second minimum increases as the solute size increases, and it disappears at $\sigma/\sigma_{\rm m} = 2$. These trends would be characteristic of the hydrophobic interaction. We analyze the thermodynamic and microscopic factors determining the σ dependence of the first minimum, the first maximum, and the second minimum of $w(r)$ in Chapter 3.

Now, we study the σ dependence of the osmotic second virial coefficients B in water. Figure 2.3(a) is the plot of B vs. σ in a log-log scale. The osmotic B is negative for all-sized solutes, indicating that the inter-solute effective interactions are attractive regardless of solute size. The magnitude of B increases with increasing σ. Figure 2.3(a) suggests that B and σ have a linear relationship on a log-log scale, i.e., they exhibit the power law behavior

$$B \propto \sigma^{\alpha} \qquad (1 \leq \sigma/\sigma_{\rm m} \leq 3). \tag{2.9}$$

The dashed and solid blue lines are straight lines with slopes of 6 and 7, respectively. These results indicate that the best estimate of the exponent α in Eq. (2.9) is 7.

The second virial coefficient $B_{\rm gas}$ for the LJ gas, the measurement of the strength of the intermolecular interaction in a vacuum, is strictly proportional to σ^3 with ϵ fixed, as

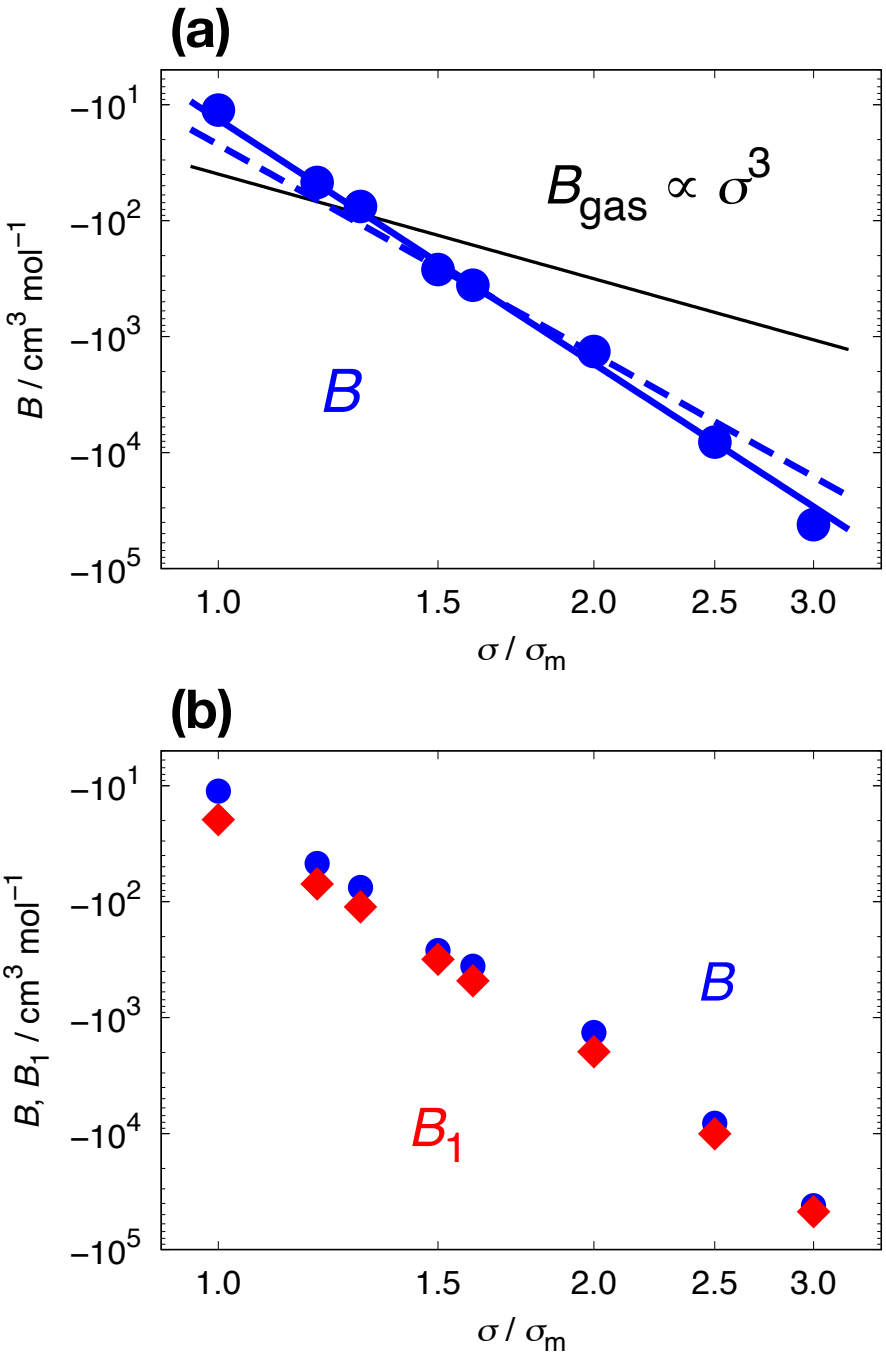

Figure 2.3: (a) The plot of the osmotic second virial coefficients B as a function of σ in a log-log scale. The dashed line represents the best fit of the 6th power law, and the solid blue line is that of the 7th power law. The gas virial coefficient $B_{\rm gas}$ for the LJ fluid is also plotted. It is known that $B_{\rm gas}$ is proportional to the cubic of σ. (b) The log-log plots of B vs. σ and $B_1 = -2\pi \int_0^{r_1} \left[\exp\left[-w(r)/kT\right] - 1\right] r^2 dr$ vs. σ, where r_1 is the inter-solute distance r of the first maximum of $w(r)$. Reproduced from Ref. [65] with permission from the Royal Society of Chemistry.

shown in Figure 2.3(a). Therefore, the characteristic behavior $B \propto \sigma^{\alpha}$ with the large exponent $\alpha \geq 6$ is due to the water-mediated interaction.

The inter-solute effective potential $w(r)$ exhibits oscillation depending on r, in contrast to the pair potential $\phi_{\mathrm{uu}}^{\mathrm{LJ}}(r)$ or $\exp\left[-\phi_{\mathrm{uu}}^{\mathrm{LJ}}(r)/kT\right]-1$, the latter function decays monotonically. Now, we examine which range of r determines the size dependence of B. We define B_1 as the contribution from $w(r)$ to B in the short-range $r \leq r_1$, where r_1 is r of the first maximum of $w(r)$:

$$B_1 = -\frac{1}{2}\int_{r\leq r_1}\left[\exp\left[-\frac{w(r)}{kT}\right]-1\right]d\tau. \tag{2.10}$$

Figure 2.3(b) compares B and B_1 for the solutes of different sizes. One can see that the σ dependence of the osmotic B is dominantly determined by that of B_1, i.e., the effective interaction in the short range.

It is remarkable that the thermodynamic identity for B predicts the 6th power law between B and σ:[10], [27]

$$B = B'' - \frac{(v-kT\chi)^2}{2kT\chi}. \tag{2.11}$$

In thermodynamics, the osmotic B is defined as the second-order coefficient in the expansion of the osmotic pressure Π with respect to the number density ρ of the solute at fixed temperature T and fixed chemical potential μ_{v} of the solvent. The first term B'' in Eq. (2.11) is an analog of B but the coefficient of ρ^2 in the ρ expansion of Π at fixed density ρ_{v} of the solvent instead of μ_{v}. In the second term, v is the partial molecular volume of the solute at infinite dilution, and χ is the isothermal compressibility of the pure solvent.

The second term $-(v-kT\chi)^2/2kT\chi$ in Eq. (2.11) has the σ^6 dependence because v should be proportional to the solute volume. Therefore, Eq. (2.11) predicts the 6th power law between B and σ, and the other σ dependence of B, such as $B \propto \sigma^7$, would be due to the σ dependence of B''.

The partial molecular volume v of the solute and the isothermal compressibility χ are

obtained based on the Kirkwood-Buff (KB) theory:[7]

$$v = -\int [g_{\mathrm{uv}}(r) - 1] d\tau + kT\chi, \tag{2.12}$$

where $g_{\mathrm{uv}}(r)$ is the radial distribution function for pairs of solute and solvent molecules, and

$$kT\chi = \int [g_{\mathrm{vv}}(r) - 1] d\tau + \frac{1}{\rho_{\mathrm{v}}}, \tag{2.13}$$

where $g_{\mathrm{vv}}(r)$ is the solvent-solvent radial distribution function.

To obtain $g_{\mathrm{uv}}(r)$ for pairs of the LJ solute and water molecules, we performed additional isobaric-isothermal MD simulations. The model system consists of 4000 water molecules and 1 LJ particle with different diameters σ. The pressure and temperature are set to 1 bar and 300 K, respectively. The duration time of the production run is 100 ns, and the partial molecular volumes v are calculated based on Eq. (2.12) by numerical integration with respect to r. The isobaric-isothermal MD simulation of 4000 water molecules was also performed to calculate $g_{\mathrm{vv}}(r)$ and thus χ of pure water at 1 bar and 300 K. The value of B'' in Eq. (2.11) was obtained as the difference between B and $-(v - kT\chi)^2/2kT\chi$.

Figure 2.4(a) shows the σ dependence of B and those of the two terms on the right-hand side of Eq. (2.11). The first term B'' is positive and increases with increasing solute diameter σ, while the second term $-(v - kT\chi)^2/2kT\chi$ is negative and decreases with σ. It is clear that the magnitudes of B'' and $-(v - kT\chi)^2/2kT\chi$ are much larger than the magnitude of B. Therefore, the sign and magnitude of B are determined by a slight difference between B'' and $(v - kT\chi)^2/2kT\chi$. This result is qualitatively the same as the numerical result obtained from the equation of state.[28] In our case, the magnitudes of the second term are slightly larger than those of B'' for all-size solutes.

Figures 2.4(b) and (c) are the log-log plots of B'' and $-(v - kT\chi)^2/2kT\chi$ against σ, respectively. We also show the best fits of the 6th power law to both data by dotted lines. $-(v - kT\chi)^2/2kT\chi$ has the 6th power dependence of σ since v is proportional to the cubic of σ. The first term B'' in Eq. (2.11) also has the same size dependence. Although

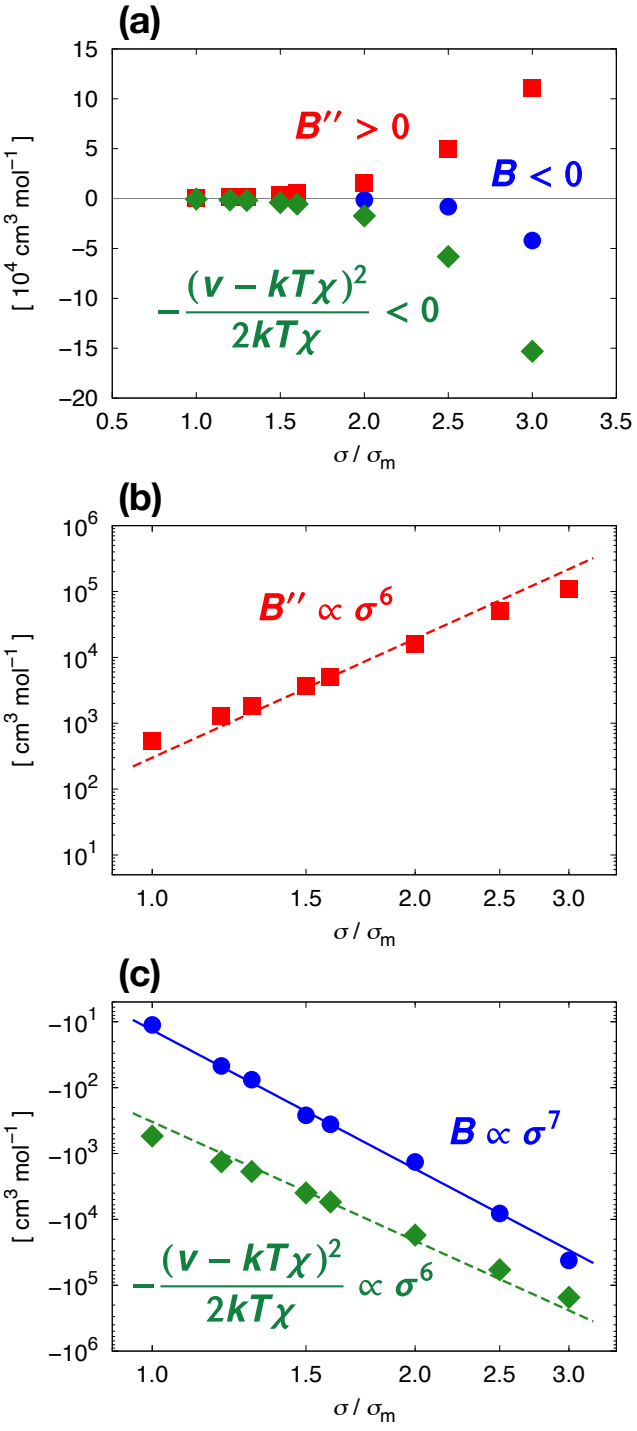

Figure 2.4: (a) B, B'', and $-(v - kT\chi)^2/2kT\chi$ for LJ particles in water as a function of σ. The solute LJ diameters are $\sigma/\sigma_{\rm m} = 1$, 1.2, 1.3, 1.5, 1.6, 2, 2.5, and 3. (b) The log-log plot of B'' against σ. The best fit to the data as $B'' \propto \sigma^{\alpha}$ with $\alpha = 6$ is also plotted by the dotted red line. (c) The plots of B vs. σ and $-(v - kT\chi)^2/2kT\chi$ vs. σ. The best fits of $B \propto \sigma^{\alpha}$ with $\alpha = 7$ and $-(v - kT\chi)^2/2kT\chi \propto \sigma^{\alpha}$ with $\alpha = 6$ are also plotted by the solid blue line and the dotted green line, respectively.

both B'' and $-(v-kT\chi)^2/2kT\chi$ have the σ^6 dependence, the osmotic B shows the power law behavior $B \propto \sigma^\alpha$ with $\alpha = 7$, as shown in Figures 2.3(a) and 2.4(c). We cannot explain why the σ dependence of B is different from that of the first and second terms in Eq. (2.11). In Chapter 4, we will present a detailed analysis of the size dependence of B, B'', and $-(v-kT\chi)^2/2kT\chi$ based on the integral equation theory.

Next, we investigate the solute-solvent attraction that might affect the solute size dependence of the effective pair interaction. Three types of solutes are considered: The solute particles with the solute-water energy parameters $\epsilon_{\rm uv}/\epsilon_0 = 1$, 2, and 3. In addition, we take into account the repellent solutes interacting with water molecule via the repulsive Weeks-Chandler-Andersen (WCA) potential[54] $\phi_{\rm uv}^{\rm WCA}(r)$ in Eq. (2.3) with $\epsilon_{\rm uv}/\epsilon_0 = 1$.

Figures 2.5(a), (b), and (c) show $w(r)$ for the solutes with $\sigma/\sigma_{\rm m} = 1$, 2, and 3, respectively. For all-size solutes, the first minimum and maximum of the effective potential $w(r)$ shift upward with increasing $\epsilon_{\rm uv}$ from ϵ_0 to $3\epsilon_0$. In contrast, when the solute particle is repellent with surrounding water molecules, $w(r)$ in the short r range is well below compared to $w(r)$ for the reference LJ solute with $\epsilon_{\rm uv}/\epsilon_0 = 1$. These results are consistent with the observation that the solvent-mediated interaction is weakened due to the enhancement of the solute-solvent attraction.[4], [5], [16]–[18], [24], [68]–[73] Earlier studies showed that, in some cases, the effective interactions between nonpolar molecules become attractive or repulsive depending on the environments.[73]–[75]

It is clear that the effect of the solute-water attraction on the size dependence of $w(r)$ is greater for larger solutes. Now, we investigate the σ dependence of the contact minimum $w(r_c)$, where r_c is the inter-solute distance r of the first minimum of $w(r)$. Figure 2.6 shows $w(r_c)$ as a function of σ. The set of the LJ solutes with $\epsilon_{\rm uv}/\epsilon_0 = 1$ is the reference to examine the size dependence. When the solute particle is repellent with water molecules, $w(r_c)$ is more negative than that for the reference set. The σ dependence of $w(r_c)$ for the WCA solutes is much greater than that for the reference LJ solutes.

When $\epsilon_{\rm uv}$ is three times larger than the reference value, however, $w(r_c)$ is positive and ascends as σ increases. The effective pair interaction could thus become more attractive or repulsive with increasing solute size depending on the magnitude of the solute-water

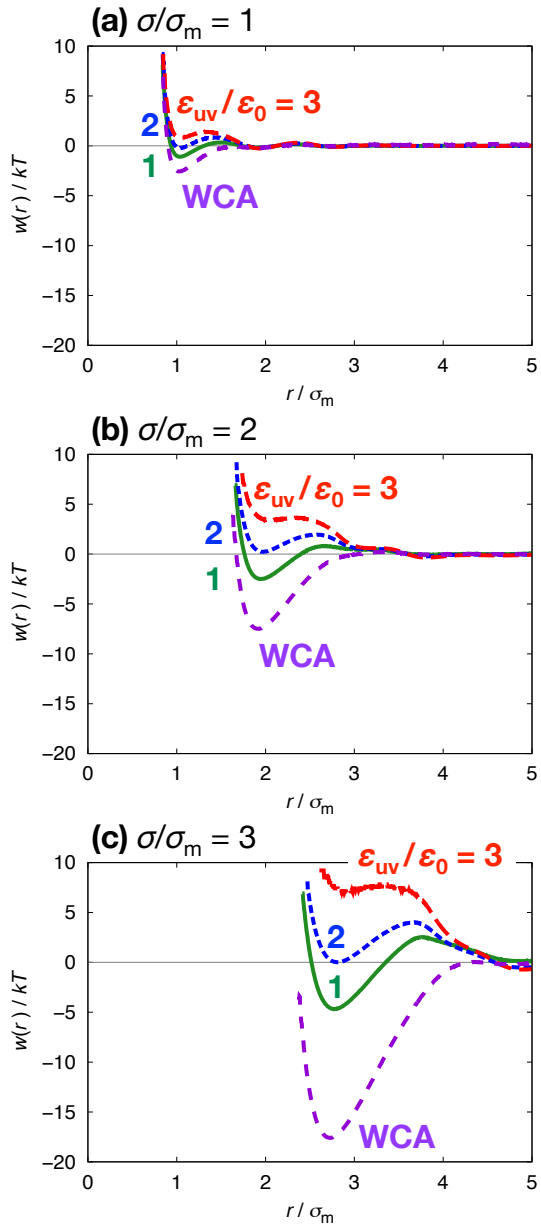

Figure 2.5: The effects of the strength of the solute-water attraction on the inter-solute effective potential $w(r)$ in water. The solute LJ diameters are set to (a) $\sigma/\sigma_{\rm m} = 1$, (b) $\sigma/\sigma_{\rm m} = 2$, and (c) $\sigma/\sigma_{\rm m} = 3$. The LJ energy parameters $\epsilon_{\rm uv}$ between the solute particle and the oxygen atom of water molecules varies from ϵ_0 to $3\epsilon_0$, where $\epsilon_0 = 0.977$ kJ mol^{-1} is the well depth of the methane-water pair potential. The solid green, dotted blue, and long-dashed red curves are $w(r)$ for the LJ solutes with $\epsilon_{\rm uv}/\epsilon_0 = 1$, 2, and 3, respectively. The dashed violet curves labeled "WCA" are the results of the solute particles interacting with the oxygen atom of water molecules through the repulsive Weeks-Chandler-Andersen (WCA) potential[54] with $\epsilon_{\rm uv}/\epsilon_0 = 1$. Reproduced from Ref. [65] with permission from the Royal Society of Chemistry.

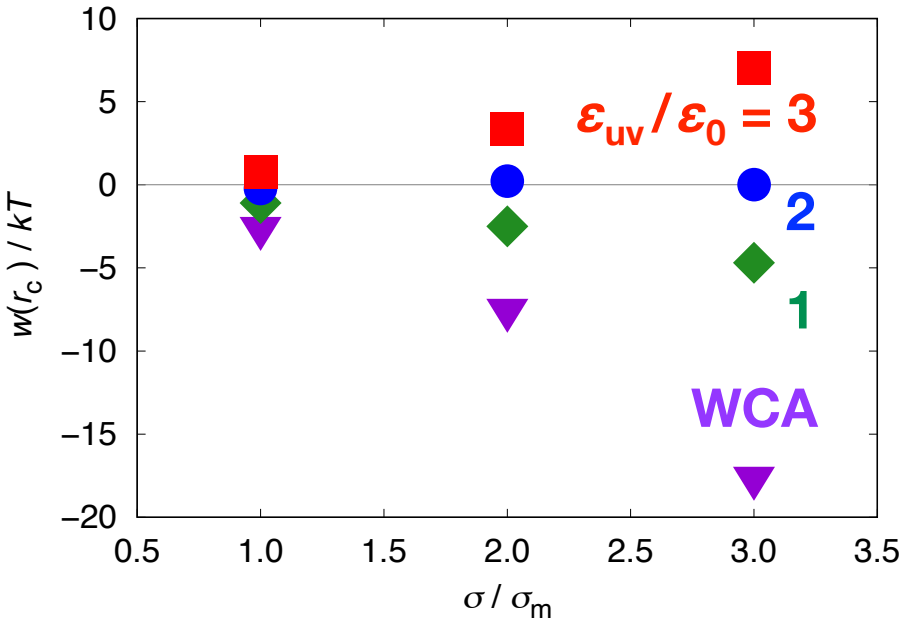

Figure 2.6: The first minimum $w(r_c)$ of the effective potential $w(r)$ for pairs of solutes with four different solute-water pair interactions as a function of σ. Green diamonds, blue circles, and red squares are the results for the LJ particles with $\epsilon_{\rm uv}/\epsilon_0 = 1$, 2, and 3, respectively. Violet triangles labeled "WCA" are the results for the WCA solutes with $\epsilon_{\rm uv}/\epsilon_0 = 1$. Reproduced from Ref. [65] with permission from the Royal Society of Chemistry.

attraction. There would be a threshold for $\epsilon_{\rm uv}$ that changes the σ dependence of $w(r_c)$ more positively or negatively. For our case of the aqueous solutions, the threshold seems to be around $2\epsilon_0$.

Finally, we examine the solute-size effect on the effective interaction in a LJ solvent and compare them with the result of the aqueous solutions. Figures 2.7(a), (b), and (c) show $g(r)$, $w(r)$, and B, respectively, for the LJ solutes with the solute-solvent LJ energy parameters $\epsilon^*_{\rm uv} = 0.5$, 1, and 2. For the solutes with $\epsilon^*_{\rm uv} = 0.5$, the first peak height of $g(r)$ increases as σ^* increases from 1 to 3, and the first minimum of $w(r)$ and the osmotic B decrease with σ^*. These results are qualitatively the same as those for the LJ solutes with $\epsilon_{\rm uv}/\epsilon_0 = 1$ in water. Note that the first maximum of $w(r)$ for $\epsilon^*_{\rm uv} = 0.5$ in the LJ solvent does not ascend with increasing σ^*, and the second minimum does not disappear. These changes against solute size are a notable difference from $w(r)$ in water.

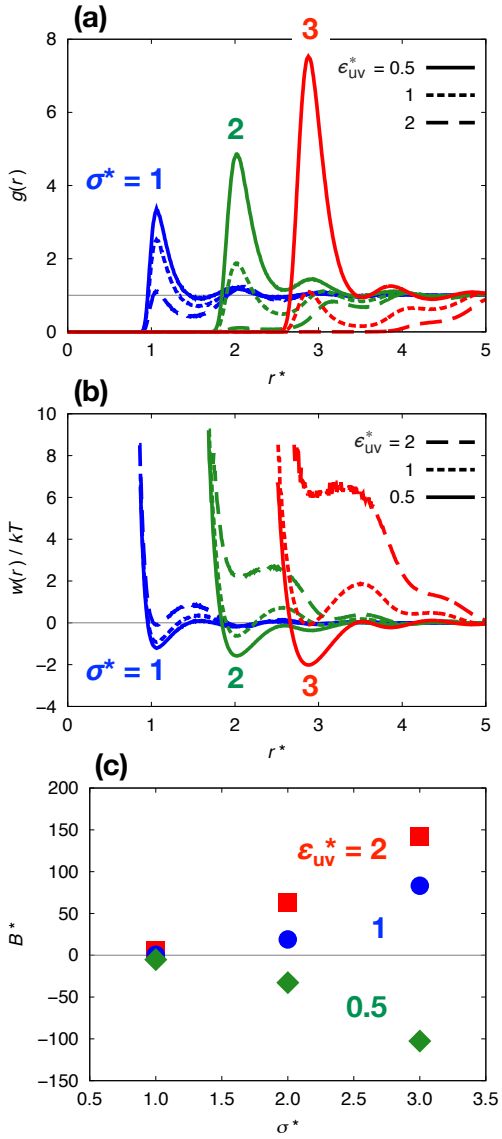

Figure 2.7: The effects of the solute size and the solute-solvent attraction on the effective interactions between the LJ solutes in the LJ solvent. The reduced density and temperature of the solvent are $\rho_{\rm v}^* = 0.8$ and $T^* = 1.5$, respectively. (a) The radial distribution functions $g(r)$ for the LJ particles with $\sigma^* = 1$, 2, 3, $\epsilon^* = 1$, and $\epsilon_{\rm uv}^* = 0.5$, 1, 2. The horizontal axis is $r^* \equiv r/\sigma_{\rm v}$, the solute-solute distance in the reduced unit. Blue, green, and red lines are the results for $\sigma^* = 1$, 2, and 3, respectively. The solid, dotted, and dashed curves are the results for $\epsilon_{\rm uv}^* = 0.5$, 1, and 2, respectively. (b) The corresponding inter-solute effective potentials $w(r)/kT$. (c) The osmotic second virial coefficients $B^* \equiv B/\sigma_{\rm v}^3$ in the reduced unit as a function of σ^*. Green diamonds, blue circles, and red squares represent B^* for $\epsilon_{\rm uv}^* = 0.5$, 1, and 2, respectively. Reproduced from Ref. [65] with permission from the Royal Society of Chemistry.

The σ dependence of $g(r)$, $w(r)$, and B for $\epsilon^*_{uv} = 1$ and 2 is completely different from those for $\epsilon^*_{uv} = 0.5$: The peak height of $g(r)$ decreases, and the contact minimum of $w(r)$ and the osmotic B increase with increasing σ^* from 1 to 3, indicating that the effective interaction becomes more repulsive as the solute size increases. The effect of increasing ϵ^*_{uv} on the σ dependence of the contact minimum is similar to that of the enhancement of the solute-water attraction on $w(r)$. The threshold for ϵ^*_{uv} in our LJ mixture would be between 0.5 and 1.

2.4 CONCLUSIONS

We investigated the effective pair potential for pairs of nonpolar solutes in water and a nonpolar solvent to understand how the solute size and the solute-solvent attraction affect the strength of the solute-solute effective interaction. We performed the molecular dynamics simulations and the umbrella sampling simulations[57], [58] of the model solutions. Based on these simulations, we compute the radial distribution functions $g(r)$ and the potentials $w(r)$ of mean force for the solutes of different sizes ranging from methane size to C_{60} fullerene size as accurately as possible. We also evaluated the osmotic second virial coefficients B using a sophisticated method to correct for the finite-size effect on the Kirkwood-Buff integral.[63], [64]

First, we considered the aqueous solutions of the Lennard-Jones (LJ) particles with different LJ diameters σ. When the solute-water direct pair potential is weak, the effective pair interaction at short distances becomes more attractive with increasing σ. The potential barrier between the first and second minima of $w(r)$ becomes also greater as the particle size increases. The osmotic B is negative, and its magnitude increases with increasing σ. The log-log plot of B vs. σ suggests the power law behavior $B \propto \sigma^\alpha$ with $\alpha = 6$ or 7.

The magnitude ϵ_{uv} of the pair interaction between solute and water molecules has a pronounced effect on the σ dependence of the effective potential $w(r)$. When the pair potential between the solute particle and the oxygen atom of water molecules is the repulsive Weeks-Chandler-Andersen (WCA) potential,[54] the σ dependence of the

contact minimum of $w(r)$ is greater than that for the reference LJ solutes: The minimum decreases more rapidly with increasing σ. In contrast, when the solute-water attraction is three times stronger than the reference solute with $\epsilon_{\rm uv} = \epsilon_0$, the effective interaction becomes increasingly repulsive with σ. There is a threshold for $\epsilon_{\rm uv}$, below which the first minimum of $w(r)$ decreases with increasing σ, and above which this minimum increases with σ. The threshold in the model aqueous solution is close to $\epsilon_{\rm uv}/\epsilon_0 = 2$.

The effect of the solute-solvent attraction on the solute size dependence of $w(r)$ in the LJ solvent is similar to that in water. For the solutes with $\epsilon^*_{\rm uv}$ =1 and 2, the effective pair interaction becomes more repulsive as σ^* increases, consistent with the numerical results obtained from the integral equation theory for the LJ mixtures at the same state point.[62] However, for a set of solutes with $\epsilon^*_{\rm uv} = 0.5$, the solute-solute effective interaction becomes more attractive with increasing σ^*. The threshold for $\epsilon^*_{\rm uv}$ in the LJ mixtures would be between 0.5 and 1.

The driving force of the enhancement of the attractive pair interaction with increasing solute size would be the increment of the configurational entropy of the solvent molecules due to the overlap of two excluded volumes of the solutes. The AO theory,[12] the simplest approximation for the excluded-volume effect, qualitatively reproduces the decrease of the contact minimum $w(\sigma)$ as σ increases. The opposite trend, that the solvent-mediated contribution to $w(r)$ becomes more repulsive with increasing solute size, is due to the attractive potential between solute and solvent molecules. The sum of the solute-solvent pair interaction energy is more negative when two solute particles are far apart than when they are in contact (Figure 2.8). We guess that at the threshold for $\epsilon_{\rm uv}$, the two opposing driving forces would be in balance.

Two open questions remain: First, why do the first maximum and the second minimum of the effective pair potentials $w(r)$ for LJ particles in water increase with increasing solute LJ diameter σ? Second, why the exponent α of the power law $B \propto \sigma^\alpha$ is 7, not 6, as predicted from the thermodynamic identity? In Chapter 3, we will show the simulation results to answer the first question. We study the microscopic structure of water around a pair of solutes when their separation is r of the first minimum, first maximum, and second

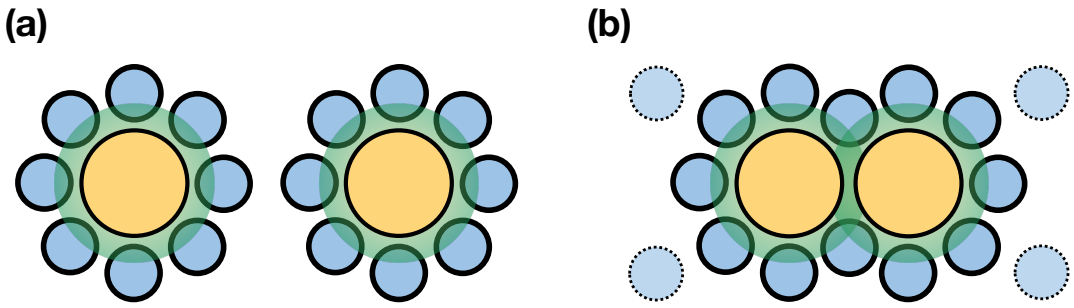

Figure 2.8: Schematic representation of two solutes being (a) far apart and (b) in contact with each other in a solvent. Two yellow circles represent a pair of solute particles, and blue circles represent solvent molecules. Green circles are the excluded volume sphere of the solute particle. As the two solutes approach each other, the number of solvent molecules surrounding the solute pair (highlighted by the circles with thick circumferences) decreases due to the overlap of the two excluded volume spheres. Therefore, the sum of the solute-solvent attractive interaction energy is more negative when two particles are far apart.

minimum of $w(r)$. Thermodynamic and microscopic factors determining the σ dependence of these extreme values are clarified. In addition, we apply the integral equation theory to the hard-sphere mixtures and obtain the σ dependence of each term in the thermodynamic identity Eq. (2.11) for the osmotic B. Chapter 4 demonstrates these numerical results.

Chapter 3

Thermodynamic and Microscopic Factors Determining the Solute-Size Effect on the Water-Mediated Interaction

Abstract

The nature of the solute-solute effective interaction in water depends on various microscopic properties of the solute molecules, such as size, shape, and solute-water attraction. There are numerous studies about the solute size effect on the water-mediated interaction, but how and why the strength of these interactions changes as the solute size increases remains unclear. Here, we compute the potentials $w(r)$ of mean force for pairs of solute particles with different diameters to quantify the strength of the water-mediated interactions varying with solute size. The oscillation of $w(r)$ depending on the inter-solute distance r reflects the structural change of water around the solute pair: There are characteristic hydrogen bond networks of water in the gap between two solutes when the inter-solute distances r are the monolayer- and bilayer-separated ones. We evaluate the enthalpic and entropic contributions to the effective pair potential $w(r)$ and clarify the thermodynamic factors determining the solute size dependence of $w(r)$ at specific separations r. The enthalpy change in decreasing the distance between two solutes from infinite separation to r is related to the distributions of the number of hydrogen bonds between water molecules near the solute pair. We also investigate the size effect when the solute is repellent with water molecules.

Publication

- Hidefumi Naito, Tomonari Sumi, and Kenichiro Koga, "The nature of the hydrophobic interaction varies as the solute size increases from methane's to C_{60}'s", *The Journal of Chemical Physics*, 2024, **161**, 214501 (14 pages).

3.1 INTRODUCTION

Water-mediated interactions are the solute-solute effective interactions in water or aqueous solution, which are qualitatively different from the intermolecular interaction in a vacuum. When the solutes are hydrophobic (hard to dissolve in water) or have hydrophobic moieties, the inter-solute effective interaction in water is referred to as the hydrophobic interaction.

The effective interaction between solute molecules in a solution is described by the potential $w(r)$ of mean force as a function of the distance r between two solutes. The excess part of $w(r)$ from the direct part $\phi(r)$ is the solvent-mediated potential $w^*(r) = w(r) - \phi(r)$. Figure 3.1 shows $w(r)$, $\phi(r)$, and $w^*(r)$ for methane in water. The first minimum of $w(r)$ quantifies the strength of effective interactions because, at this distance r, two solutes are in contact. The first maximum and the second minimum usually appear in $w(r)$ at larger r than the first minimum, and they are referred to as the desolvation barrier and the solvent-separated minimum, respectively.

The temperature effect on the water-mediated interaction is an important subject in physical chemistry. Based on the molecular simulation and theoretical calculation, the effective potentials $w(r)$ at different temperatures T have been calculated for various nonpolar solutes in water.[19], [21], [22], [24], [25], [33], [67], [77]–[92] These studies showed that the contact minimum of $w(r)$ decreases with increasing T, so the association of two nonpolar solutes in water would be the entropy-driven process. The enthalpy change in which two nonpolar solutes approach each other into the contact distance is positive at ambient temperature and pressure.[25], [67], [78]–[86], [88], [89], [91], [93]–[95]

The size effect on the nature of the solute-solute effective interaction in water are another central matter.[3]–[6], [16], [17], [33], [65]–[67], [73], [76], [77], [87], [96]–[100] Recent studies based on the molecular dynamics simulation showed that the contact minimum for pairs of Lennard-Jones (LJ) particles in water decreases with increasing LJ diameter σ, i.e., the water-mediated interaction becomes stronger as the particle size increases.[65], [76] On the other hand, the first maximum and the second minimum increase with increasing σ. It is characteristic that the latter, the solvent-separated minimum, disappears when σ is two

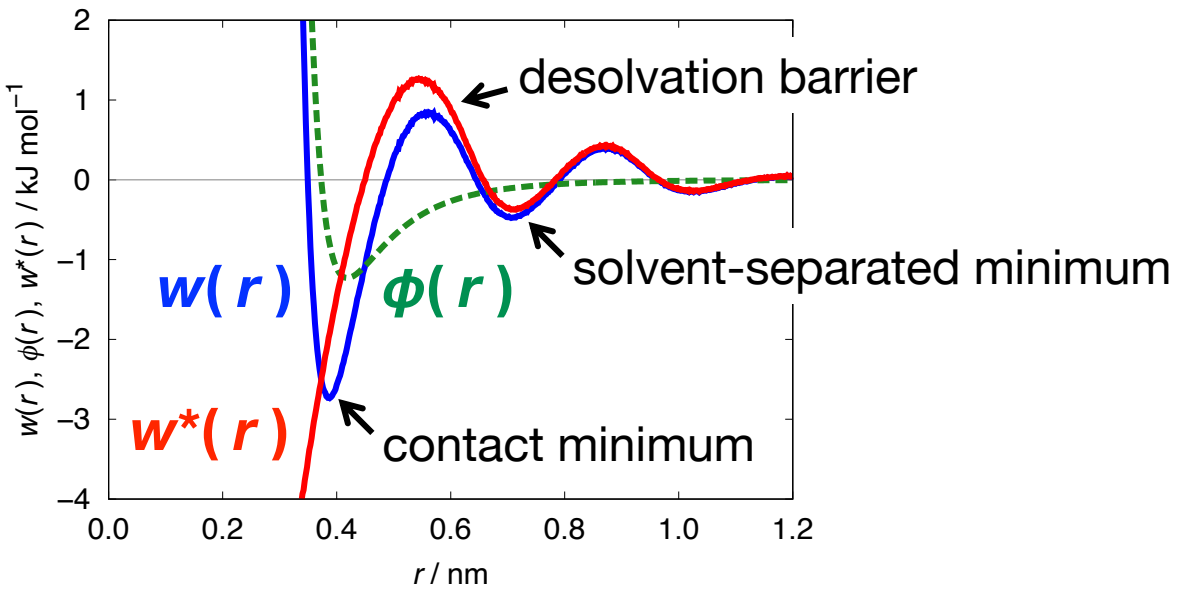

Figure 3.1: The simulation result of the effective potential $w(r)$ for pairs of methane-sized particles in water.[76] The horizontal axis is the methane-methane distance r. $\phi(r)$ is the Lennard-Jones (LJ) potential between methane-sized LJ particles, and $w^*(r) = w(r) - \phi(r)$ is the water-mediated part of $w(r)$. The first minimum, the first maximum, and the second minimum are called the contact minimum, the desolvation barrier, and the solvent-separated minimum, respectively.

times larger than the methane size.[65]

The present paper aims to clarify the thermodynamic and microscopic factors determining the solute size dependence of the water-mediated interaction, i.e., the σ dependence of the minima and maxima of the effective potential $w(r)$. We compute $w(r)$ as accurately as possible for nonpolar solutes of various sizes in water at different T. The enthalpic and entropic contributions to the effective potential are obtained from the temperature derivative of $w^*(r) = w(r) - \phi(r)$. Then, we analyze the solvation structures of the solute pair when the inter-solute separations are r of the minima and maxima of $w(r)$. These analyses make clear an anomalous behavior of water structures confined by two large solutes.

3.2 COMPUTATIONAL DETAILS

3.2.1 Molecular Dynamics Simulation

We performed the isobaric-isothermal molecular dynamics (MD) simulations for the system consisting of TIP4P/2005 water molecules[53] and spherical solute particles. The pair potential between two solute particles is represented by the Lennard-Jones (LJ) potential:

$$\phi(r) = 4\epsilon\left[\left(\frac{\sigma}{r}\right)^{12} - \left(\frac{\sigma}{r}\right)^{6}\right], \tag{3.1}$$

where ϵ and σ are the energy and size parameters, respectively. The reference values for σ and ϵ are $\sigma_{\mathrm{m}} = 0.373$ nm and $\epsilon_{\mathrm{m}} = 1.23$ kJ mol^{-1}, which are the TraPPE-UA force field for methane.[55] The solute LJ diameters are $\sigma^* \equiv \sigma/\sigma_{\mathrm{m}} = 1$, 1.5, 2, 2.5, and 3. The energy parameter ϵ is fixed to ϵ_{m} for all-size solutes. The LJ cross parameters between the solute particle and the oxygen atom of water molecules are given by the Lorentz-Berthelot combining rules.

We used GROMACS 2018 software[56] to perform MD simulations for the aqueous solutions. Periodic boundary condition was applied to the simulation box containing the solute and water molecules. The pressure is set to 1 bar using the Parrinello-Rahman method. The temperature T is controlled at $T = 270$, 300, 330, and 360 K by the Nosé-Hoover method. The number N of solute particles is $N = 40$ for $\sigma^* = 1$, $N = 20$ for $\sigma^* = 1.5$, and $N = 2$ for $\sigma^* = 2$, 2.5, and 3. The N_{w} of water molecules is $N_{\mathrm{w}} = 4000$ for $\sigma^* = 1$ and 1.5, and $N_{\mathrm{w}} = 8000$ for $\sigma^* = 2$, 2.5, and 3. The duration time t of the production run to compute the radial distribution function $g(r)$ is $t = 100$ ns for $\sigma^* = 1$ and $t = 200$ ns for $\sigma^* = 1.5$. The solute-solute effective potential $w(r)$ is then obtained from $w(r) = -kT \ln g(r)$, where k is Boltzmann's constant. For the systems with $N = 2$, we performed the umbrella sampling simulations[57, 58] to evaluate $w(r)$. In these simulations, t is 20 ns for each window. The time step interval is 1 fs for each simulation. The configurations of solute particles and water molecules were recorded every 0.05 ps.

When we performed molecular simulations for the solutions of the solutes with $\sigma^* = 1$ and 1.5, the pair potential $\phi(r)$ between two solutes was a repulsive potential $\phi_{\mathrm{rep}}(r)$

instead of $\phi(r)$ to calculate $g(r)$ at solute-infinite dilution. The relation between $g_{\rm rep}(r)$ and $g(r)$, the former is obtained from the simulation using $\phi_{\rm rep}(r)$, is

$$g(r) = g_{\rm rep}(r) \exp\left[-\frac{\phi_{\rm att}(r)}{kT}\right] \tag{3.2}$$

with $\phi_{\rm att}(r) = \phi(r) - \phi_{\rm rep}(r)$. For $\sigma^* = 1$, $\phi_{\rm rep}(r)$ is the repulsive part of the Weeks-Chandler-Andersen (WCA) potential.[54] For $\sigma^* = 1.5$, $\phi_{\rm rep}(r)$ is taken to be $4\epsilon(\sigma/r)^{12}$.

The cutoff distance $r_{\rm cut}$ for truncating the solute-solute, solute-water, and water-water LJ potentials depends on the diameter of the solute particle: $r_{\rm cut} = 1.3$ nm for $\sigma^* = 1$ and 1.5, $r_{\rm cut} = 2$ nm for $\sigma^* = 2$ and 2.5, and $r_{\rm cut} = 2.4$ nm for $\sigma^* = 3$. The particle mesh Ewald method is used to calculate the long-range part of the Coulomb potential between water molecules. The real-space cutoff distance is the same as $r_{\rm cut}$ for the LJ potential.

The inter-solute distances were constrained via the harmonic potential during the umbrella sampling simulations. The spring constant is 1000 kJ mol^{-1} nm^{-2}. For the solute with $\sigma^* = 2$, the constraint distance ranges from 0.6 to 2.9 nm in 0.1 nm increments. Similarly, that is from 0.7 to 2.8 nm for $\sigma^* = 2.5$ and from 0.8 to 3.1 nm for $\sigma^* = 3$. The inter-solute effective potentials $w(r)$ were then obtained from the 22 or 24 umbrella windows using the weighted histogram analysis method.[59], [60]

We also investigate the effect of the solute-water attraction on the water-mediated interaction. A previous study showed that the contact minimum of $w(r)$ rapidly decreases with increasing σ^* when the solute is repellent with water molecules.[65] Here, we denote the WCA solute as the solute particle interacting with the oxygen atom of water molecules via the repulsive WCA potential. The umbrella sampling simulations were performed to compute $w(r)$ for the WCA solutes with $\sigma^* = 1$, 2, and 3 in water. The pressure is fixed at 1 bar, but the temperature is controlled at $T = 270$, 300, and 330 K. The number of water molecules is 8000. The inter-solute distance was constrained in the simulations, ranging from 0.2 to 2.5 nm for $\sigma^* = 1$, from 0.6 to 2.9 nm for $\sigma^* = 2$, and from 0.8 to 3.1 nm for $\sigma^* = 3$.

3.2.2 Energetic Analysis

The effective potential $w(r)$ for pairs of solutes in a solvent consists of the direct part $\phi(r)$ and the indirect part $w^*(r) = w(r) - \phi(r)$. The latter corresponds to the difference between the solvation free energy of a pair of solutes with their separation being r and two times the solvation free energy of a single solute.[1] Therefore, the solvent-mediated potential $w^*(r)$ is the free energy change and can be expressed as the sum of the enthalpic and entropic terms, i.e., $w^*(r) = \Delta h^*(r) - T\Delta s^*(r)$. The temperature derivative of $w^*(r)$ at fixed pressure gives the enthalpy and entropy changes at each distance r:

$$\Delta h^*(r) = \left[\frac{\partial(w^*(r)/T)}{\partial(1/T)}\right]_p, \tag{3.3}$$

$$\Delta s^*(r) = -\left[\frac{\partial w^*(r)}{\partial T}\right]_p. \tag{3.4}$$

In the present study, three temperatures (270, 300, and 330 K) are taken into account for a linear fit to $w^*(r)$ against T:

$$w^*_{\text{fit}}(r) = Ta_1(r) + a_0(r). \tag{3.5}$$

In the case of the LJ solutes, i.e., solute particles interacting with water molecules via the LJ potentials, we also obtain a quadratic fit of $w^*(r)$ using the simulation data at $T = 270$, 300, 330, and 360 K:

$$w^*_{\text{fit}}(r) = T^2b_2(r) + Tb_1(r) + b_0(r). \tag{3.6}$$

Then, we calculate the enthalpic and entropic contributions to $w^*(r)$ at $T = 300$ K via

$$\Delta h^*(r) = \begin{cases} a_0(r) & \text{(linear fit)} \\ -T^2b_2(r) + b_0(r) & \text{(quadratic fit)}, \end{cases} \tag{3.7}$$

and

$$-T\Delta s^*(r) = \begin{cases} Ta_1(r) & \text{(linear fit)} \\ 2T^2 b_2(r) + Tb_1(r) & \text{(quadratic fit).} \end{cases} \tag{3.8}$$

Note that $\Delta h^*(r)$ obtained from a linear fit to $w^*(r)$ has no T dependence.

The enthalpy change $\Delta h^*(r)$ is now the difference between $h^*(r)$ and $h^*(r \to \infty)$, where $h^*(r)$ is the solvation enthalpy of a pair of solute particles with fixed separation r. $h^*(r)$ consists of the configuration energy $U(r)$ of the aqueous solution of the solute pair and the product of the pressure and the volume change. We ignore the volume change of the system associated with decreasing the solute-solute separation from infinity to r, then $h^*(r)$ is expressed as

$$h^*(r) = U_{\mathrm{sw}}(r) + U_{\mathrm{ww}}(r), \tag{3.9}$$

where $U_{\mathrm{sw}}(r)$ is the sum of the pair interaction energy between the solute pair and water molecules, and $U_{\mathrm{ww}}(r)$ is that between water molecules. Therefore,

$$\Delta h^*(r) = \Delta U_{\mathrm{sw}}(r) + \Delta U_{\mathrm{ww}}(r), \tag{3.10}$$

where Δ means the change in the process of decreasing the distance between two solute particles from infinite separation to r.

To obtain $\Delta U_{\mathrm{sw}}(r)$ in Eq. (3.10), additional isobaric-isothermal MD simulations were performed. The target system is the aqueous solutions of a pair of solute particles with LJ diameters $\sigma^* = 1$, 1.5, 2, 2.5, and 3. The number N_{w} of water molecules is 8000. The inter-solute separation R was fixed to r of the first minimum, the first maximum, the second minimum, the second maximum, and the third minimum of $w(r)$. Table 3.1 shows R for $\sigma^* = 1$, 1.5, 2, 2.5 and 3. The pressure and temperature are maintained at 1 bar and 300 K, respectively. The duration time of the production run is 20 ns for each simulation. The configurations of solute particles and water molecules were sampled every 1 ps to calculate the sum $U_{\mathrm{sw}}(r)$ of the solute-water pair interaction energy. We also performed MD simulations for the model solutions consisting of a single solute particle

Table 3.1: The fixed inter-solute separations R of the first minimum, the first maximum, the second minimum, the second maximum, and the third minimum of $w(r)$ for pairs of LJ solutes with $\sigma^* = 1$, 1.5, 2, 2.5, and 3 at $T = 300$ K.

	R / nm				
σ^*	1st minimum	1st maximum	2nd minimum	2nd maximum	3rd minimum
1	0.388	0.562	0.706	0.874	1.026
1.5	0.562	0.786	0.904	1.046	1.204
2	0.724	0.992	1.114	1.230	1.414
2.5	0.886	1.206	1.328	1.460	1.650
3	1.032	1.400	1.506	1.570	1.764

and 4000 water molecules to obtain $U_{\mathrm{sw}}(r \to \infty) = 2U_{\mathrm{s_1w}}$, where $U_{\mathrm{s_1w}}$ is the sum of the pair interaction energy between one solute and water molecules. Then, we obtain $\Delta U_{\mathrm{sw}}(r) = U_{\mathrm{sw}}(r) - 2U_{\mathrm{s_1w}}$, and consider the change $\Delta U_{\mathrm{ww}}(r)$ of the sum of the water-water pair interaction energy as the difference between $\Delta h^*(r)$ and $\Delta U_{\mathrm{sw}}(r)$.

3.2.3 Structural Analysis

Previous studies calculated the cylindrical distributions of water molecules around the solute pair and investigated the microscopic structure of water.[4], [5], [85], [89], [99], [100] Figure 3.2 is a schematic representation of the cylindrical coordinate system defined by the variables h, d, and θ. Based on this system, we calculate the distribution $g_{\mathrm{cyl}}(h, d)$ of the oxygen atoms of water molecules and the number $N_{\mathrm{HB}}(h, d)$ of hydrogen bonds between water molecules per one molecule. Both quantities are averaged over the azimuth θ and are depicted on the h-d plane. The two-dimensional distributions $g_{\mathrm{cyl}}(h, d)$ of water molecules are normalized to 1 in the bulk region. Two water molecules form one hydrogen bond if the distance r_{OO} between their oxygen atoms is less than 0.35 nm and the H-O$\cdots$O angle is less than or equal to 30 degrees.[101]–[103] We focus on how $g_{\mathrm{cyl}}(h, d)$ and $N_{\mathrm{HB}}(h, d)$ vary with the solute size. We also performed the molecular simulation of the solute pair with $R = 3$ nm to calculate $g_{\mathrm{cyl}}(h, d)$ and $N_{\mathrm{HB}}(h, d)$ when two solute particles are far enough apart.

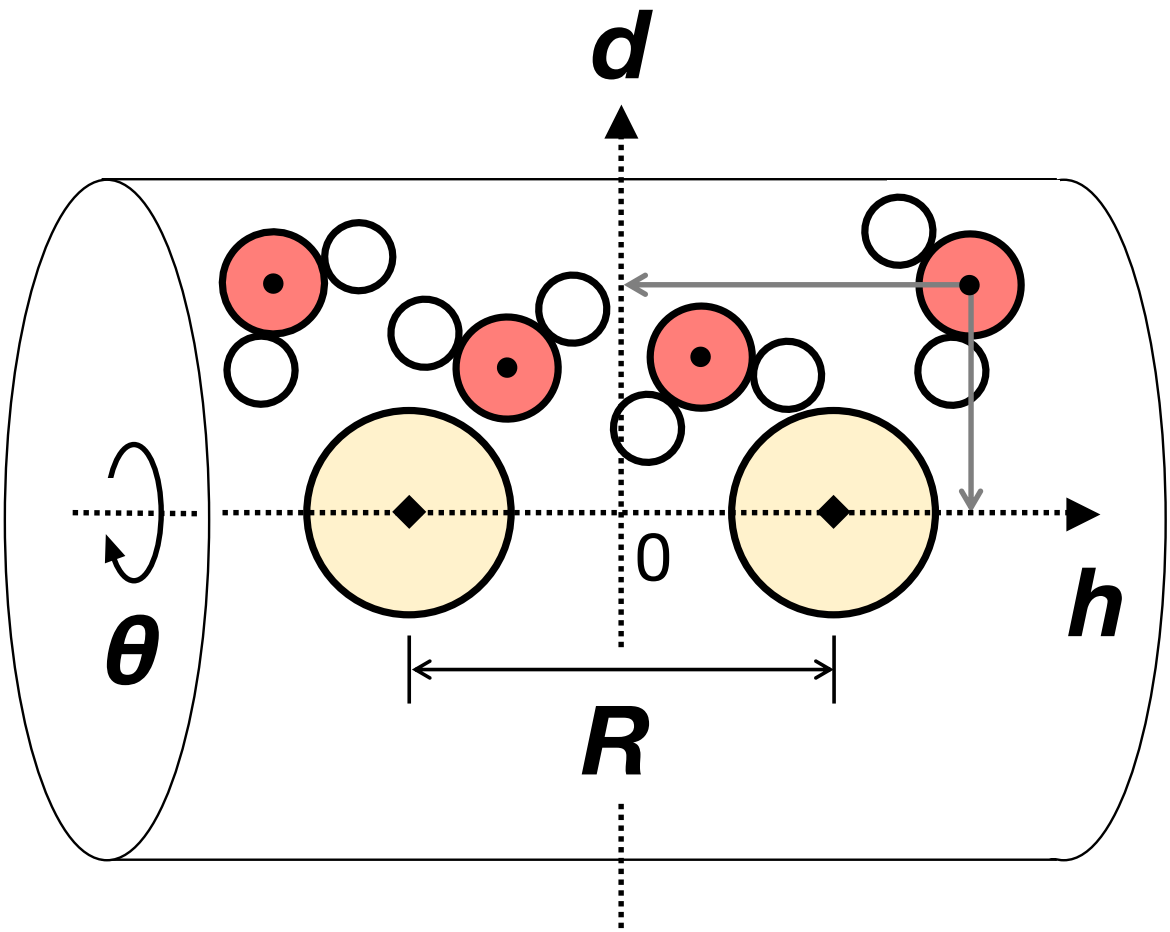

Figure 3.2: Schematic representation of water molecules around a pair of solute particles in the cylindrical coordinate system defined by the independent variables h, d, and θ. The horizontal axis h passes through two centers of the solutes (yellow circles). The vertical axis d is perpendicular to h, and θ is the azimuth. The axes h and d intersect at the midpoint of two centers of the solutes. The red circles represent the oxygen atoms of water molecules. Reproduced from "H. Naito, T. Sumi, and K. Koga, *J. Chem. Phys.*, Vol. 161, doi: 10.1063/5.0233808 (2024)", with the permission of AIP Publishing.

3.3 RESULTS AND DISCUSSION

3.3.1 Lennard-Jones Solute

Potentials of Mean Force

First, we examine the temperature effects on the solute-solute effective interaction in water. Figures 3.3(a)-(c) show the potentials $w(r)$ of mean force for pairs of LJ particles in water at the temperatures T = 270, 300, 330, and 360 K. The particle diameters σ^* are 1 (methane size), 2, and 3 (C_{60} fullerene size). The first minimum of $w(r)$ descends with increasing T for each-sized particle. This result suggests that the decrement of the distance between two solutes in water from an infinite separation to the contact distance is entropy-driven, consistent with previous studies.[25], [67], [78]–[85], [88], [89], [91], [93]–[95] For the solutes with $\sigma^* = 2$ and 3, the first maximum of $w(r)$ also decreases with increasing T, indicating that the rise in temperature affects the solute-solute effective interaction over a longer range of r than the contact distance.

Distributions of Water Molecules Around Solute Pairs

The microscopic structure of water around a solute pair changes depending on the solute-solute distance r. Figure 3.4 shows the normalized two-dimensional distributions $g_{\rm cyl}(h, d)$ of water molecules around a pair of LJ particles. The inter-particle separation R is fixed at particular six values for each particle. These distributions are normalized to 1 in the bulk region. The particle diameters σ^* are 1, 2, and 3.

When two particles are 3 nm apart [Figure 3.4(a)], each particle is surrounded by the first solvation shell of water (bright-colored ring). The local density of water in the solvation shell is higher than the bulk density: $g_{\rm cyl}(h, d)$ in the shell is approximately 2.0 for $\sigma^* = 1$, 1.7 for $\sigma^* = 2$, and 1.6 for $\sigma^* = 3$.

As the solute-solute separation decreases from 3 nm to r of the third minimum of $w(r)$, we find two peaks in the region between two solute particles [Figure 3.4(b)]. Since the solute pair is separated by the bilayer structure of water, we call the third minimum the *bilayer-separated minimum*. This bilayer structure disappears at r of the second maximum

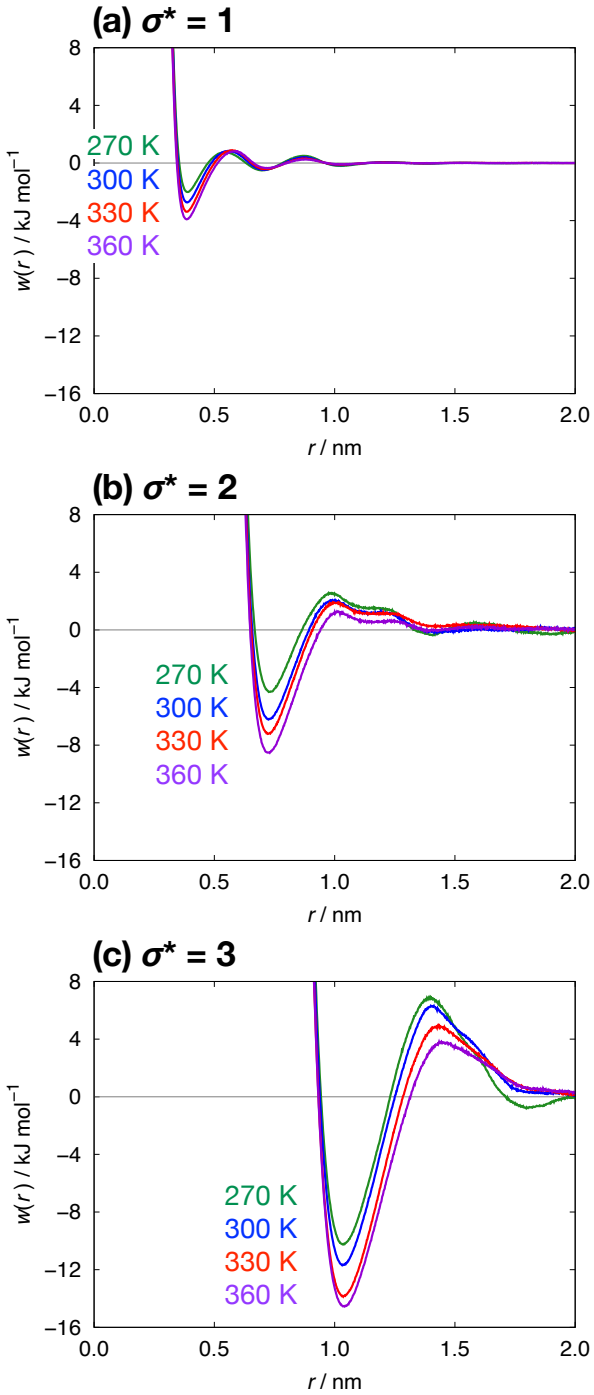

Figure 3.3: The effective potentials $w(r)$ for pairs of Lennard-Jones (LJ) particles of different diameters in water at four temperatures T. The particle diameters σ^* are (a) 1 (methane size), (b) 2, and (c) 3 (C_{60} fullerene size). Each curve shows the result at $T = 270$ K (green), 300 K (blue), 330 K (red), and 360 K (violet), respectively.

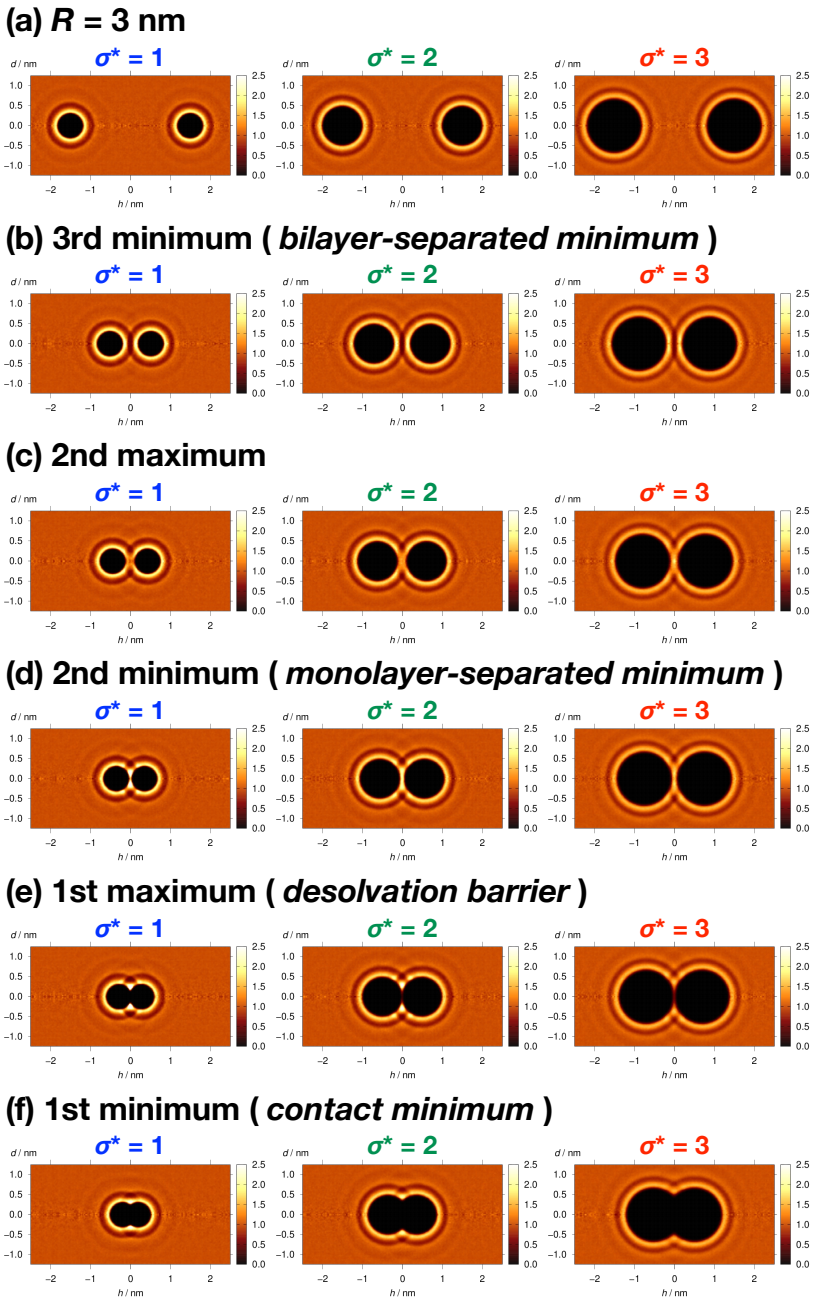

Figure 3.4: The normalized two-dimensional distributions $g_{\mathrm{cyl}}(h, d)$ of water molecules around a pair of LJ particles. $g_{\mathrm{cyl}}(h, d)$ is normalized to 1 in the bulk region. Two solute particles with $\sigma^* = 1$ (left), 2 (middle), and 3 (right) are displayed in black. The solute-solute separation R is fixed to (a) 3 nm, or to r of (b) the third minimum (*bilayer-separated minimum*), (c) the second maximum, (d) the second minimum (*monolayer-separated minimum*), (e) the first maximum (*desolvation barrier*), and (f) the first minimum (*contact minimum*), of $w(r)$ for each-sized particle (see Table 3.1). Reproduced from "H. Naito, T. Sumi, and K. Koga, *J. Chem. Phys.*, Vol. 161, doi: 10.1063/5.0233808 (2024)", with the permission of AIP Publishing.

of $w(r)$ due to the partial overlap of the two solvation shells [Figure 3.4(c)]. The water density inside the gap between the two particles is low compared to the density of water molecules in the solvation shell outside the gap.

When the distance between solute particles is r of the second minimum of $w(r)$, the solute pair is separated by the monolayer structure of water [Figure 3.4(d)]. Previous studies found a similar structural change from bilayer to monolayer structure in the hydrogen bonding network of water confined by two hydrophobic sheets[92], [104]–[106] or two C_{60} fullerenes.[86] The second minimum of $w(r)$ is usually called the solvent-separated minimum, but here, we refer to this minimum as the *monolayer-separated minimum* to distinguish it from the bilayer-separated minimum. The local density inside the monolayer structure is higher than outside: The distribution $g(0,0)$ at the midpoint of the solute pair is approximately 2.4 for $\sigma^* = 1$, 2.1 for $\sigma^* = 2$, and 1.7 for $\sigma^* = 3$.

With decreasing the inter-particle distance to r of the first maximum of $w(r)$, $g_{\mathrm{cyl}}(h,d)$ at the midpoint diminishes [Figure 3.4(e)]: $g(0,0)$ is approximately 0, 0.4, and 0.6 for $\sigma^* = 1$, 2, and 3, respectively, indicating that water molecules are scarce in between two particles at r of the *desolvation barrier*. Finally, two solutes are in contact at the first minimum of $w(r)$ [Figure 3.4(f)], so this minimum is called the *contact minimum*.

Enthalpic and Entropic Contributions to the Water-Mediated Potentials

Next, we study the size effect on the water-mediated interaction between two solutes. Figure 3.5 displays the water-mediated potentials $w^*(r)$ for LJ particles with $\sigma^* = 1$, 1.5, 2, 2.5, and 3 at $T = 300$ K. $w^*(r)$ is defined as the difference between the effective potential $w(r)$ and the direct pair potential $\phi(r)$, the latter is also plotted in Figure 3.5. Subtracting $\phi(r)$ from $w(r)$ obscures the first minimum of $w(r)$, but other minima and maxima remain in $w^*(r)$.

Figure 3.6 shows $w^*(r)$ at r of the contact minimum, the desolvation barrier, the monolayer-separated minimum, and the bilayer-separated minimum of $w(r)$ as a function of the particle diameter σ^*. One can see three different σ^* dependencies: With increasing particle size, the contact minimum decreases, the desolvation barrier and the monolayer-

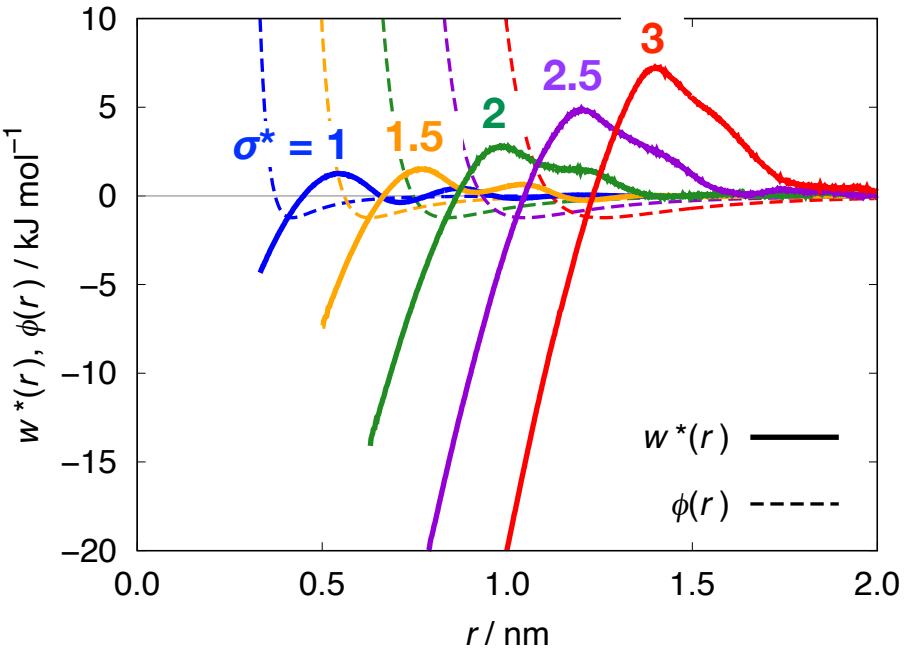

Figure 3.5: The water-mediated potentials $w^*(r)$ for pairs of LJ particles at $T = 300$ K. The solute diameter σ^* varies from 1 to 3 in 0.5 increments. $w^*(r)$ (solid curve) is defined as the excess part of the effective potential $w(r)$ by subtracting the solute-solute pair potential $\phi(r)$ (dashed curve) from $w(r)$. Reproduced from "H. Naito, T. Sumi, and K. Koga, *J. Chem. Phys.*, Vol. 161, doi: 10.1063/5.0233808 (2024)", with the permission of AIP Publishing.

separated minimum increase, and the bilayer-separated minimum barely changes from zero. The present paper aims to elucidate the thermodynamic and microscopic factors determining these size dependence.

Firstly, we investigate the thermodynamic factor. The enthalpic and entropic contributions, $\Delta h^*(r)$ and $-T\Delta s^*(r)$, to $w^*(r)$, are obtained from a temperature derivative of $w^*(r)$. Figures 3.7(a) and (b) display $\Delta h^*(r)$ and $-T\Delta s^*(r)$ for $\sigma^* = 1$, 1.5, 2, 2.5, and 3 at $T = 300$ K. Both curves show the fluctuating behavior as a function of the distance r between two solute particles. Here, we focus on $w^*(r)$, $\Delta h^*(r)$, and $-T\Delta s^*(r)$ at particular values of r.

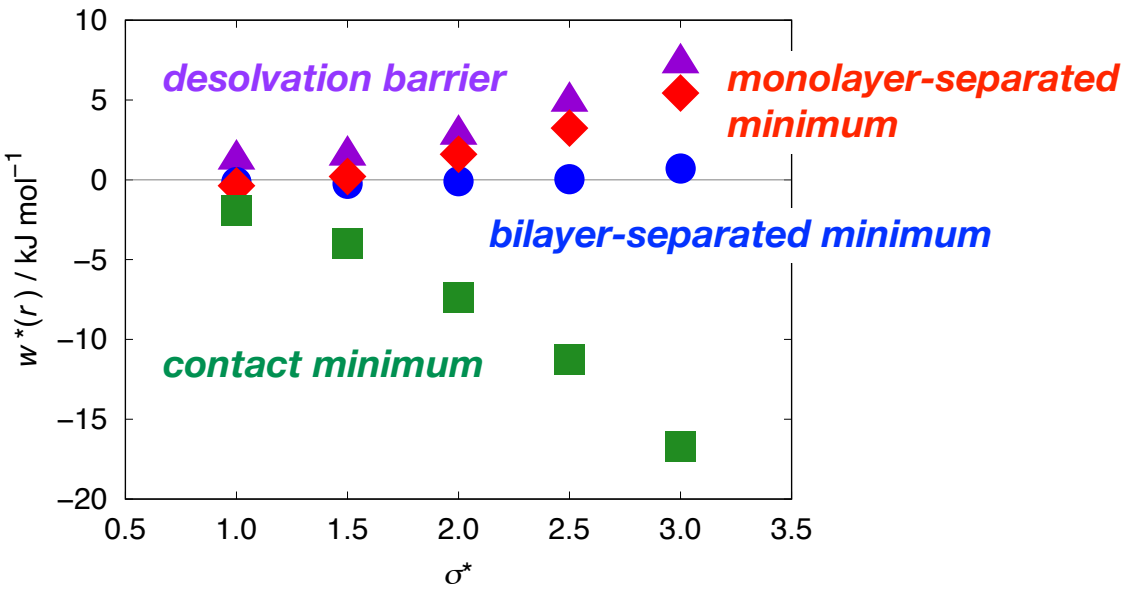

Figure 3.6: The particle size dependence of the water-mediated interactions between LJ particles at $T = 300$ K. Blue circles, red diamonds, violet triangles, and green squares represent $w^*(r)$ at the inter-particle distances r of the bilayer-separated minimum, the monolayer-separated minimum, the desolvation barrier, and the contact minimum of $w(r)$, respectively.

Solute Size Dependence of $w^*(r) = \Delta h^*(r) - T\Delta s^*(r)$

Figure 3.8(a) shows the σ^* dependence of $w^*(r)$, $\Delta h^*(r)$, and $-T\Delta s^*(r)$ at r of the bilayer-separated minimum of $w(r)$. The temperature derivative of a quadratic fit to $w^*(r)$ against T gives the enthalpy and entropy changes. Although $w^*(r)$ at the bilayer-separated minimum does not vary with the particle size, $\Delta h^*(r)$ and $-T\Delta s^*(r)$ largely depend on σ^* and have opposite trends against σ^*: $\Delta h^*(r)$ is negative and decreases with increasing σ^*, while $-T\Delta s^*(r)$ is positive and increases with σ^*. Both contributions largely cancel out, so the resulting $w^*(r)$ is nearly zero for all size solutes. For example, in the case of the largest solute with $\sigma^* = 3$, $\Delta h^*(r) = -6.42$ kJ mol^{-1} and $-T\Delta s^*(r) = 7.14$ kJ mol^{-1}, so $w^*(r) = \Delta h^*(r) - T\Delta s^*(r) = 0.72$ kJ mol^{-1}. The signs of $\Delta h^*(r)$ and $-T\Delta s^*(r)$ are consistent with the result for the effective interactions between two graphene plates[106] and two C_{60} fullerenes[86] in water, but in both cases, the magnitude of $\Delta h^*(r)$ is greater than that of $-T\Delta s^*(r)$, so the resulting free energy change is negative.

Figure 3.8(b) displays $w^*(r)$, $\Delta h^*(r)$, and $-T\Delta s^*(r)$ obtained from a linear fit to $w^*(r)$

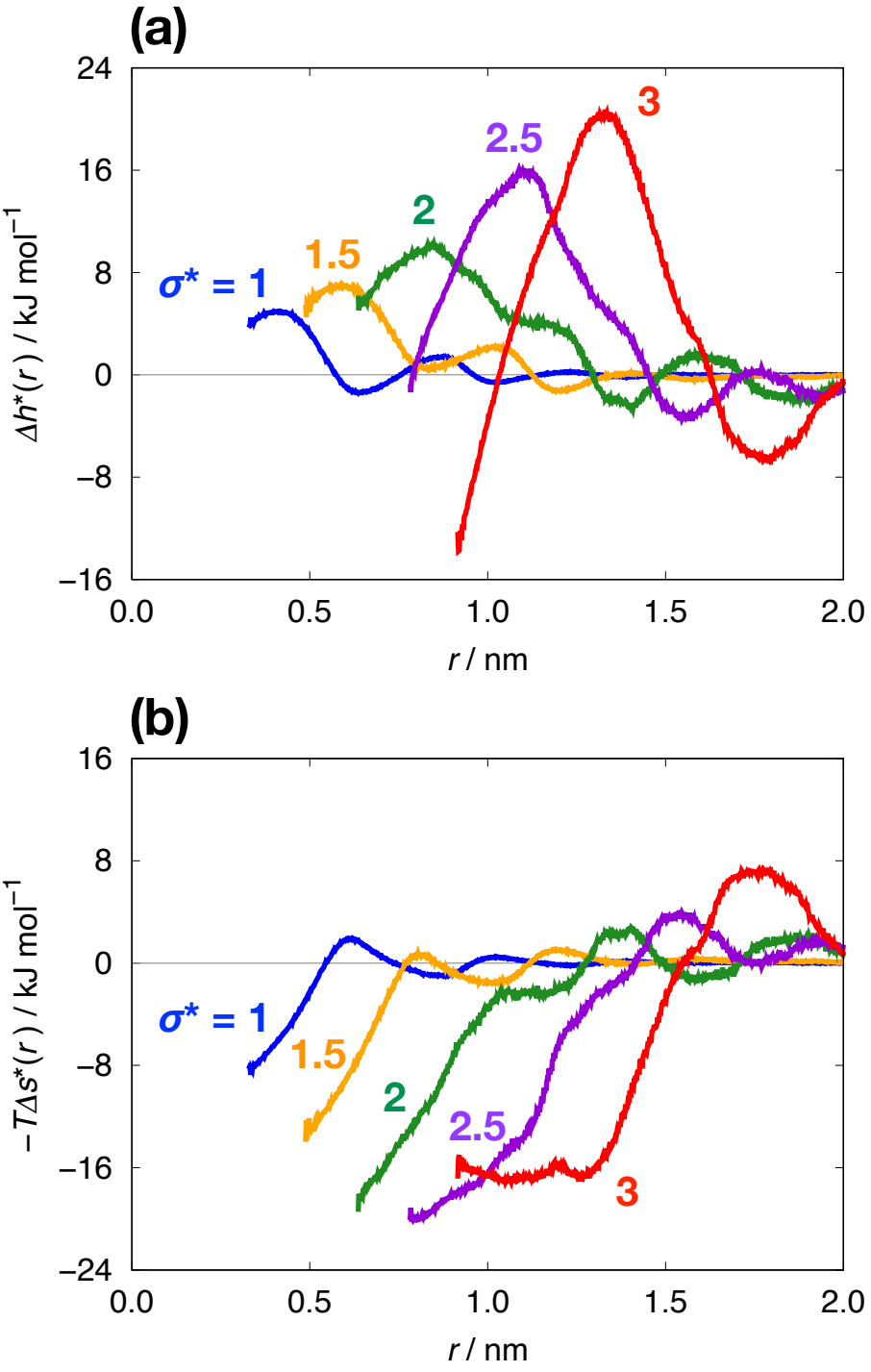

Figure 3.7: The enthalpic and entropic contributions, $\Delta h^*(r)$ and $-T\Delta s^*(r)$, to the water-mediated potentials $w^*(r)$ for LJ particles with $\sigma^* = 1$, 1.5, 2, 2.5, and 3 at $T = 300$ K. (a) $\Delta h^*(r)$ and (b) $-T\Delta s^*(r)$ are obtained from a quadratic fit of $w^*(r)$ as a function of T. Reproduced from "H. Naito, T. Sumi, and K. Koga, *J. Chem. Phys.*, Vol. 161, doi: 10.1063/5.0233808 (2024)", with the permission of AIP Publishing.

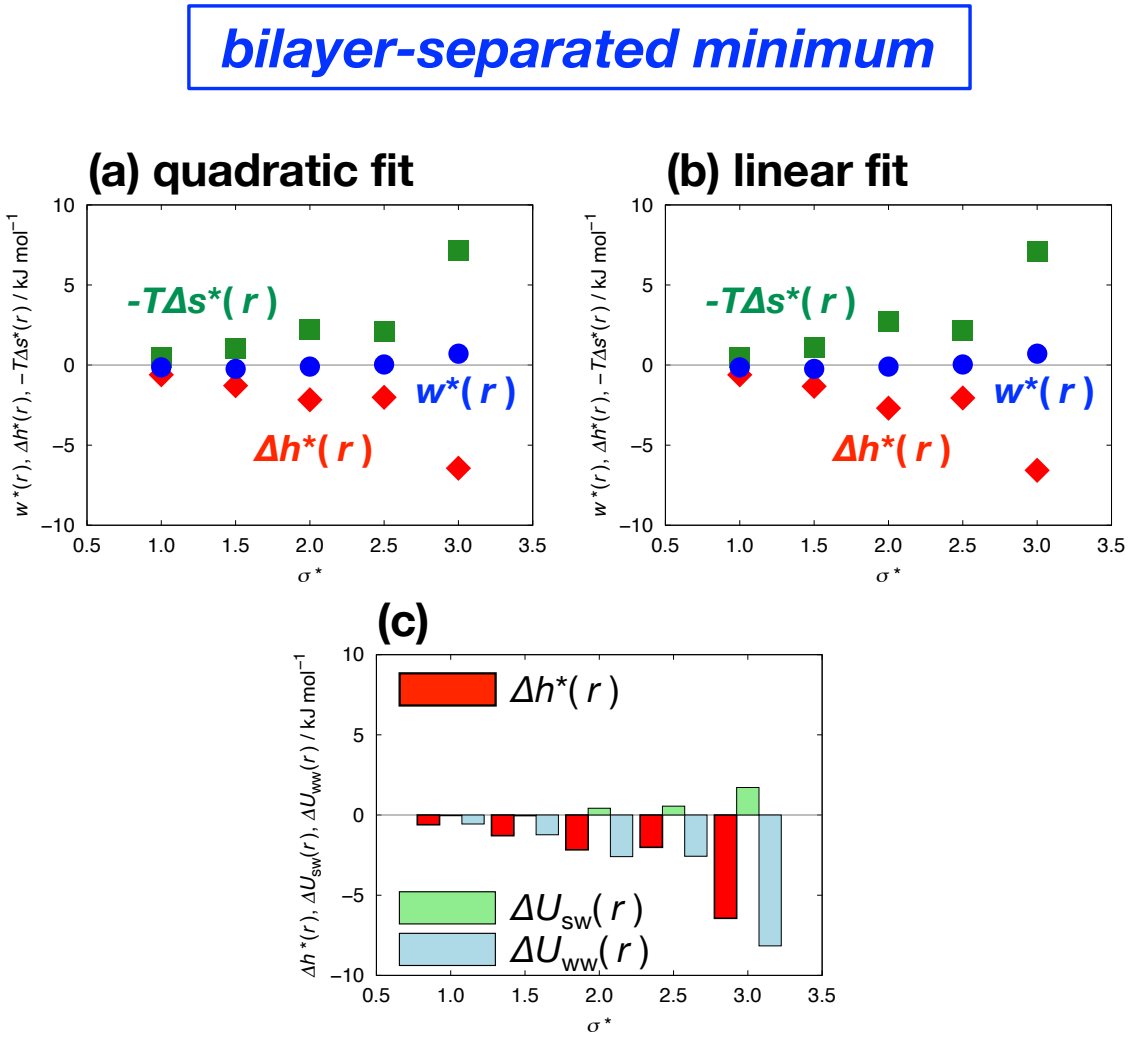

Figure 3.8: The particle size dependence of $w^*(r)$, $\Delta h^*(r)$, and $-T\Delta s^*(r)$ at r of the bilayer-separated minimum of $w(r)$ for LJ particles at $T = 300$ K. The particle diameter σ^* ranges from 1 to 3. (a) The results of a quadratic fit to $w^*(r)$ against T using the data at $T = 270$, 300, 330, and 360 K. Blue circles, red diamonds, and green squares represent $w^*(r)$, $\Delta h^*(r)$, and $-T\Delta s^*(r)$, respectively. (b) $w^*(r)$, $\Delta h^*(r)$, and $-T\Delta s^*(r)$ obtained from a linear fit to $w^*(r)$ against T using the data at $T = 270$, 300, and 330 K. (c) The σ^* dependence of $\Delta h^*(r) = \Delta U_{\rm sw}(r) + \Delta U_{\rm ww}(r)$. Here, $\Delta U_{\rm sw}(r)$ and $\Delta U_{\rm ww}(r)$ are the changes in the sums of the solute-water and water-water pair interaction energies, respectively, as the solute-solute distance decreases from infinite separation to r. Red, light-green, and light-blue bars represent $\Delta h^*(r)$, $\Delta U_{\rm sw}(r)$, and $\Delta U_{\rm ww}(r)$, respectively. Reproduced from "H. Naito, T. Sumi, and K. Koga, *J. Chem. Phys.*, Vol. 161, doi: 10.1063/5.0233808 (2024)", with the permission of AIP Publishing.

against T. A comparison of Figures 3.8(a) and (b) indicates that there is little difference between the two results: $\Delta h^*(r)$ from a quadratic fit is -0.60, -1.28, -2.17, -2.01, and -6.44 kJ mol^{-1} for $\sigma^* = 1$, 1.5, 2, 2.5, and 3, respectively, while $\Delta h^*(r)$ from a linear fit is -0.61, -1.33, -2.69, -2.05, and -6.57 kJ mol^{-1} for each-size particle. These results suggest that the enthalpy change in which two solute particles approach each other has little temperature dependence.

Now we consider the size effect on the enthalpic contribution $\Delta h^*(r)$ to $w^*(r)$ by dividing it into two parts, $\Delta U_{\rm sw}(r)$ and $\Delta U_{\rm ww}(r)$: $U_{\rm sw}(r)$ is the sum of the pair interaction energy between the solute pair and water molecules, $U_{\rm ww}(r)$ is the sum of the pair interaction energy between the water molecules, and Δ denotes the change in the process of decreasing the inter-particle distance from infinity to r. Figure 3.8(c) is a bar graph of $\Delta h^*(r) = \Delta U_{\rm sw}(r) + \Delta U_{\rm ww}(r)$ for LJ particles with $\sigma^* = 1$, 1.5, 2, 2.5, and 3. $\Delta U_{\rm sw}(r)$ at the bilayer-separated minimum is almost zero for $\sigma^* = 1$, but it becomes slightly larger with increasing σ^*. On the other hand, $\Delta U_{\rm ww}(r)$ is negative and decreases as the particle size increases. The decrease of $\Delta h^*(r)$ with σ^* is thus due to that of $\Delta U_{\rm ww}(r)$, indicating that the bilayer structure of water becomes more energetically stable with increasing particle size.

The negative $\Delta U_{\rm ww}(r)$ means that the stability of the water structure is greater when two solutes are bilayer-separated than they are far apart. This result is consistent with the normalized distributions $g_{\rm cyl}(h, d)$ of water molecules around the solute pair. Fig. 3.4(b) indicates that the local density of water in the bilayer structure is higher than that in the first solvation shell of the solute: The former is $g_{\rm cyl}(h, d) \simeq 2.3$, 2.1, and 1.8 for the particle with $\sigma^* = 1$, 2, and 3, respectively, while the latter is $g_{\rm cyl}(h, d) \simeq 2.0$, 1.7, and 1.6 for each particle.

The entropic contribution $-T\Delta s^*(r)$ to the bilayer-separated minimum is positive and increases with σ^*, and it cancels out the enthalpic stabilization of the bilayer-separated pair. One of the microscopic factors of the positive $-T\Delta s^*(r)$ would be the decrease of the translational entropy of water molecules inside the bilayer structure. Here, we calculate the following quantity $D_{\rm w}$ to measure the diffusion of water molecules around a pair of

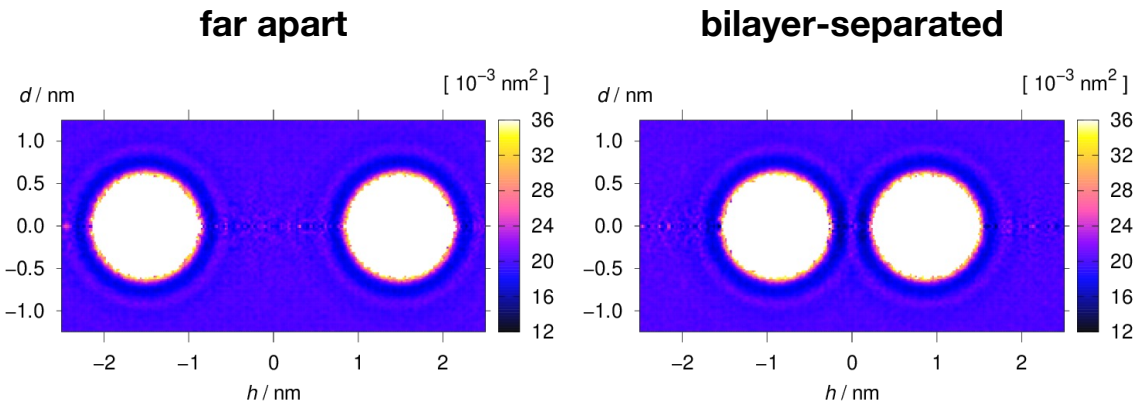

Figure 3.9: The distribution $D_{\mathrm{w}}(h, d)$ of the mean square displacement of water molecules around the solute pair per 1 ps in the cylindrical coordinate system. Two solute particles with the diameter $\sigma^* = 3$ are displayed in white. The inter-particle distance is 3 nm (left) and 1.764 nm (right), the latter corresponding to the bilayer-separated distance of the effective pair potential $w(r)$ for the LJ solute with $\sigma^* = 3$.

the LJ solutes with $\sigma^* = 3$:

$$D_{\mathrm{w}} = \left\langle |\boldsymbol{r}_i(t + dt) - \boldsymbol{r}_i(t)|^2 \right\rangle \quad \text{with } dt = 1 \text{ ps}, \tag{3.11}$$

where $\boldsymbol{r}_i(t) = (x_i(t), y_i(t), z_i(t))$ is the three-dimensional coordinate of a water molecule i at the time t, and $\langle \cdots \rangle$ denotes the statistical average of all water molecules and the time average. D_{w} is the mean square displacement of the water molecule per 1 ps.

Fig. 3.9 shows the spatial distribution of D_{w} in the cylindrical coordinate system. One can see that $D_{\mathrm{w}}(h, d)$ of the bilayer-separated pair has slightly black-colored lines, indicating that the mean square displacement of the water molecule inside the bilayer structure is smaller than that in the solvation shell. Therefore, the entropic destabilization of the bilayer-separated pair would be due to the slow diffusion of the water molecule confined by two solute particles.

Next, we see the particle size effect on the monolayer-separated minimum of $w(r)$. Figures 3.10(a) and (b) show the σ^* dependence of $w^*(r)$, $\Delta h^*(r)$, and $-T\Delta s^*(r)$ at r of the monolayer-separated minimum. For the solutes with $\sigma^* \geq 1.5$, $\Delta h^*(r)$ is positive while $-T\Delta s^*(r)$ is negative, consistent with the simulation result of two graphene plates

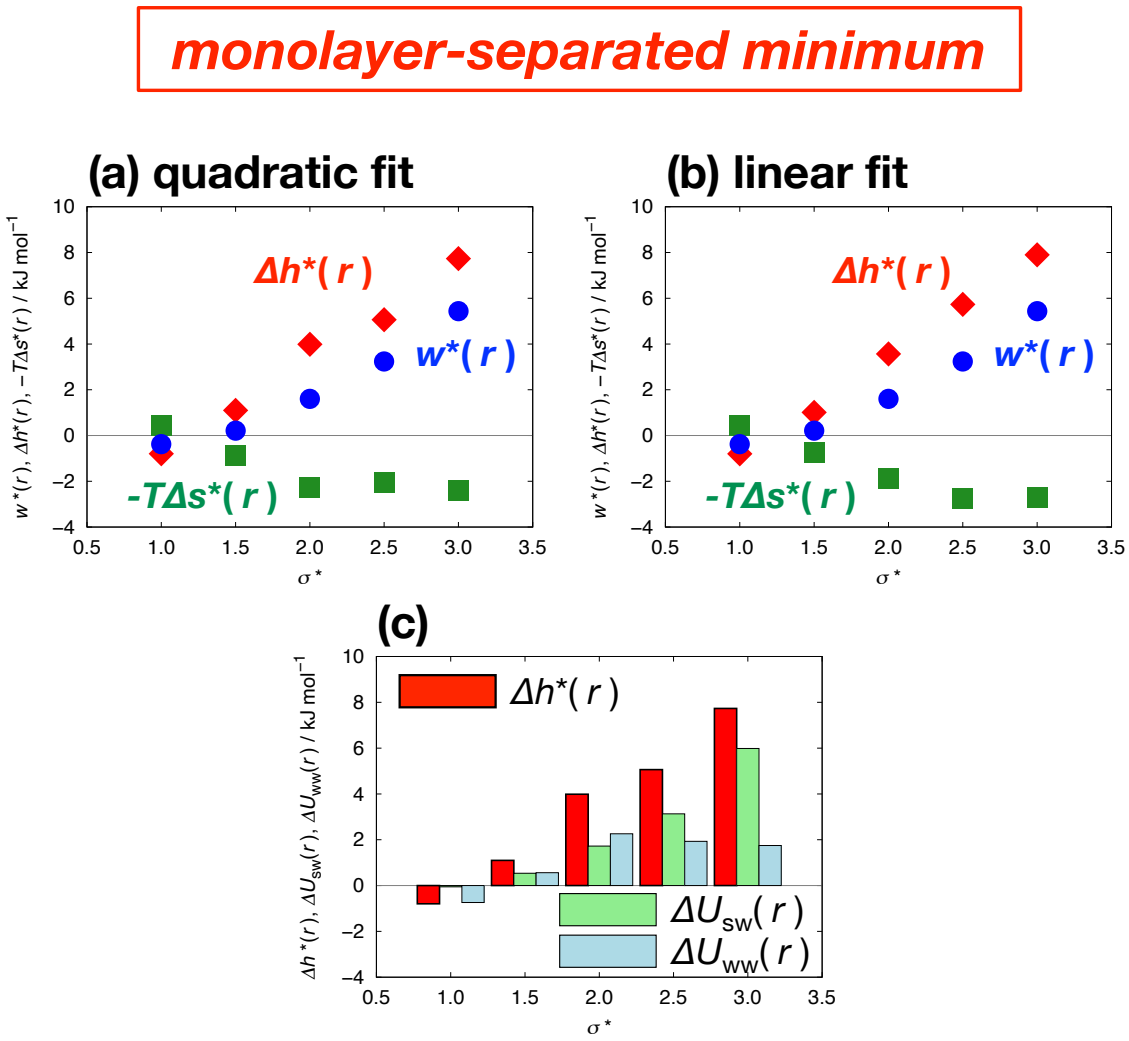

Figure 3.10: The particle size dependence of $w^*(r)$, $\Delta h^*(r)$, and $-T\Delta s^*(r)$ at r of the monolayer-separated minimum of $w(r)$ for LJ particles at $T = 300$ K. The particle diameter σ^* ranges from 1 to 3. (a) The results of a quadratic fit to $w^*(r)$ against T. Blue circles, red diamonds, and green squares represent $w^*(r)$, $\Delta h^*(r)$, and $-T\Delta s^*(r)$, respectively. (b) $w^*(r)$, $\Delta h^*(r)$, and $-T\Delta s^*(r)$ obtained from a linear fit to $w^*(r)$ against T. (c) The σ^* dependence of $\Delta h^*(r) = \Delta U_{\rm sw}(r) + \Delta U_{\rm ww}(r)$. Red, light-green, and light-blue bars represent $\Delta h^*(r)$, $\Delta U_{\rm sw}(r)$, and $\Delta U_{\rm ww}(r)$, respectively. Reproduced from "H. Naito, T. Sumi, and K. Koga, *J. Chem. Phys.*, Vol. 161, doi: 10.1063/5.0233808 (2024)", with the permission of AIP Publishing.

in water.[106] The increase of $w^*(r)$ at the monolayer-separated distance with σ^* is due to the enthalpic contribution $\Delta h^*(r)$ regardless of the fitting forms of $w^*(r)$: $\Delta h^*(r)$ positively ascends as σ^* increases.

Figure 3.10(c) displays the σ^* dependence of $\Delta h^*(r) = \Delta U_{\rm sw}(r)+\Delta U_{\rm ww}(r)$. The energy change $\Delta U_{\rm sw}(r)$ of the solute-water pair interaction increases with increasing particle size, indicating that "the desolvation cost" of water molecules increases with σ^*. Here, "the desolvation cost" is an energetic loss of the solute-water pair interaction energy when two solutes are close to each other, and parts of water molecules are removed from the solvation shells of the solutes (compare Figures 3.4(a) and (d)). The energy change $\Delta U_{\rm ww}(r)$ of the water-water pair interaction is negative for $\sigma^* = 1$, so the monolayer structure of water in the gap between methane-sized particles is energetically stable. In contrast, $\Delta U_{\rm ww}(r)$ is positive for $\sigma^* = 1.5$, 2, 2.5 and 3. We will analyze the structural stability/instability of the monolayer structure of water based on the spatial distributions of the number of hydrogen bonds between water molecules.

The thermodynamic factor determining the size dependence of the desolvation barrier is similar to that of the monolayer-separated minimum. Figures 3.11(a) and (b) indicate that in the σ^* range from 2 to 3, $\Delta h^*(r)$ is positive and increases with σ^*, while $-T\Delta s^*(r)$ is negative and decreases with σ^*. The magnitude of the enthalpic contribution is greater than that of the entropic contribution, so the resulting $w^*(r)$ at the desolvation barrier is positive and increases as the particle size increases. Figure 3.11(c) shows that both energy changes, $\Delta U_{\rm sw}(r)$ and $\Delta U_{\rm ww}(r)$, become larger as σ^* increases. The former size dependence implies an increase in the desolvation cost, and the latter would be related to the structural change of water around the solute pair.

Finally, we study the effect of particle size on the contact minimum. As shown in Figure 3.6, $w^*(r)$ at r of the contact minimum of $w(r)$ is negative and descends with increasing σ^*. Figures 3.12(a) and (b) displays that the decrement of $w^*(r)$ against σ^* is mainly due to the entropic contribution: $-T\Delta s^*(r)$ is negative and decreases as the particle size increases up to $\sigma^* = 2.5$. The entropic stabilization of the solute pair is due to the overlap of two excluded volumes of the solutes. See the detailed discussion for the

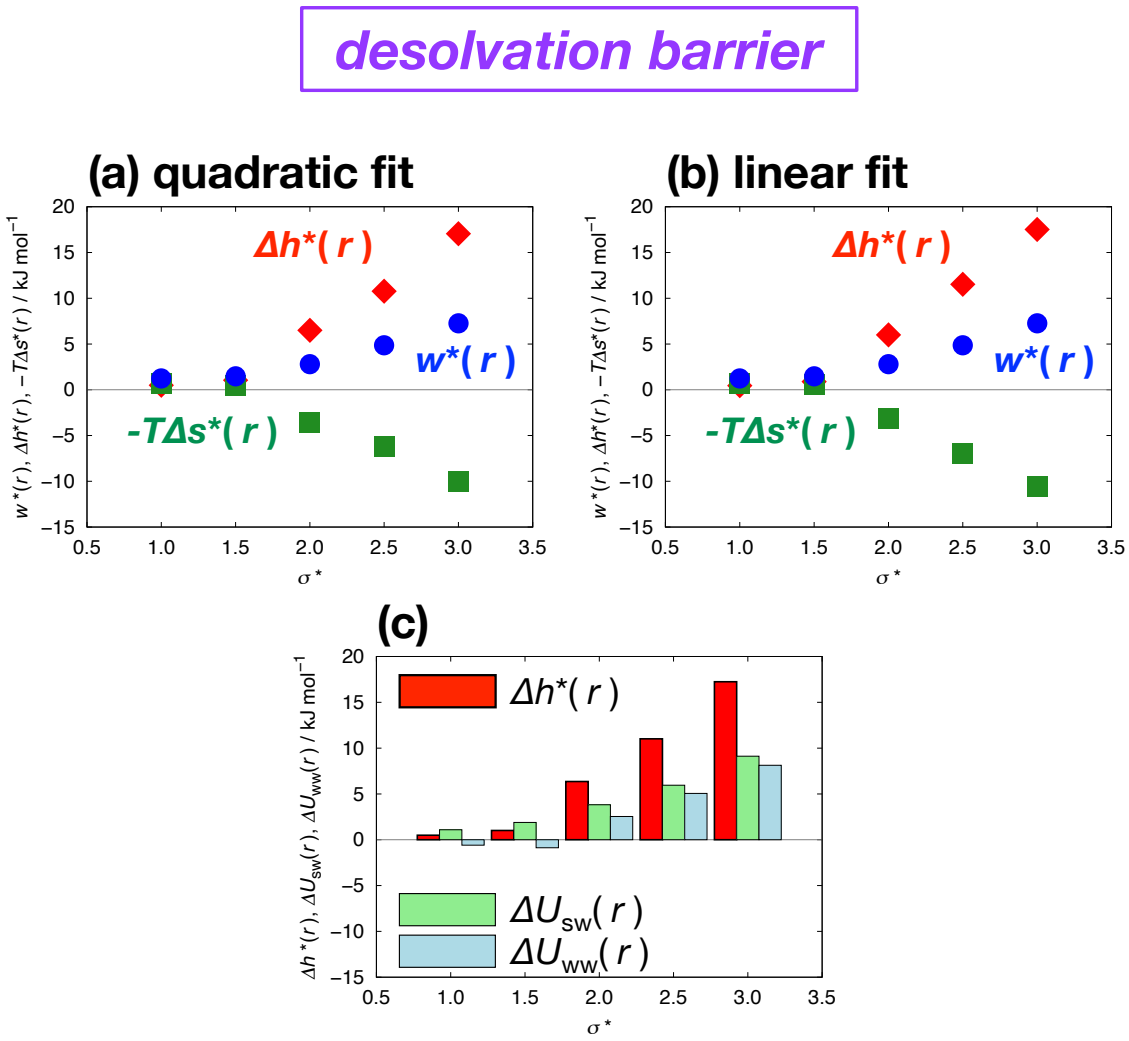

Figure 3.11: The particle size dependence of $w^*(r)$, $\Delta h^*(r)$, and $-T\Delta s^*(r)$ at r of the desolvation barrier of $w(r)$ for LJ particles at $T = 300$ K. The particle diameter σ^* ranges from 1 to 3. (a) The results of a quadratic fit to $w^*(r)$ against T. Blue circles, red diamonds, and green squares represent $w^*(r)$, $\Delta h^*(r)$, and $-T\Delta s^*(r)$, respectively. (b) $w^*(r)$, $\Delta h^*(r)$, and $-T\Delta s^*(r)$ obtained from a linear fit to $w^*(r)$ against T. (c) The σ^* dependence of $\Delta h^*(r) = \Delta U_{\rm sw}(r) + \Delta U_{\rm ww}(r)$. Red, light-green, and light-blue bars represent $\Delta h^*(r)$, $\Delta U_{\rm sw}(r)$, and $\Delta U_{\rm ww}(r)$, respectively. Reproduced from "H. Naito, T. Sumi, and K. Koga, *J. Chem. Phys.*, Vol. 161, doi: 10.1063/5.0233808 (2024)", with the permission of AIP Publishing.

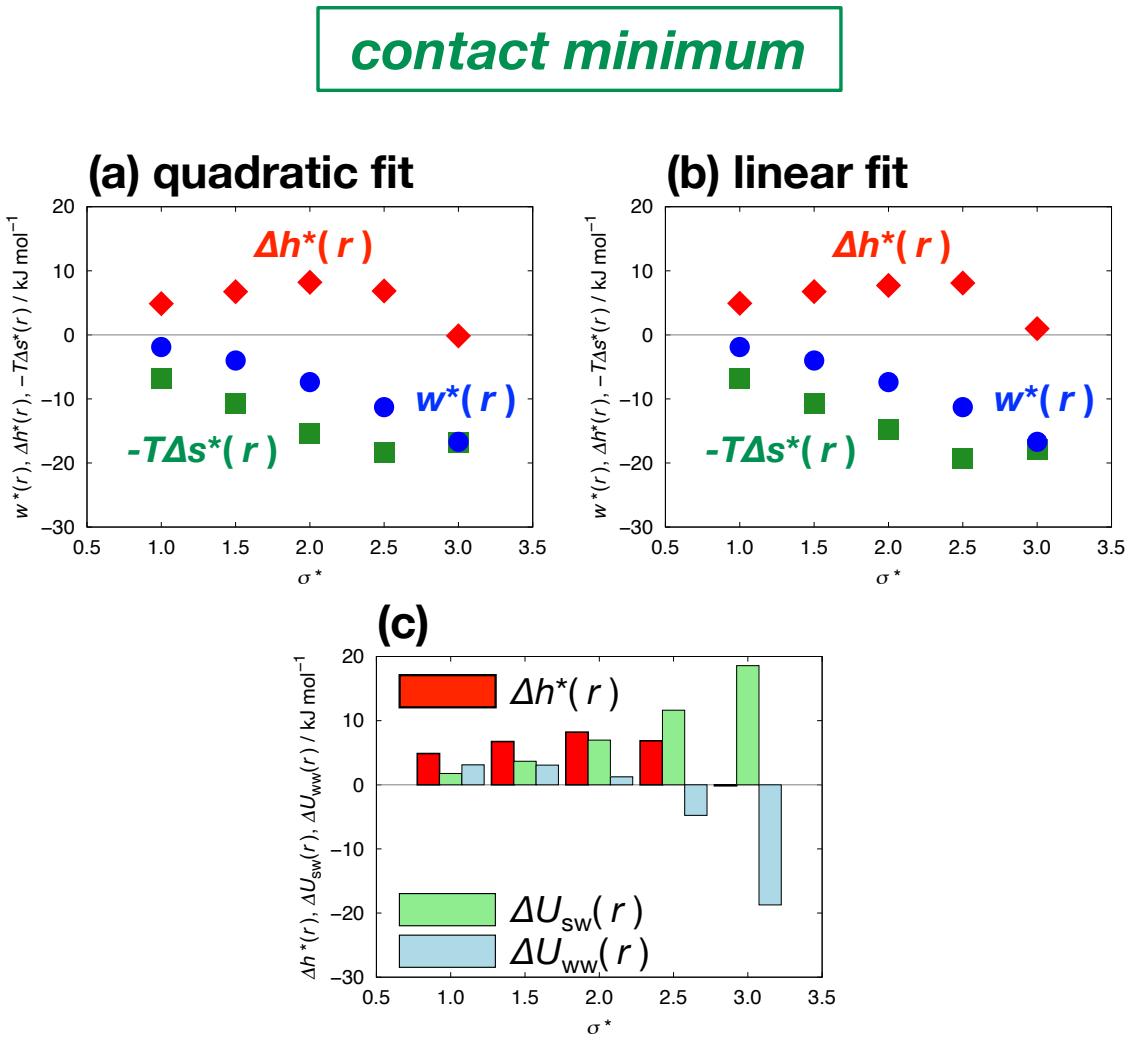

Figure 3.12: The particle size dependence of $w^*(r)$, $\Delta h^*(r)$, and $-T\Delta s^*(r)$ at r of the contact minimum of $w(r)$ for LJ particles at $T = 300$ K. The particle diameter σ^* ranges from 1 to 3. (a) The results of a quadratic fit to $w^*(r)$ against T. Blue circles, red diamonds, and green squares represent $w^*(r)$, $\Delta h^*(r)$, and $-T\Delta s^*(r)$, respectively. (b) $w^*(r)$, $\Delta h^*(r)$, and $-T\Delta s^*(r)$ obtained from a linear fit to $w^*(r)$ against T. (c) The σ^* dependence of $\Delta h^*(r) = \Delta U_{\rm sw}(r) + \Delta U_{\rm ww}(r)$. Red, light-green, and light-blue bars represent $\Delta h^*(r)$, $\Delta U_{\rm sw}(r)$, and $\Delta U_{\rm ww}(r)$, respectively. Reproduced from "H. Naito, T. Sumi, and K. Koga, *J. Chem. Phys.*, Vol. 161, doi: 10.1063/5.0233808 (2024)", with the permission of AIP Publishing.

excluded volume effect[12] in Chapters 2 and 4.

The enthalpic contribution $\Delta h^*(r)$ is positive for any size particles but has a non-monotonic dependence on σ^*: For the result obtained from a quadratic fit of $w^*(r)$, $\Delta h^*(r)$ increases with increasing σ^* from 1 to 2, while it decreases with σ^* from 2 to 3. In the case of the largest solute with $\sigma^* = 3$, $\Delta h^*(r)$ is close to zero.

Figure 3.12(c) shows $\Delta h^*(r)$, $\Delta U_{\rm sw}(r)$, and $\Delta U_{\rm ww}(r)$ at the contact minimum. Interestingly, $\Delta U_{\rm sw}(r)$ and $\Delta U_{\rm ww}(r)$ have opposite trends against the particle size: The change $\Delta U_{\rm sw}(r)$ of the solute-water pair interaction energy is positive and monotonically increases with increasing σ^*, indicating the increase of the desolvation cost with σ^*. In contrast, the change $\Delta U_{\rm ww}(r)$ of the water-water pair interaction energy is positive for $\sigma^* = 1$, 1.5, and 2, but its magnitude decreases with σ^*. $\Delta U_{\rm ww}(r)$ is significantly negative for $\sigma^* = 3$ and cancels out the largely positive $\Delta U_{\rm sw}(r)$, so the resulting $\Delta h^*(r) = \Delta U_{\rm sw}(r) + \Delta U_{\rm ww}(r)$ is close to zero. Therefore, the non-monotonic σ^* dependence of $\Delta h^*(r)$ at the contact distance is due to the opposite trends of $\Delta U_{\rm sw}(r)$ and $\Delta U_{\rm ww}(r)$ against σ^*.

We summarize in Table 3.2 the σ^* dependence of $w^*(r)$, $\Delta h^*(r)$, $-T\Delta s^*(r)$, $\Delta U_{\rm sw}(r)$, and $\Delta U_{\rm ww}(r)$ at r of the bilayer-separated minimum, the monolayer-separated minimum, the desolvation barrier, and the contact minimum. Here, we focus on the particle size effects on $\Delta U_{\rm ww}(r)$: At the bilayer-separated minimum and the contact minimum, $\Delta U_{\rm ww}(r)$ decreases with increasing σ^*, but at the monolayer-separated minimum and the desolvation barrier, $\Delta U_{\rm ww}(r)$ increases with σ^*. To clarify the microscopic factors determining the σ^* dependence of $\Delta U_{\rm ww}(r)$ at particular distances r, we calculate the number of hydrogen bonds between water molecules around the solute pair.

Distributions of the Number of Hydrogen Bonds between Water Molecules Around Solute Pairs

Figure 3.13 displays the spatial distributions $N_{\rm HB}(h, d)$ of the number of hydrogen bonds between water molecules around the solute pair with $\sigma^* = 1$ (left), 2 (middle), and 3 (right) at $T = 300$ K. These two-dimensional distributions are obtained based on the cylindrical coordinate system (see Figure 3.2). When two solutes are 3 nm apart [Figure 3.13(a)], the

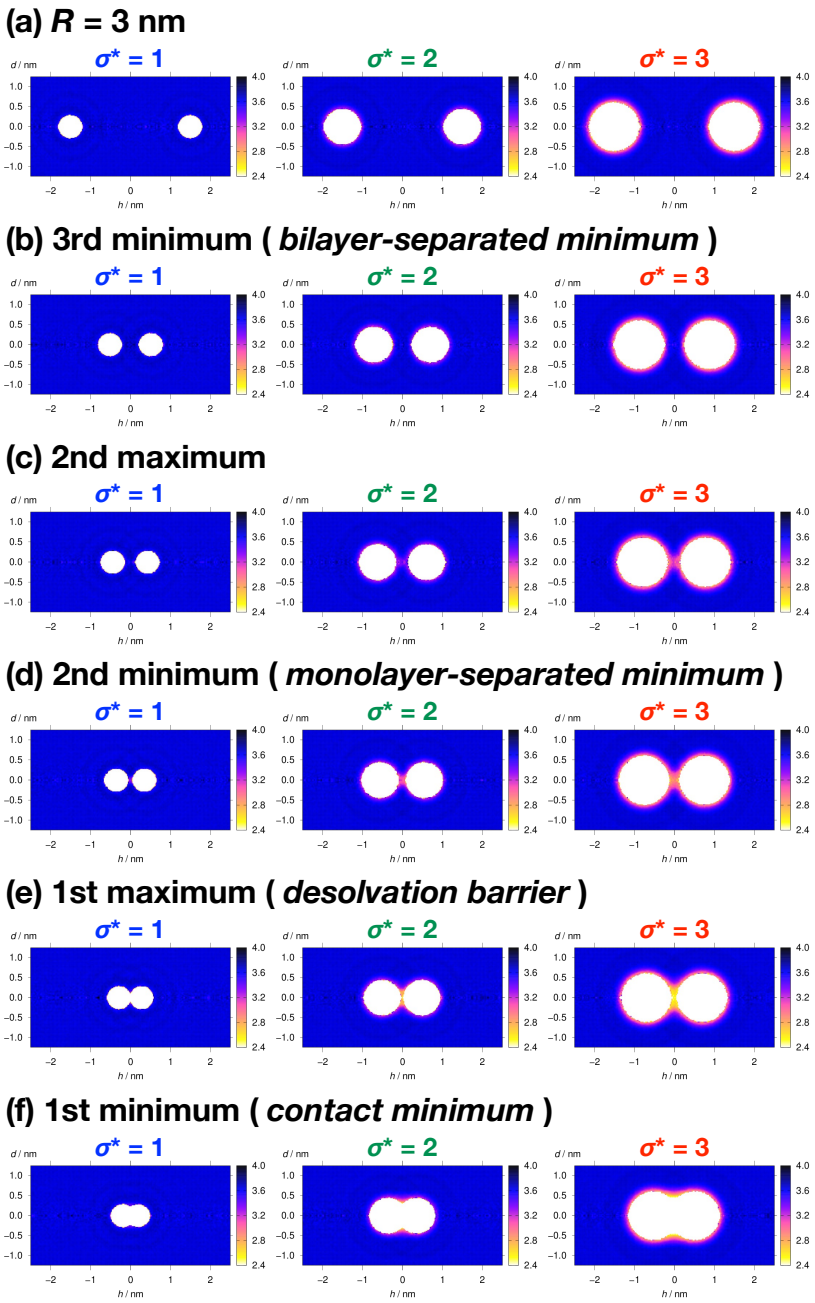

Figure 3.13: The spatial distributions $N_{\mathrm{HB}}(h, d)$ of the number of hydrogen bonds between water molecules per one molecule at $T = 300$ K. Two LJ particles with $\sigma^* = 1$ (left), 2 (middle), and 3 (right) are displayed in white. The solute-solute separation R is fixed to (a) 3 nm, or to r of (b) the third minimum (*bilayer-separated minimum*), (c) the second maximum, (d) the second minimum (*monolayer-separated minimum*), (e) the first maximum (*desolvation barrier*), and (f) the first minimum (*contact minimum*), of $w(r)$ for each-sized particle (see Table 3.1). N_{HB} of the bulk water is about 3.66. Reproduced from "H. Naito, T. Sumi, and K. Koga, *J. Chem. Phys.*, Vol. 161, doi: 10.1063/5.0233808 (2024)", with the permission of AIP Publishing.

Table 3.2: The particle size dependence of $w^*(r)$, $\Delta h^*(r)$, $-T\Delta s^*(r)$, $\Delta U_{\rm sw}(r)$, $\Delta U_{\rm ww}(r)$ for LJ particles in water at $T = 300$ K. The inter-particle distance is r of the bilayer-separated minimum, the monolayer-separated minimum, the desolvation barrier, and the contact minimum, of the solute-solute effective potential $w(r)$. The symbols $\nearrow$ and $\searrow$ denote the increment and decrement against σ^*, respectively, and $\longrightarrow$ represents little size dependence. The symbol $\nearrow\!\!\searrow$ for $\Delta h^*(r)$ at the contact minimum denotes the convex upward size dependence on σ^* (see Figure 3.12).

	$w^*(r)$	$\Delta h^*(r)$	$-T\Delta s^*(r)$	$\Delta U_{\rm sw}(r)$	$\boldsymbol{\Delta U_{\rm ww}(r)}$
bilayer-separated minimum	$\longrightarrow$	$\searrow$	$\nearrow$	$\nearrow$	$\searrow$
monolayer-separated minimum	$\nearrow$	$\nearrow$	$\searrow$	$\nearrow$	$\nearrow$
desolvation barrier	$\nearrow$	$\nearrow$	$\searrow$	$\nearrow$	$\nearrow$
contact minimum	$\searrow$	$\nearrow\!\!\searrow$	$\searrow$	$\nearrow$	$\searrow$

number $N_{\rm HB}(h, d)$ in the first solvation shell of the methane-sized particle is almost the same as $N_{\rm HB} \simeq 3.66$ in the bulk water. The number of hydrogen bonds in the solvation shell decreases as the particle size increases: $N_{\rm HB}(h, d)$ in the shell is approximately 3.4 and 3.0 for $\sigma^* = 2$ and 3, respectively.

Even though the inter-particle separation decreases from 3 nm to r of the bilayer-separated minimum of $w(r)$, the $N_{\rm HB}(h, d)$ in the gap between two particles is almost the same as in the bulk [Figure 3.13(b)]. The bilayer structure of water disappears at r of the second maximum of $w(r)$, and the $N_{\rm HB}(h, d)$ in the gap is smaller than that in the bulk due to the confinement of water molecules [Figure 3.13(c)]. The confinement effect is absent for the LJ particle with $\sigma^* = 1$ but notable for $\sigma^* = 3$.

When the particle-particle distance is r of the monolayer-separated minimum of $w(r)$, the effect of confinement on water becomes more obvious [Figure 3.13(d)]: $N_{\rm HB}(0, 0)$ at the midpoint of the solute pair is approximately 3.4 for $\sigma^* = 1$, 3.1 for $\sigma^* = 2$, and 3.0 for $\sigma^* = 3$. Therefore, water molecules in the monolayer structure are less hydrogen-bonded and thus less energetically stable than the bulk water. These unstable water molecules are the microscopic factor for the positive $\Delta U_{\rm ww}(r)$ at the monolayer-separated minimum for $\sigma^* = 2$ and 3 (see Figure 3.10(c)). Since the number $N_{\rm HB}(h, d)$ of hydrogen bonds in the gap between the large-size particles is close to 3, the monolayer structure of water

would be the planar hydrogen bond network.

As the inter-particle distance decreases to that of the desolvation barrier, $N_{\rm HB}(0,0)$ becomes smaller [Figure 3.13(e)]. At the contact minimum, $N_{\rm HB}(0,0)$ is zero because two solutes are in contact with each other [Figure 3.13(f)].

Now, we discuss the microscopic factor of the negative $\Delta U_{\rm ww}(r)$ at r of the contact minimum for the C_{60}-sized particle (see Figure 3.12(c)). The number $N_{\rm HB}(h,d)$ of hydrogen bonds in the first solvation shell of the LJ particle with $\sigma^* = 3$ is about 3, smaller than in the bulk ($N_{\rm HB} \simeq 3.66$). With decreasing the inter-particle distance r towards the contact distance, parts of the water molecules in the two shells are released into the bulk region. Then, the number of hydrogen bonds of these released water molecules increases to the bulk value. Therefore, the sum $U_{\rm ww}(r)$ of the pair interaction energy between water molecules decreases as r decreases from an infinite separation to the contact distance. Previous studies similarly suggested that the negative enthalpic contribution to the contact pair of actual C_{60} fullerenes[107] or hydrophobic plates[90] is due to the increment in the number of hydrogen bonds.

3.3.2 Weeks-Chandler-Andersen Solute

Now we consider the other type of the solute; the WCA solute. This solute interacts with water molecules via the repulsive part of the Weeks-Chandler-Andersen (WCA) potential.[54] The difference between two types of the solutes is that the pair potential between solute and water molecules includes the attractive part (LJ solute) or not (WCA solute).

Potentials of Mean Force

Figure 3.14 shows the potentials $w(r)$ of mean force for pairs of the LJ solutes (solid curves) and the WCA solutes (dashed curves) in water at $T = 300$ K. The contact minimum of $w(r)$ for the WCA solutes becomes deeper than that for the LJ solutes, consistent with the simulation result for the water-mediated interaction between C_{60} fullerenes.[72] This minimum also decreases as σ^* increases from 1 (methane size) to 3 (C_{60} size). The

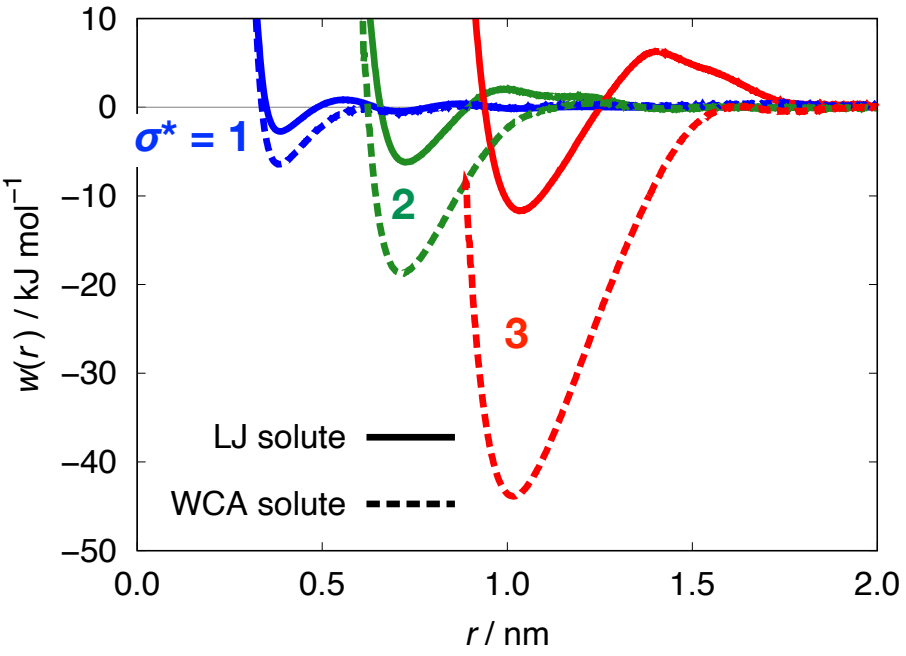

Figure 3.14: The effective potentials $w(r)$ for the LJ solutes and the Weeks-Chandler-Andersen (WCA) solutes in water at $T = 300$ K. The LJ and WCA solutes interact with water molecules through the LJ and repulsive WCA potentials,[54] respectively. The solute diameters σ^* are 1 (blue), 2 (green), and 3 (red). The solid and dashed curves represent $w(r)$ for the LJ and WCA solutes, respectively.

decrease of the contact minimum with σ^* is more drastic for the WCA solutes than for the LJ solutes: $w(r) = -2.73$, -6.22, and -11.69 kJ mol^{-1} for the LJ solutes with $\sigma^* = 1$, 2, and 3, respectively, while $w(r) = -6.43$, -18.73, and -43.88 kJ mol^{-1} for the WCA solutes with $\sigma^* = 1$, 2, and 3, respectively. One can see that $w(r)$ for the WCA solutes does not have the desolvation barrier and the monolayer-separated minimum.[72]

The rise in temperature affects the strength of the solute-solute effective interaction when the solute particles are repellent with water molecules. Figures 3.15(a)-(c) display $w(r)$ for the WCA solutes with $\sigma^* = 1$, 2, and 3 in water at three temperatures $T = 270$, 300, and 330 K. For each-size solute, the contact minimum decreases with increasing T. The effective potentials between the WCA solutes with $\sigma^* = 2$ and 3 do not have the monolayer-separated minimum, but at r of the monolayer-separated minimum for the LJ solutes, $w(r)$ decreases with T.

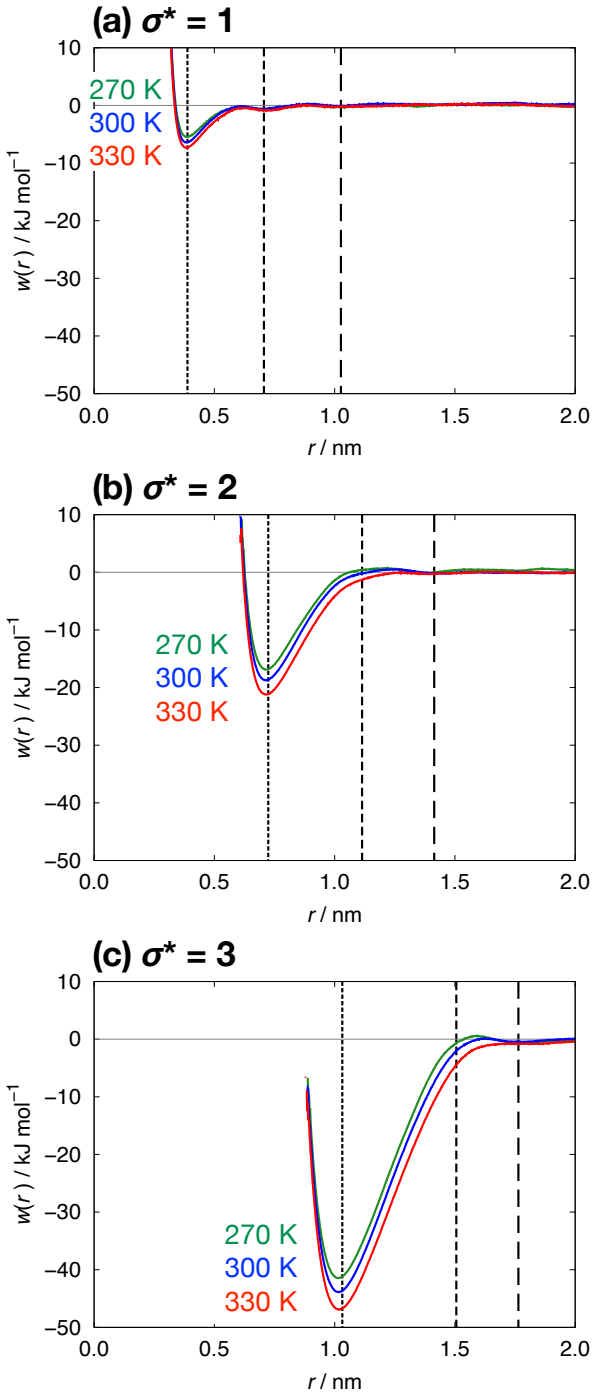

Figure 3.15: The effective potentials $w(r)$ for pairs of the WCA solutes of different sizes in water at three T. The solute diameters σ^* are (a) 1 (methane size), (b) 2, and (c) 3 (C_{60} fullerene size). Each curve shows the result at $T = 270$ K (green), 300 K (blue), and 330 K (red), respectively. Dotted, short-dashed, and long-dashed black lines indicate the inter-solute distances r of the contact minimum, the monolayer-separated minimum, and the bilayer-separated minimum of $w(r)$ for the LJ solutes (see Table 3.1).

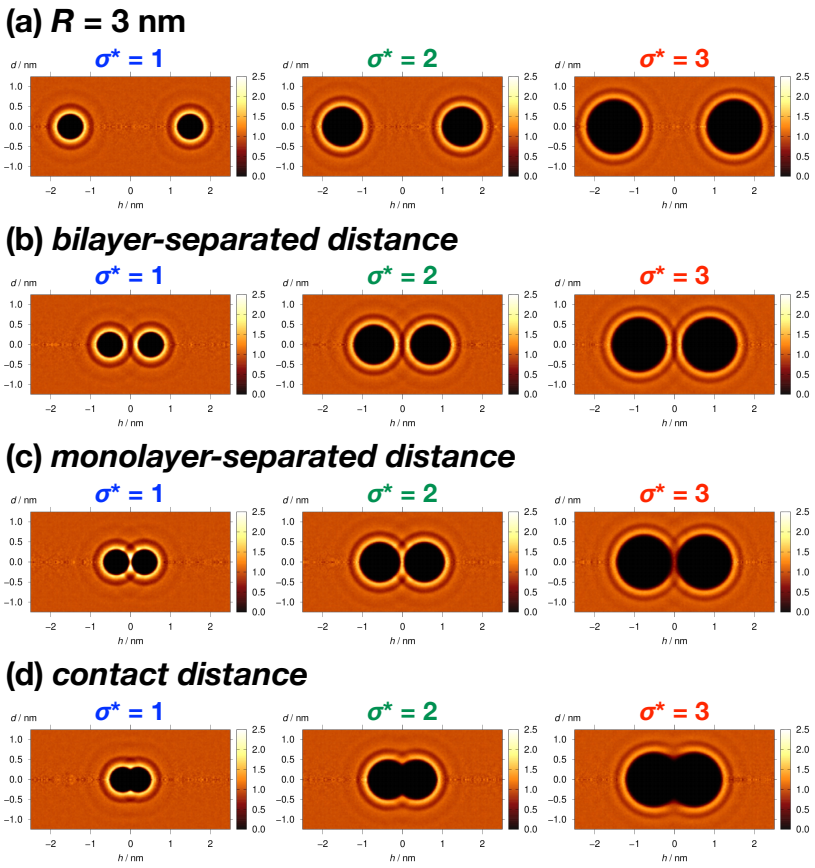

Figure 3.16: The normalized two-dimensional distributions $g_{\rm cyl}(h, d)$ of water molecules around a pair of the WCA solutes at $T = 300$ K. Two solutes with $\sigma^* = 1$ (left), 2 (middle), and 3 (right) are displayed in black. The solute-solute separation R is fixed to (a) 3 nm, or to r of (b) the bilayer-separated minimum, (c) the monolayer-separated minimum, and (d) the contact minimum, of $w(r)$ for the LJ solutes in water (see Table 3.1).

Distributions of Water Molecules Around Solute Pairs

Here, we study the water structure near a pair of the WCA solutes and compare the results with those for the LJ solutes. Figure 3.16 shows the normalized two-dimensional distributions $g_{\rm cyl}(h, d)$ of water molecules near the WCA solute pair with $\sigma^* = 1$ (left), 2 (middle), and 3 (right). When two solutes are 3 nm apart [Figure 3.16(a)], the local density of water in the first solvation shell of each solute is higher than the bulk density but slightly lower than that for the LJ solutes [Figure 3.4(a)]: For the WCA solutes, $g_{\rm cyl}(h, d)$ in the solvation shell is approximately 1.8, 1.6, and 1.4 for $\sigma^* = 1$, 2, and 3, respectively, while for the LJ solutes, it is nearly 2.0, 1.7, and 1.6 at $\sigma^* = 1$, 2, and 3.

As the solute-solute separation decreases from 3 nm to r of the bilayer-separated minimum of $w(r)$ for the LJ solutes (see Table 3.1), the bilayer structure of water appears in between the two WCA solutes [Figure 3.16(b)]. The height of these peaks is higher than $g_{\rm cyl}(h,d)$ in the other part of the solvation shells: $g_{\rm cyl}(h,d)$ is approximately 2.1, 1.9, and 1.5 for the WCA solutes with $\sigma^* = 1$, 2, and 3, respectively. These values are smaller than those for the LJ solute: The peak height of $g_{\rm cyl}(h,d)$ in the gap between the LJ solutes is approximately 2.3, 2.1, and 1.8 for $\sigma^* = 1$, 2, and 3, respectively [Figure 3.4(b)].

When the particle-particle distance is r of the monolayer-separated minimum of $w(r)$ for the LJ solutes, the bilayer structure disappears [Figure 3.16(c)]. For the WCA solutes with $\sigma^* = 1$ and 2, the water density inside the monolayer structure is higher than outside. However, that density for $\sigma^* = 3$ is lower than the bulk density: $g_{\rm cyl}(0,0)$ is approximately 2.0 for $\sigma^* = 1$ and 1.7 for $\sigma^* = 2$, but 0.7 for $\sigma^* = 3$. In the case of the LJ solute with $\sigma^* = 3$, $g_{\rm cyl}(h,d)$ inside the gap between two solute particles is slightly greater than outside the gap [Figure 3.4(d)]. With decreasing the inter-solute distance to r of the contact minimum of $w(r)$ for the LJ solutes, two WCA solutes are in contact with each other [Figure 3.16(d)].

Enthalpic and Entropic Contributions to the Water-Mediated Potentials

Now, the solute size effects on the water-mediated interaction between the WCA solutes are examined. Figure 3.17 shows $w^*(r) = w(r) - \phi(r)$ for pairs of the WCA solutes with $\sigma^* = 1$, 2, and 3 together with the direct part $\phi(r)$. The water-mediated potential $w^*(r)$ for the LJ solutes has a positive potential peak corresponding to the desolvation barrier (see Figure 3.5), whereas $w^*(r)$ for the WCA solutes does not have such a peak.[72] The following analysis investigates why the potential barrier disappears when the solute particle is repellent with water molecules.

The enthalpy and entropy changes are obtained from a temperature derivative of a linear fit to $w^*(r)$ against T. Figures 3.18(a) and (b) display $\Delta h^*(r)$ and $-T\Delta s^*(r)$, respectively, for pairs of the WCA solutes. In contrast to the water-mediated potential, $\Delta h^*(r)$ and $-T\Delta s^*(r)$ oscillate depending on the solute-solute distance r. Here, we

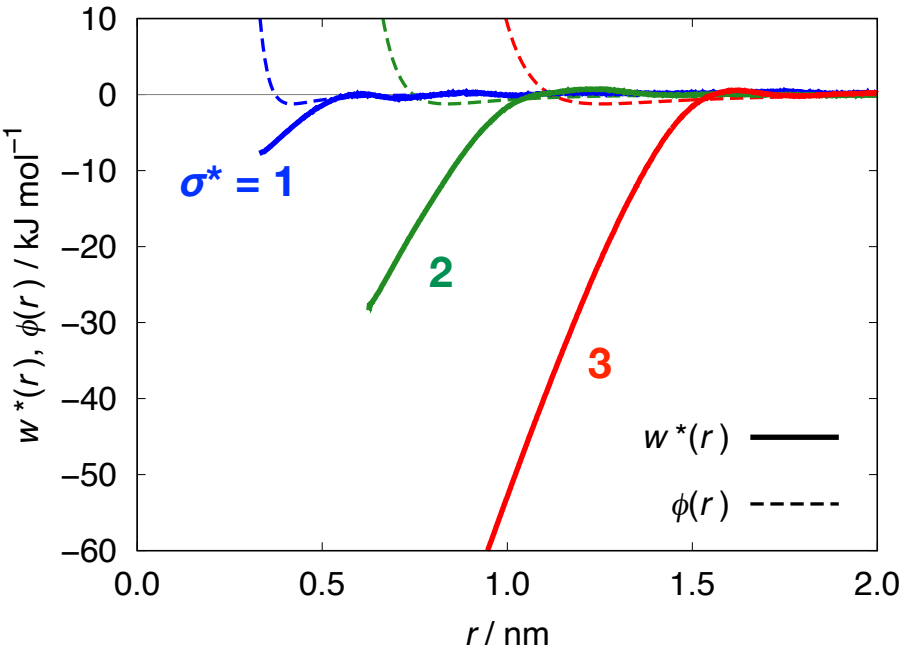

Figure 3.17: The water-mediated potentials $w^*(r)$ for the WCA solutes with $\sigma^* = 1$, 2, and 3 at $T = 300$ K. The excess parts $w^*(r)$ of the effective potentials $w(r)$ and the direct parts $\phi(r)$ are represented by the solid and dashed curves, respectively.

focus on $w^*(r)$, $\Delta h^*(r)$, and $-T\Delta s^*(r)$ at the bilayer-separated, monolayer-separated, and contact distances of $w(r)$ for the LJ solutes. The values of these distances are listed in Table 3.1 and highlighted in Figure 3.15.

Solute Size Dependence of $w^*(r) = \Delta h^*(r) - T\Delta s^*(r)$

Figure 3.19(a) shows the σ^* dependence of $w^*(r) = \Delta h^*(r) - T\Delta s^*(r)$ for the WCA solutes at the bilayer-separated distance. The water-mediated potential $w^*(r)$ is close to zero for any size solutes. In contrast to the result for the LJ solutes, $\Delta h^*(r)$ and $-T\Delta s^*(r)$ for the WCA solutes hardly depend on σ^*. The enthalpy change $\Delta h^*(r)$ is slightly negative for $\sigma^* = 1$ and 3, while it takes a small positive value when $\sigma^* = 2$. Figure 3.19(b) indicates that the magnitudes of $\Delta h^*(r)$ are determined by the change $\Delta U_{\mathrm{ww}}(r)$ of the water-water pair interaction energy because the change $\Delta U_{\mathrm{sw}}(r)$ of the solute-water pair interaction energy is almost zero for all solutes.

Next, Figure 3.20(a) shows the σ^* dependence of $w^*(r)$, $\Delta h^*(r)$, and $-T\Delta s^*(r)$ at the monolayer-separated distance. For $\sigma^* = 1$, $\Delta h^*(r)$ is slightly negative (-0.80 kJ mol^{-1})

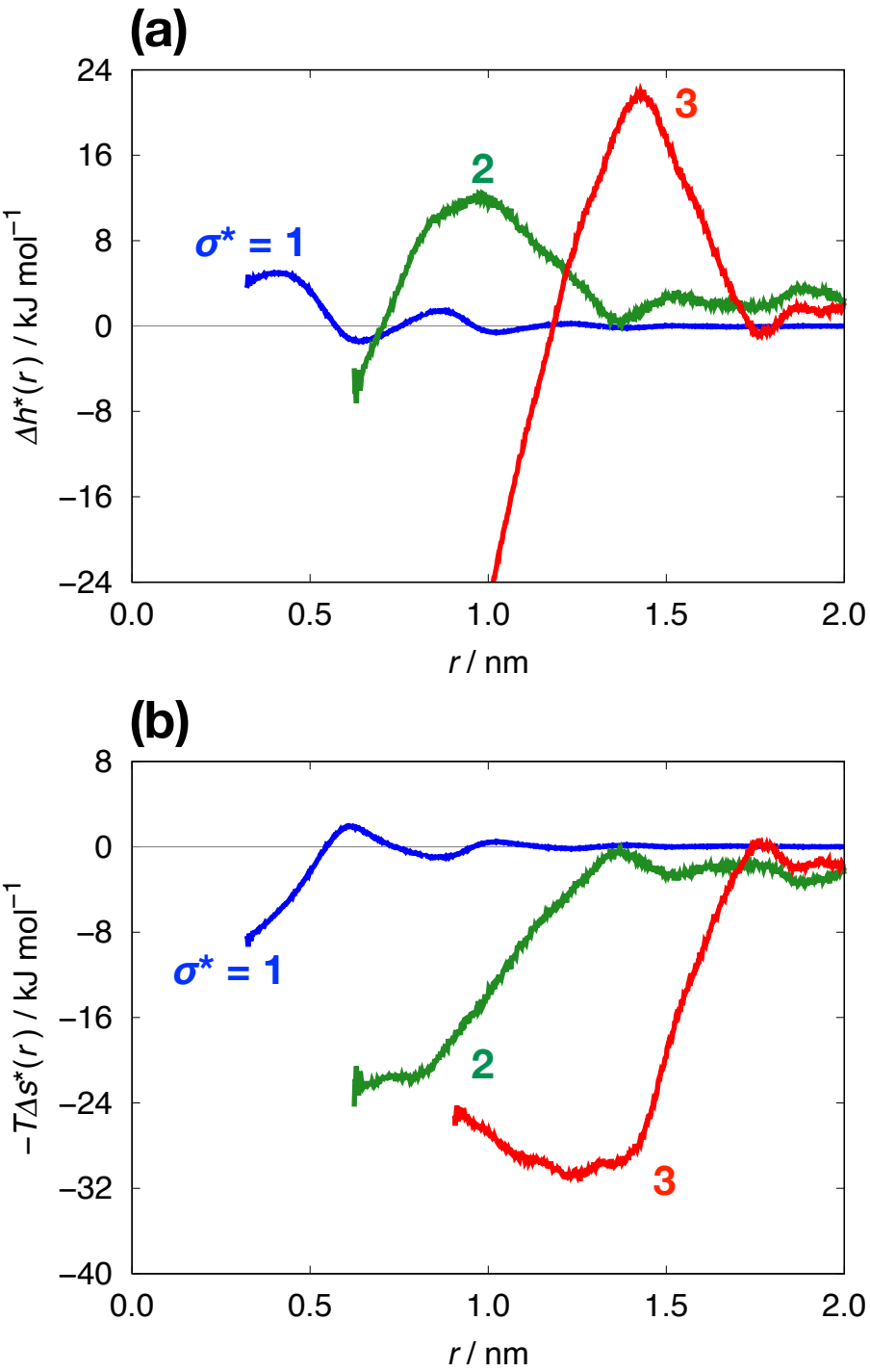

Figure 3.18: The enthalpic and entropic contributions, $\Delta h^*(r)$ and $-T\Delta s^*(r)$, to the water-mediated potentials $w^*(r)$ for the WCA solutes at $T = 300$ K. The solute diameter σ^* is 1, 2, and 3. (a) $\Delta h^*(r)$ and (b) $-T\Delta s^*(r)$ are obtained from a linear fit to $w^*(r)$ as a function of T.

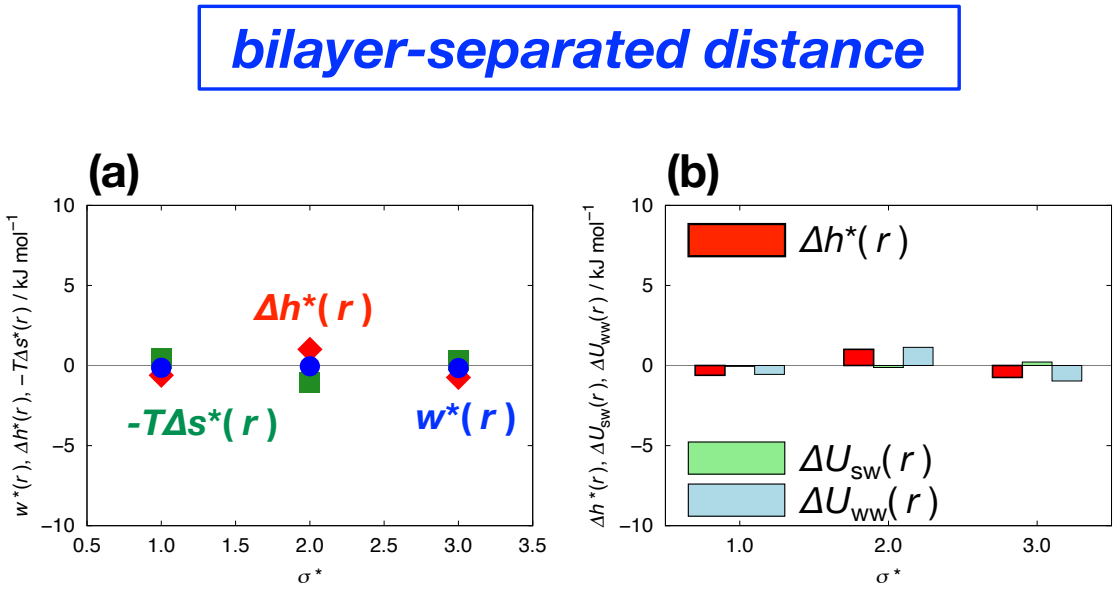

Figure 3.19: (a) The solute size dependence of $w^*(r) = \Delta h^*(r) - T\Delta s^*(r)$ for pairs of the WCA solutes in water at $T = 300$ K. The inter-solute distances are r of the bilayer-separated minimum of $w(r)$ for the LJ solutes (see Table 3.1). The particle diameter σ^* varies from 1 to 3. The linear fit to $w^*(r)$ (blue circle) against T gives $\Delta h^*(r)$ (red diamond) and $-T\Delta s^*(r)$ (green square). (b) The σ^* dependence of $\Delta h^*(r) = \Delta U_{\rm sw}(r) + \Delta U_{\rm ww}(r)$, where $\Delta U_{\rm sw}(r)$ and $\Delta U_{\rm ww}(r)$ are the changes in the sums of the solute-water and water-water pair interaction energies, respectively, as the solute-solute distance decreases from infinity to r. Red, light-green, and light-blue bars represent $\Delta h^*(r)$, $\Delta U_{\rm sw}(r)$, and $\Delta U_{\rm ww}(r)$, respectively.

while $-T\Delta s^*(r)$ is slightly positive ($+0.44$ kJ mol^{-1}) so that $w^*(r) = \Delta h^*(r) - T\Delta s^*(r)$ is nearly zero (-0.36 kJ mol^{-1}). $w^*(r)$ for $\sigma^* = 2$ and 3 is also close to zero, so the water-mediated interaction hardly depends on the solute size. However, the magnitudes of $\Delta h^*(r)$ and $-T\Delta s^*(r)$ for $\sigma^* = 2$ and 3 are large, and they show the opposite trends against σ^*: The enthalpic contribution to $w^*(r)$ is positive and increases with increasing σ^*, while the entropic contribution is negative and decreases with σ^*. The magnitudes of both contributions are nearly equal, so the positive $\Delta h^*(r)$ and the negative $-T\Delta s^*(r)$ mostly cancel each other out.

We divide $\Delta h^*(r)$ into two parts, $\Delta U_{\rm sw}(r)$ and $\Delta U_{\rm ww}(r)$. Figure 3.20(b) is a plot of $\Delta h^*(r)$, $\Delta U_{\rm sw}(r)$, and $\Delta U_{\rm ww}(r)$ as a function of σ^*. $\Delta U_{\rm sw}(r)$ is close to zero for the WCA solutes with $\sigma^* = 1$ and 2, and it is negative for $\sigma^* = 3$. The sign of $\Delta U_{\rm sw}(r)$

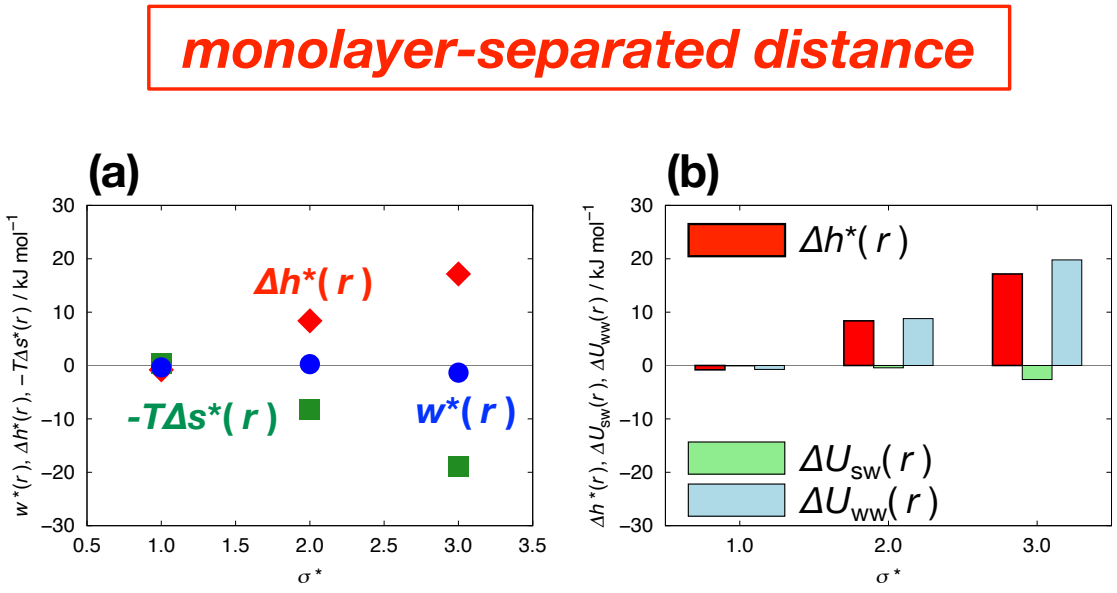

Figure 3.20: (a) The solute size dependence of $w^*(r) = \Delta h^*(r) - T\Delta s^*(r)$ for pairs of the WCA solutes in water at $T = 300$ K. The inter-solute distances are r of the monolayer-separated minimum of $w(r)$ for the LJ solutes (see Table 3.1). The particle diameter σ^* varies from 1 to 3. The linear fit to $w^*(r)$ (blue circle) against T gives $\Delta h^*(r)$ (red diamond) and $-T\Delta s^*(r)$ (green square). (b) The σ^* dependence of $\Delta h^*(r) = \Delta U_{\rm sw}(r) + \Delta U_{\rm ww}(r)$. Red, light-green, and light-blue bars represent $\Delta h^*(r)$, $\Delta U_{\rm sw}(r)$, and $\Delta U_{\rm ww}(r)$, respectively.

and its σ^* dependence are completely different from those for the LJ solutes: $\Delta U_{\rm sw}(r)$ at the monolayer-separated minimum increases with increasing the size of the LJ solute (see Figure 3.10(c)), indicating that the desolvation cost of water molecules increases with σ^*. In the case of the WCA solute with $\sigma^* = 3$, removing parts of water molecules from the solvation shell is not an energetic loss but rather an energetic gain.

The energy change $\Delta U_{\rm ww}(r)$ of the water-water pair interaction is slightly negative for $\sigma^* = 1$. On the other hand, $\Delta U_{\rm ww}(r)$ is positive for $\sigma^* = 2$, and its magnitude ascends with increasing σ^*. The positive $\Delta U_{\rm ww}(r)$ for large WCA solutes suggests that the monolayer structure of water in between two solutes is energetically unstable, similar to the LJ solutes with $\sigma^* = 2$ and 3 (see Figure 3.10(c)).

Finally, we see the size effect on the contact minimum for the WCA solutes. Figure 3.21(a) displays that the water-mediated potential $w^*(r)$ at the contact distance is

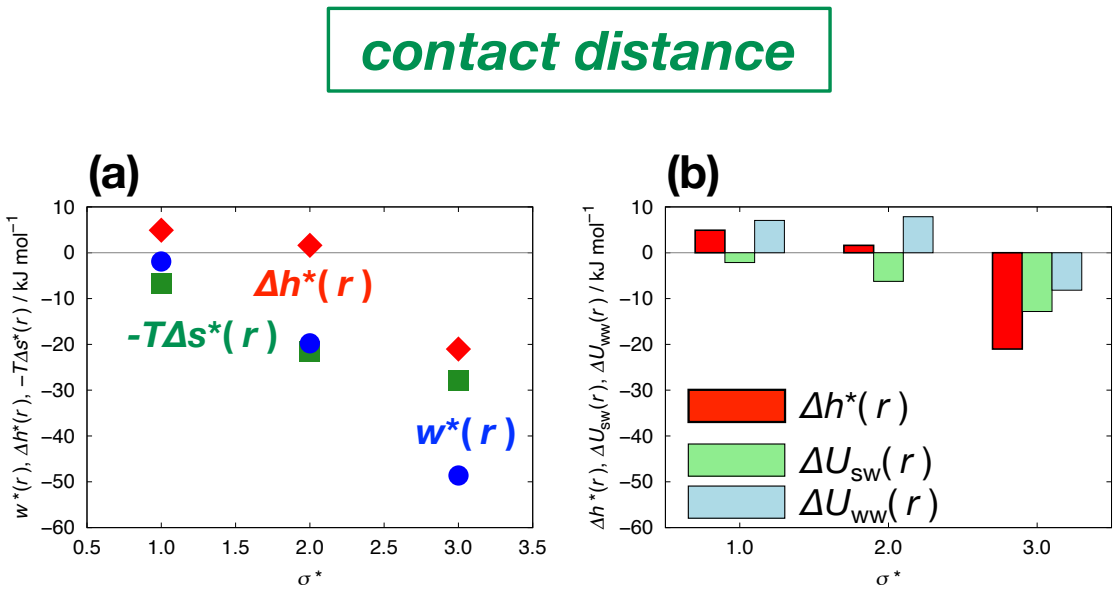

Figure 3.21: (a) The solute size dependence of $w^*(r) = \Delta h^*(r) - T\Delta s^*(r)$ for pairs of the WCA solutes in water at $T = 300$ K. The inter-solute distances are r of the contact minimum of $w(r)$ for the LJ solutes (see Table 3.1). The particle diameter σ^* varies from 1 to 3. The linear fit to $w^*(r)$ (blue circle) against T gives $\Delta h^*(r)$ (red diamond) and $-T\Delta s^*(r)$ (green square). (b) The σ^* dependence of $\Delta h^*(r) = \Delta U_{\rm sw}(r) + \Delta U_{\rm ww}(r)$. Red, light-green, and light-blue bars represent $\Delta h^*(r)$, $\Delta U_{\rm sw}(r)$, and $\Delta U_{\rm ww}(r)$, respectively.

negative and descends with increasing σ^*. It is clear that both the enthalpic and entropic contributions to $w^*(r)$ decrease as the solute size increases: The enthalpic contribution $\Delta h^*(r)$ is positive for $\sigma^* = 1$, close to zero for $\sigma^* = 2$, and negative for $\sigma^* = 3$. The entropic contribution $-T\Delta s^*(r)$ is negative for all-size solutes, and its magnitude increases with σ^* due to the increment of the excluded volume effect.[12]

Figure 3.21(b) shows $\Delta h^*(r)$, $\Delta U_{\rm sw}(r)$, and $\Delta U_{\rm ww}(r)$ at the contact distance as a function of σ^*. The change $\Delta U_{\rm sw}(r)$ of the solute-water pair potential energy in decreasing the distance between two WCA solutes from an infinite separation to the contact distance is negative and monotonically decreases with increasing σ^*. In contrast to the LJ solutes, the desolvation of water molecules is energetically favorable because the WCA solutes repel water molecules.

The change $\Delta U_{\rm ww}(r)$ of the water-water pair potential energy is positive for $\sigma^* = 1$ and 2, but it takes a negative value when $\sigma^* = 3$. In the case of the largest size solute, both

$\Delta U_{\rm sw}(r)$ and $\Delta U_{\rm ww}(r)$ are negative, and so the resulting $\Delta h^*(r) = \Delta U_{\rm sw}(r) + \Delta U_{\rm ww}(r)$ becomes significantly negative. Therefore, a deep minimum in $w(r)$ for the WCA solute with $\sigma^* = 3$, compared to $w(r)$ for the LJ solute (see Fig. 3.14), is due to the largely negative contributions from both the enthalpic and entropic terms.

Distributions of the Number of Hydrogen Bonds between Water Molecules Around Solute Pairs

The positive/negative $\Delta U_{\rm ww}(r)$ suggests the instability/stability of the microscopic structure of water. Here, we calculate the number of hydrogen bonds between water molecules around a pair of the WCA solutes. Figure 3.22 displays the spatial distributions $N_{\rm HB}(h, d)$ of the number of hydrogen bonds between water molecules near the WCA solute pair. When two solutes are 3 nm apart [Figure 3.22(a)], the number $N_{\rm HB}(h, d)$ in the first solvation shell of the WCA solute with $\sigma^* = 1$ is almost the same as $N_{\rm HB} \simeq 3.66$ for the bulk water. The number of hydrogen bonds in the solvation shell decreases as σ^* increases: $N_{\rm HB}(h, d)$ is approximately 3.5 for $\sigma^* = 2$ and 3.4 for $\sigma^* = 3$. These values are slightly larger than $N_{\rm HB}(h, d)$ for the LJ solutes: $N_{\rm HB}(h, d)$ in the shell is approximately 3.4 and 3.0 for the LJ solutes of $\sigma^* = 2$ and 3, respectively.

At the bilayer-separated distance, the $N_{\rm HB}(h, d)$ in the gap between two WCA solutes is slightly smaller than the bulk value [Figure 3.22(b)], so the confinement of water molecules has a bit of influence on the stability of the bilayer structure of water. The confinement effect becomes obvious when the inter-solute separation is the monolayer-separated distance [Figure 3.22(c)]: $N_{\rm HB}(0, 0)$ at the midpoint of the solute pair is approximately 3.3, 3.0, and 2.7 for $\sigma^* = 1$, 2, and 3, respectively. Similar to the result for the LJ solutes [Figure 3.13(d)], water molecules in the monolayer structure are energetically less stable than the bulk water. These molecules are the microscopic factor for the positive $\Delta U_{\rm ww}(r)$ at the monolayer-separated distance (see Figure 3.20(b)).

As the inter-solute separation decreases to the contact distance, two WCA solutes are in contact [Figure 3.22(d)]. The negative $\Delta U_{\rm ww}(r)$ for $\sigma^* = 3$ at the contact distance (see Figure 3.21(b)) is due to releasing parts of water molecules from the solvation shells of

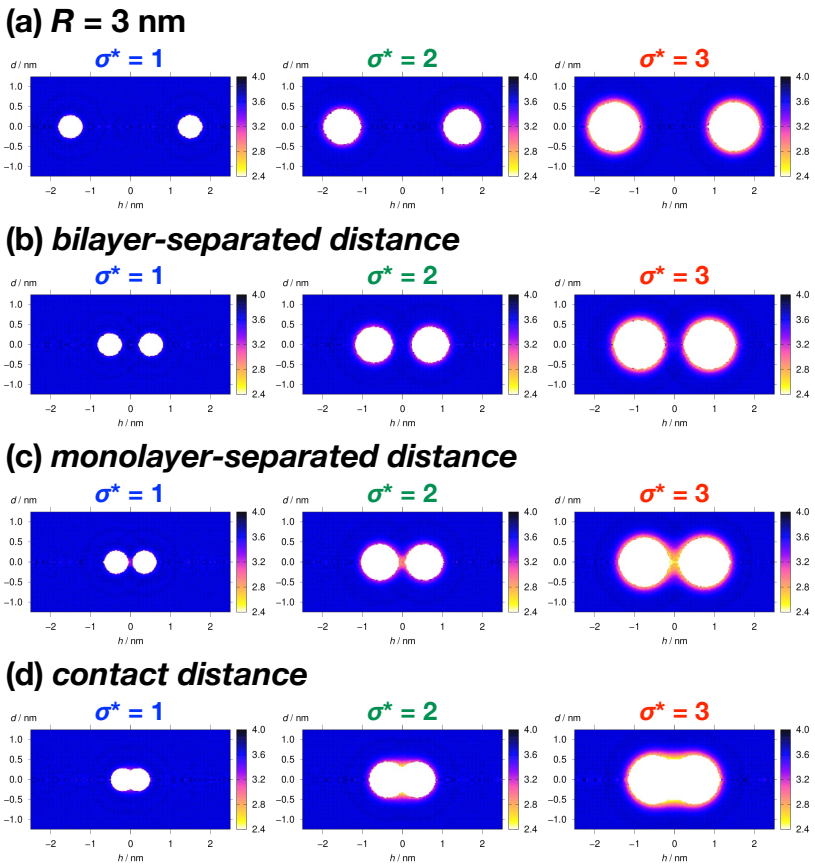

Figure 3.22: The spatial distributions $N_{\mathrm{HB}}(h, d)$ of the number of hydrogen bonds between water molecules per one molecule around a pair of the WCA solutes of different sizes at $T = 300$ K. Two solutes with $\sigma^* = 1$ (left), 2 (middle), and 3 (right) are displayed in white. The solute-solute separation R is fixed to (a) 3 nm, or to r of (b) the bilayer-separated minimum, (c) the monolayer-separated minimum, and (d) the contact minimum, of $w(r)$ for the LJ solutes in water (see Table 3.1).

the solutes into the bulk region when two solutes approach each other: The number of hydrogen bonds of these released water molecules increases from about 3.4 in the solvation shell to the bulk value $N_{\mathrm{HB}} \simeq 3.66$.

3.4 CONCLUSIONS

Energetic and structural analyses elucidated the thermodynamic and microscopic factors determining the particle size dependence of the water-mediated interactions. The nature of the inter-solute effective interaction in water varies as the particle size increases from

methane's to C_{60} fullerene's size. The presence or absence of the solute-water attraction also changes the strength of the effective interaction and its driving force.

Based on the molecular dynamics simulation, we computed the potentials $w(r)$ of mean force for pairs of solute particles with different diameters σ^*. $w(r)$ oscillates depending on the solute-solute distance r and has minima and maxima at particular values of r. Three minima and one maximum of $w(r)$ were characterized by the structural analysis of calculating the spatial distributions of water molecules around the solute pair: We refer to the first minimum as the *contact minimum*, the second minimum as the *monolayer-separated minimum*, the third minimum as the *bilayer-separated minimum*, and the first maximum as the *desolvation barrier*. We quantified the enthalpic and entropic contributions to $w(r)$ at specific distances r to investigate the thermodynamic factors that determine the σ^* dependencies of the bilayer-separated minimum, the monolayer-separated minimum, the desolvation barrier, and the contact minimum.

When the inter-solute separation is r of the bilayer-separated minimum, two solutes are separated by the bilayer structure of water. The magnitude of the bilayer-separated minimum does not vary as the solute size increases due to the large canceling between the enthalpic and entropic contributions, $\Delta h^*(r)$ and $-T\Delta s^*(r)$: $\Delta h^*(r)$ is negative and decreases with increasing σ^*, while $-T\Delta s^*(r)$ is positive and increases with σ^*. The negative $\Delta h^*(r)$ is due to the negative change $\Delta U_{\mathrm{ww}}(r)$ of the water-water pair potential energy, suggesting that the bilayer structure of water is energetically stable. This result is in agreement with the previous simulation study of the effective potential between graphene plates[104]–[106] and C_{60} fullerenes[86] in water.

The monolayer structure of water is in the gap between two solutes at the monolayer-separated distance. In the case of the LJ solutes, the monolayer-separated minimum ascends with increasing σ^* due to the increment of the enthalpic contribution: $\Delta h^*(r)$ is negative for the methane-sized solute ($\sigma^* = 1$), but it becomes positive as the solute size increases to that of C_{60} ($\sigma^* = 3$). Two energy changes, $\Delta U_{\mathrm{ww}}(r)$ and $\Delta U_{\mathrm{sw}}(r)$, determine whether the monolayer-separated pair is enthalpically stable or unstable. The $\Delta U_{\mathrm{ww}}(r)$ is negative for $\sigma^* = 1$, so the monolayer-separated pair of the methane-sized

particle is stable. The structural analysis based on the spatial distribution of the number of hydrogen bonds between water molecules clarifies that methane-sized particles hardly disturb the solvation structure. In contrast, $\Delta U_{\mathrm{ww}}(r)$ is positive for the C_{60}-size solute, indicating that the monolayer-separated pair of large particles destabilizes the monolayer structure of water. The number of hydrogen bonds in the gap between two solute particles is actually smaller than the bulk value.

Another contribution determining the σ^* dependence of $\Delta h^*(r)$ is the change of the solute-water interaction energy: $\Delta U_{\mathrm{sw}}(r)$ is close to zero for $\sigma^* = 1$ but positively increases as the solute size increases. For the LJ solutes, $\Delta U_{\mathrm{sw}}(r)$ is positive because the number of water molecules in the first solvation shells is smaller when two solutes are monolayer-separated than when they are far apart. The increase of $\Delta U_{\mathrm{sw}}(r)$ with σ^* is due to the larger decrease in the number of water molecules in the solvation shells, i.e., the increment of the desolvation cost. The driving factors for the increase of the desolvation barrier with increasing σ^* are the same as those of the monolayer-separated minimum.

In the case of the WCA solutes, the repellent solute with water molecules, the trend of $\Delta U_{\mathrm{sw}}(r)$ vs. σ^* is completely different from that for the LJ solutes: At the monolayer-separated distance, $\Delta U_{\mathrm{sw}}(r)$ is negative and decreases with increasing σ^*. The negative $\Delta U_{\mathrm{sw}}(r)$ means that the decrement in the number of water molecules in the solvation shells of the WCA solutes is energetically favorable. $\Delta U_{\mathrm{ww}}(r)$ positively increases with σ^*, but the effective potential $w(r)$ at the monolayer-separated distance hardly depends on the solute size because the enthalpic term $\Delta h^*(r) > 0$ is canceled out by the entropic term $-T\Delta s^*(r) < 0$ for each solute.

Finally, the contact minimum of $w(r)$ is negative and decreases with increasing σ^*. Decreasing the inter-solute separation into the contact distance is mainly entropy-driven due to the excluded volume effect.[12] The enthalpy changes $\Delta h^*(r) = \Delta U_{\mathrm{sw}}(r) + \Delta U_{\mathrm{ww}}(r)$ in the contact configurations have different size dependence for the LJ and WCA solutes. The $\Delta U_{\mathrm{sw}}(r)$ for the LJ solutes is positive, and its magnitude increases with increasing σ^*. This size dependence is due to the increment of the desolvation cost, similar to $\Delta U_{\mathrm{sw}}(r)$ at the monolayer-separated minimum. In contrast, $\Delta U_{\mathrm{ww}}(r)$ decreases as the solute size

increases. The increase of $\Delta U_{\rm sw}(r)$ and the decrease of $\Delta U_{\rm ww}(r)$ give the non-monotonic σ^* dependence of the resulting $\Delta h^*(r)$ for the LJ solutes. The $\Delta U_{\rm ww}(r)$ for the largest solute is negative because the number of hydrogen bonds between water molecules in the first solvation shell of the single solute is small compared to the bulk water and because parts of the water molecules in the shells of two solutes are released into the bulk as the inter-solute separation decreases from infinity to the contact distance.

In the case of the WCA solutes, the change $\Delta U_{\rm sw}(r)$ of the solute-water pair interaction energy is negative, indicating that the desolvation of water molecules is an energetic gain. The magnitude of $\Delta U_{\rm sw}(r)$ increases with increasing σ^* because the number of water molecules released from the first solvation shells of the WCA solutes increases as the solute size increases. $\Delta U_{\rm sw}(r)$ and $\Delta U_{\rm ww}(r)$ are both negative for $\sigma^* = 3$, so the resulting enthalpy change becomes largely negative. The contact minimum is thus significantly negative due to the negative contributions from the enthalpic and entropic terms. The main difference between the LJ and WCA solutes is that the desolvation of water molecules is an energetic loss for the LJ solute but an energetic gain for the WCA solute.

Note that in the case of the LJ solutes, the magnitudes of the solute-solute and solute-water pair interactions, ϵ and $\epsilon_{\rm sw}$, are the same as those of the methane-methane and methane-water pair ones, respectively. The purpose of fixing ϵ and $\epsilon_{\rm sw}$ is to focus only on the size effect on the water-mediated interaction. In reality, however, the attractive (or dispersion) force between solute and water molecules becomes stronger for larger-size solutes. The strong solute-water attraction changes the nature of the inter-solute effective interaction and its size dependence qualitatively. For example, the effective potential $w(r)$ for pairs of the realistic C_{60} fullerenes in water has a negative value at the monolayer-separated distance,[5], [72], [86] in contrast to the result for the C_{60}-sized LJ particle. Moreover, the contact minimum positively increases with σ^* when the depth of the solute-water pair potential is significantly deeper than that of the methane-water LJ potential.[65] For a more detailed understanding of the water-mediated interaction, we should elucidate the driving factors for the size effect on the effective interaction that varies with the strength of the solute-water attraction.

Chapter 4

Integral Equation Study of the Particle Size Dependence of the Osmotic Second Virial Coefficient

Abstract

The present work investigates the quantitative relationship between the strength of the solute-solute effecive interaction and the solute size. Based on the integral equation theory, we calculate the potentials $w(r)$ of mean force and the osmotic second virial coefficients B for hard-sphere particles of different diameters σ in a hard-sphere solvent with its particle diameter σ_{v}. The numerical result shows that the contact minimum $w(\sigma)$ is negative and decreases with increasing σ. The descent of the contact minimum indicates that the contact pair of solute particles becomes more stable as the particle size increases, consistent with the Asakura-Oosawa theory. In contrast, the osmotic B is positive for the solute particles with $\sigma \leq 5\sigma_{\mathrm{v}}$, suggesting that the effective interactions are repulsive. B decreases with increasing σ from $5\sigma_{\mathrm{v}}$ to $6\sigma_{\mathrm{v}}$ and turns nearly zero at $\sigma = 6\sigma_{\mathrm{v}}$. In the σ range from $7\sigma_{\mathrm{v}}$ to $50\sigma_{\mathrm{v}}$, B is negative and decreases as σ increases, so the inter-particle effective interaction is more attractive with increasing particle size. We analyze the σ dependence of B in detail based on the thermodynamic identity for the osmotic virial coefficients [K. Koga, V. Holten, and B. Widom, *J. Phys. Chem. B*, 2015, **119**, 13391].

4.1 INTRODUCTION

Any macromolecule in a solution has an excluded volume from which solvent molecules are excluded (Figure 4.1(a)). If two macromolecules are close to each other, their excluded volumes overlap (Figure 4.1(b)), and the configuration entropy of surrounding solvent molecules becomes greater. An attractive interaction between two macromolecules is thus entropically induced. Asakura and Oosawa proposed this "excluded volume effect" about 70 years ago.[12] The Asakura-Oosawa (AO) theory is simple but has been applied to various research subjects, such as colloidal aggregation, protein stability, and so on (see the recent review[108] for the AO theory and reference therein).

The inter-solute effective interaction in a solution can be represented by the potential $w(r)$ of mean force for pairs of solutes, and the magnitude of that interaction can be measured by its first minimum. If we apply the AO theory to the system consisting of a pair of hard-sphere solute particles with a diameter σ immersed in hard-sphere solvent particles with $\sigma_{\rm v}$, the contact minimum $w(\sigma)$ is[12]

$$\frac{w(\sigma)}{\eta kT} = -\frac{3}{2}\sigma^* - 1, \tag{4.1}$$

where η is the packing fraction of solvent particles, k is Boltzmann's constant, T is the temperature, and σ^* is the solute diameter σ divided by $\sigma_{\rm v}$. Eq. (4.1) indicates that $w(\sigma)$ linearly decreases with increasing σ, i.e., the strength of the inter-particle effective interaction is enhanced as the particle size increases.

The osmotic second virial coefficient B also quantifies the strength of the solute-solute effective interaction. B is defined as the coefficient in the expansion of the osmotic pressure Π with respect to the number density ρ of the solute at fixed T and solvent chemical potential $\mu_{\rm v}$. B is related to the effective potential $w(r)$, or equivalently, the radial distribution function $g(r) = \exp\left[-w(r)/kT\right]$ in an infinitely dilute solution:[9]

$$B = -\frac{1}{2}\lim_{\rho\to 0}\int\left[\exp\left[-\frac{w(r)}{kT}\right] - 1\right]d\boldsymbol{r} = -\frac{1}{2}G \tag{4.2}$$

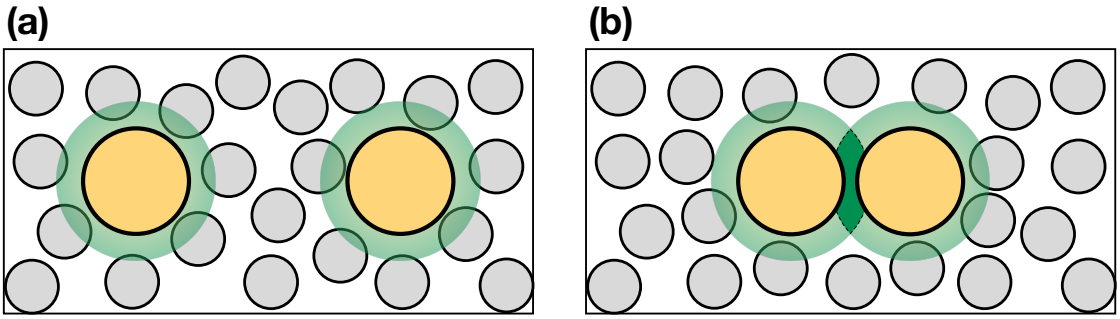

Figure 4.1: Schematic representation of the excluded volume effect.[12] Yellow and grey circles represent macromolecules and solvent particles, respectively. Green circles are the excluded volume of the macromolecule, from which the centers of solvent particles are excluded. Two macromolecules are (a) far apart and (b) close together, in the latter case, two excluded volumes overlap (shown in dark green).

where $d\boldsymbol{r}$ is an infinitesimal volume element, and $G = \lim_{\rho \to 0} \int [g(r) - 1] d\boldsymbol{r}$ is the solute-solute Kirkwood-Buff integral[7] at infinite dilution.

The solute-size effect on the effective interaction between solute particles has been crucial in the theory of liquids.[35]–[41], [62], [109]–[112] In addition, the size dependence of the effective interaction between nonpolar solutes in water or aqueous solutions has been extensively studied using the theoretical approach[29], [32], [66], [67], [87], [97], [98] and molecular simulation.[4]–[6], [16], [17], [33], [34], [65], [76], [79], [99], [113] They calculated the effective potentials $w(r)$ or the corresponding $g(r)$ for various molecules of different sizes and shapes. However, the data of B are still limited to small-size solutes, such as methane,[19], [21], [25], [114] argon-size hard-sphere particle,[22] noble gases,[18], [23], [24] and other molecules[20], [26] in water.

Recent molecular dynamics (MD) simulation studies showed $w(r)$ and B for Lennard-Jones (LJ) particles of different LJ diameters σ ranging from methane's size to C_{60} fullerene's size in water.[65], [76], [113] The MD results indicate that the contact minimum of $w(r)$ and the osmotic B are both negative and decrease with increasing σ. This size dependence is qualitatively the same as the AO expression Eq. (4.1) of the contact minimum $w(\sigma)$ for pairs of hard-sphere particles.

We also obtained the quantitative relationship between B and σ as the power law

$B \propto \sigma^{\alpha}$ with $\alpha = 6$ or 7.[65], [76], [113] The following thermodynamic identity partially supports the 6th power law between B and σ:[10], [27]

$$B = B'' - \frac{(v - kT\chi)^2}{2kT\chi}, \tag{4.3}$$

where B'' is the coefficient in $\Pi = \rho kT(1 + B''\rho + \cdots)$ at fixed solvent number density ρ_{v}. v is the partial molecular volume of the solute at infinite dilution and χ is the isothermal compressibility of the pure solvent. The partial molecular volume v is proportional to the solute volume because it corresponds to the increase of the system volume with inserting a solute into the system. Therefore, the second term in Eq. (4.3) is proportional to the 6th power of σ, and the other σ dependence of B, such as $B \propto \sigma^7$, might be due to the σ dependence of B''.

The first term B'' in Eq. (4.3) is defined as the coefficient in the ρ expansion of Π, or equivalently, an infinitesimal change of the solute excess chemical potential μ^* with respect to ρ at fixed T and ρ_{v}:[31]

$$B'' = \frac{1}{2kT} \lim_{\rho \to 0} \left(\frac{\partial \mu^*}{\partial \rho} \right)_{T, \rho_{\mathrm{v}}}. \tag{4.4}$$

Eq. (4.4) indicates that if $B'' > 0$, μ^* increases with increasing solute density. In fact, B'' is usually positive.[28] B'' is also related to the volume integral of the solute-solute direct correlation function $c_{\mathrm{uu}}(r)$ at solute-infinite dilution:[30], [31]

$$B'' = -\frac{1}{2} \lim_{\rho \to 0} \int c_{\mathrm{uu}}(r) d\boldsymbol{r}. \tag{4.5}$$

Further calculation for much larger-size solutes is crucial to clarify the quantitative relationship between the strength of the solute-solute effective interaction and the solute size. However, enormous computational time and resources are necessary to obtain B based on the molecular simulation. To save these costs, we apply the integral equation theory to the two-component hard-sphere mixtures, the most fundamental system in the theory of liquids. We calculate B, B'', and v for hard-sphere particles with different

diameters σ and discuss the σ dependence of each term in the thermodynamics identity Eq. (4.3).

4.2 COMPUTATIONAL DETAILS

4.2.1 Thermodynamic Identity for Osmotic Second Virial Coefficient

The thermodynamic identity Eq. (4.3) was originally derived based on the thermodynamical argument.[10] Here, we start from the Ornstein-Zernike (OZ) equation to derive this identity.[115] The OZ equation for the two-component system consisting of solute and solvent particles in the limit of solute-infinite dilution $\rho \to 0$ is[116]

$$h_{ij}(r) = c_{ij}(r) + \rho_{\mathrm{v}} \int c_{i\mathrm{v}}(|\boldsymbol{r} - \boldsymbol{r'}|) h_{\mathrm{v}j}(r') d\boldsymbol{r'}, \tag{4.6}$$

where $h_{ij}(r)$ and $c_{ij}(r)$ are the total and direct correlation functions, respectively, for pairs of particles i and j.

Taking the Fourier transform of both sides in Eq. (4.6) gives

$$\begin{aligned} \int h_{ij}(r) \exp\left[-i\boldsymbol{k}\cdot\boldsymbol{r}\right] d\boldsymbol{r} = &\int c_{ij}(r) \exp\left[-i\boldsymbol{k}\cdot\boldsymbol{r}\right] d\boldsymbol{r} \\ &+ \rho_{\mathrm{v}} \int\int c_{i\mathrm{v}}(|\boldsymbol{r} - \boldsymbol{r'}|) h_{\mathrm{v}j}(r') \exp\left[-i\boldsymbol{k}\cdot\boldsymbol{r}\right] d\boldsymbol{r'} d\boldsymbol{r}, \end{aligned} \tag{4.7}$$

where $k = |\boldsymbol{k}|$ is the wave number. The second term in the right-hand side of Eq. (4.7) includes the convolution integral, so this term can be rewritten with $\boldsymbol{r''} \equiv \boldsymbol{r} - \boldsymbol{r'}$ as

$$\begin{aligned} &\rho_{\mathrm{v}} \int\int c_{i\mathrm{v}}(|\boldsymbol{r''}|) h_{\mathrm{v}j}(r') \exp\left[-i\boldsymbol{k}\cdot\boldsymbol{r'}\right] \exp\left[-i\boldsymbol{k}\cdot\boldsymbol{r''}\right] d\boldsymbol{r'} d\boldsymbol{r''} \\ &= \rho_{\mathrm{v}} \int h_{\mathrm{v}j}(r') \exp\left[-i\boldsymbol{k}\cdot\boldsymbol{r'}\right] d\boldsymbol{r'} \int c_{i\mathrm{v}}(r'') \exp\left[-i\boldsymbol{k}\cdot\boldsymbol{r''}\right] d\boldsymbol{r''}. \end{aligned} \tag{4.8}$$

In the limit of $k \to 0$, Eq. (4.7) reduces to

$$G_{ij} = \int c_{ij}(r) d\boldsymbol{r} + \rho_{\mathrm{v}} G_{\mathrm{v}j} \int c_{i\mathrm{v}}(r'') d\boldsymbol{r''}, \tag{4.9}$$

where $G_{ij} = \int h_{ij}(r) d\boldsymbol{r}$ is the Kirkwood-Buff (KB) integral[7] for pairs of i and j.

Eq. (4.9) gives the expressions for the solute-solvent and solute-solute KB integrals, G_{uv} and G_{uu}:

$$G_{\mathrm{uv}} = \int c_{\mathrm{uv}}(r) d\boldsymbol{r} + \rho_{\mathrm{v}} G_{\mathrm{vv}} \int c_{\mathrm{uv}}(r'') d\boldsymbol{r''} \tag{4.10}$$

and

$$G_{\mathrm{uu}} = \int c_{\mathrm{uu}}(r) d\boldsymbol{r} + \rho_{\mathrm{v}} G_{\mathrm{uv}} \int c_{\mathrm{uv}}(r'') d\boldsymbol{r''}, \tag{4.11}$$

where G_{vv} is the solvent-solvent KB integral. Note that $G_{\mathrm{vu}} = G_{\mathrm{uv}}$ (see Section 1.2). From Eqs. (4.10) and (4.11),

$$-\frac{1}{2} G_{\mathrm{uu}} = -\frac{1}{2} \int c_{\mathrm{uu}}(r) d\boldsymbol{r} - \frac{\rho_{\mathrm{v}} G_{\mathrm{uv}}^2}{2(1 + \rho_{\mathrm{v}} G_{\mathrm{vv}})}. \tag{4.12}$$

The left-hand side in Eq. (4.12) is equal to the osmotic second virial coefficient B since $h_{\mathrm{uu}}(r) = g(r) - 1$. Also,[8]

$$G_{\mathrm{uv}} = -v + kT\chi \tag{4.13}$$

and

$$G_{\mathrm{vv}} = kT\chi - \frac{1}{\rho_{\mathrm{v}}}, \tag{4.14}$$

where v is the partial molecular volume of the solute at infinite dilution and χ is the isothermal compressibility of the pure solvent. On substitution of Eqs. (4.13) and (4.14) into Eq. (4.12),

$$B = -\frac{1}{2} \int c_{\mathrm{uu}}(r) d\boldsymbol{r} - \frac{(v - kT\chi)^2}{2kT\chi}. \tag{4.15}$$

Comparison of Eqs. (4.3) and (4.15) yields the equality Eq. (4.5).

4.2.2 Integral Equation Theory for Simple Liquids

The integral equation theory is a theoretical approach to calculate the correlation functions $h_{ij}(r)$ and $c_{ij}(r)$ by solving the OZ equation iteratively or numerically. Now we define the difference between these functions as $\gamma_{ij}(r) \equiv h_{ij}(r) - c_{ij}(r)$. The OZ equation Eq. (4.6) gives the expressions for the solvent-solvent, solute-solvent, and solute-solute correlation functions:

$$\gamma_{\mathrm{vv}}(r) = \rho_{\mathrm{v}} \int c_{\mathrm{vv}}(|\boldsymbol{r} - \boldsymbol{r'}|)\big[\gamma_{\mathrm{vv}}(r') + c_{\mathrm{vv}}(r')\big] d\boldsymbol{r'}, \tag{4.16}$$

$$\gamma_{\mathrm{uv}}(r) = \rho_{\mathrm{v}} \int c_{\mathrm{vv}}(|\boldsymbol{r} - \boldsymbol{r'}|)\big[\gamma_{\mathrm{uv}}(r') + c_{\mathrm{uv}}(r')\big] d\boldsymbol{r'}, \tag{4.17}$$

$$\gamma_{\mathrm{uu}}(r) = \rho_{\mathrm{v}} \int c_{\mathrm{uv}}(|\boldsymbol{r} - \boldsymbol{r'}|)\big[\gamma_{\mathrm{uv}}(r') + c_{\mathrm{uv}}(r')\big] d\boldsymbol{r'}. \tag{4.18}$$

The other relation between $\gamma_{ij}(r)$ and $c_{ij}(r)$, which is called the closure relation,[116] is necessary to solve Eqs. (4.16)-(4.18). The closure relation is generally represented by

$$c_{ij}(r) = \exp\big[-\phi_{ij}(r)/kT + \gamma_{ij}(r) + b_{ij}(r)\big] - \gamma_{ij}(r) - 1, \tag{4.19}$$

where $\phi_{ij}(r)$ and $b_{ij}(r)$ are the direct pair potential and the bridge function, respectively, for pairs of i and j. In the case of hard-sphere mixtures, $\phi_{ij}(r) = \infty$ for $r < \sigma_{ij} = (\sigma_i + \sigma_j)/2$ and $\phi_{ij}(r) = 0$ for $r > \sigma_{ij}$ with σ_i being the hard-sphere diameter of a particle i. Then,

$$c_{ij}(r) = \begin{cases} -\gamma_{ij}(r) - 1 & (r < \sigma_{ij}) \\ \exp\big[\gamma_{ij}(r) + b_{ij}(r)\big] - \gamma_{ij}(r) - 1 & (r > \sigma_{ij}). \end{cases} \tag{4.20}$$

The functional form of $b_{ij}(r)$ has significant effects on the numerical result derived from the integral equation theory. The Percus-Yevick (PY) and hypernetted-chain (HNC) approximations are well-known, in the latter case, $b_{ij}(r) = 0$. Analytical solutions of the pair correlation functions for multi-component hard-sphere mixtures were obtained using the PY approximation,[117] but the PY results of the radial distribution function

$g_{ij}(r)$ could have regions with negative values.[109], [118], [119] In contrast, Nakamura et al. applied the MHNC closure relation[11] to solve the OZ equation and clarified that the numerical results of $g_{\mathrm{uv}}(r) = h_{\mathrm{uv}}(r) + 1$ are good agreement with the canonical Monte Carlo (MC) simulation results for hard-sphere particles of various diameters σ up to $\sigma^* = \sigma/\sigma_{\mathrm{v}} = 50$.[120] The MHNC bridge function is

$$b_{ij}(r) = -0.5\frac{\gamma_{ij}^2(r)}{1 + 0.8|\gamma_{ij}(r)|}. \tag{4.21}$$

Eq. (4.21) is similar to the formula proposed by Verlet,[121] the difference is in the denominator ($|\gamma_{ij}(r)|$ instead of $\gamma_{ij}(r)$). Matsuo et al. also applied this MHNC closure to calculate the spatial distribution function $g_{\mathrm{uv}}(x, y, z)$ of solvent particles around a solute pair based on the three-dimensional OZ equation.[122] They validated the MHNC closure relation compared with the grand canonical MC result.

We apply the HNC and MHNC closure relations to solve the OZ equations Eqs. (4.16)-(4.18). The computation procedure is as follows: First, Eq. (4.16) was solved iteratively to obtain the solvent-solvent correlation functions $c_{\mathrm{vv}}(r)$ and $h_{\mathrm{vv}}(r) = \gamma_{\mathrm{vv}}(r)+c_{\mathrm{vv}}(r)$. The latter function was used to calculate χ based on Eq. (4.14). $c_{\mathrm{vv}}(r)$ was the input data to solve Eq. (4.17) iteratively. The resulting solute-solvent correlation function $h_{\mathrm{uv}}(r)$ was the source to obtain v from Eq. (4.13). $h_{\mathrm{uv}}(r)$ and $c_{\mathrm{uv}}(r)$ were the input to solve Eq. (4.18) numerically. Then the resulting solute-solute correlation functions $h_{\mathrm{uu}}(r)$ and $c_{\mathrm{uu}}(r)$ were used to compute B from Eq. (4.2) and B'' from Eq. (4.5), respectively.

Our target solution is the two-component hard-sphere mixture of a pair of solute particles with diameter σ immersed in solvent particles with diameter σ_{v}. The solvent number density ρ_{v} was determined based on the molecular dynamics (MD) simulation of pure water at the pressure $p = 1$ bar and temperature $T = 300$ K using GROMACS 2018.[56] The three-dimensional periodic boundary condition was applied to the cubic system containing 4000 water molecules. The TIP4P/2005 potential function[53] represented the direct pair interaction between water molecules. The LJ potential between oxygen atoms of water molecules was truncated at 1.1 nm. The cutoff distance of the Coulomb potential was 1.1 nm in real space, and the long-range part of that potential was computed by the

particle mesh Ewald method. The pressure and temperature were controlled using the Parinello-Rahman method and the Nosé-Hoover method, respectively. From 10 ns MD simulation, we obtained the average number density $\rho_{\rm v} = 33.45$ nm^{-3} and the radial distribution function $g_{\rm vv}(r)$ between water molecules. The oxygen-oxygen distance r of the first maximum of $g_{\rm vv}(r)$ is about 0.28 nm, consistent with the scattering experiment.[123] We set the diameter of a solvent particle as $\sigma_{\rm v} = 0.28$ nm. The reduced number density and the packing fraction are thus $\rho^* = \rho_{\rm v}\sigma_{\rm v}^3 = 0.7343$ and $\eta = \pi\rho^*/6 \simeq 0.3845$, respectively.

The remaining parameters to solve the OZ equations are as follows: The hard-sphere diameters $\sigma^* = \sigma/\sigma_{\rm v}$ of solute particles are 1, 2, 3, 4, 5, 6, 7, 8, 10, 12, 14, 16, 20, 25, 30, 35, 40, 45, and 50. The maximum value $r_{\rm max}$ and the grid width dr for the numerical integration with respect to r are $r_{\rm max}/\sigma_{\rm v} = 500$ and $dr/\sigma_{\rm v} = 1/140$, respectively. We set $r_{\rm max}/\sigma_{\rm v} = 1000$ and $dr/\sigma_{\rm v} = 1/280$ only to calculate χ. For the inverse Fourier transform from k to r, the maximum value and the grid width are set to $2\pi/dr$ and $2\pi/r_{\rm max}$, respectively.

4.2.3 Monte Carlo Simulation

To check whether the HNC or MHNC approximation is better as the closure relation of the OZ equation, we performed the MC simulation to obtain the effective potentials $w(r)$ for pairs of solute particles with $\sigma^* = 1$, 2, 3, and 4 at $\rho^* = 0.7343$. Table 4.1 displays the number N of solute particles, the $N_{\rm v}$ of solvent particles, the cell length $L^* = L/\sigma_{\rm v}$ of the cubic simulation box, and the total number of MC steps. To get the initial configuration, 27 solute particles were arranged in the $3\times3\times3$ lattice configuration in the simulation box with L^3, and solvent particles were inserted randomly into the box without overlapping with solute and other solvent particles.

Table 4.1: Computational details of the MC simulations for hard-sphere particles with $\sigma^* = 1$, 2, 3, and 4 in a hard-sphere solvent. N and N_v are the numbers of solute and solvent particles, respectively, and L^* is the cell length L of the cubic simulation box divided by σ_v.

σ^*	N	N_v	L^*	MC steps
1	27	4000	17.72	10^{10}
2	27	16000	28.09	1.6×10^{11}
3	27	16000	28.31	1.6×10^{11}
4	27	16000	28.67	1.6×10^{11}

4.2.4 Asakura-Oosawa Theory and Boubík-Mansoori-Carnahan -Starling-Leland Equation of State

In the present work, we compare the numerical results derived from the integral equation theory with the analytical expressions from the Asakura-Oosawa (AO) theory[12] and the Boubík-Mansoori-Carnahan-Starling-Leland (BMCSL) equation of state.[13], [14] The AO theory gives the inter-particle effective potential $w(r)$ as a function of $r^* = r/\sigma_\mathrm{v}$:

$$\frac{w(r)}{\eta kT} = \begin{cases} \infty \quad (r^* < \sigma^*), \\ -(\sigma^*+1)^3 + \frac{3}{2}(\sigma^*+1)^2 r^* - \frac{1}{2}(r^*)^3 \quad (\sigma^* \le r^* < \sigma^*+1), \\ 0 \quad (r^* \ge \sigma^*+1). \end{cases} \tag{4.22}$$

Eq. (4.22) reduces to Eq. (4.1) when $r^* = \sigma^*$.

The BMCSL equation of state is a well-known equation for the multi-component mixture of hard-sphere particles:

$$\frac{p}{kT} = \frac{6}{\pi}\left[\frac{\xi_0}{(1-\xi_3)} + \frac{3\xi_1\xi_2}{(1-\xi_3)^2} + \frac{(3-\xi_3)\xi_2^3}{(1-\xi_3)^3}\right], \tag{4.23}$$

where $\xi_m = \pi \sum_i \rho_i \sigma_i^m/6$. Eq. (4.23) was firstly derived from the expression for the contact

value of $g_{ij}(r)$:[13]

$$g_{ij}(\sigma_{ij}) = \frac{1}{1-\xi_3} + \frac{3\xi_2\sigma_i\sigma_j}{(1-\xi_3)^2(\sigma_i+\sigma_j)} + \frac{2\xi_2^2\sigma_i^2\sigma_j^2}{(1-\xi_3)^3(\sigma_i+\sigma_j)^2} \tag{4.24}$$

because $g_{ij}(\sigma_{ij})$ is directly related to p/kT in the case of hard-sphere fluids:[8], [116]

$$\frac{p}{kT} = \sum_i \rho_i + \frac{2\pi}{3}\sum_i\sum_j \rho_i\rho_j\sigma_{ij}^3 g_{ij}(\sigma_{ij}). \tag{4.25}$$

Now we consider the two-component hard-sphere mixture at solute-infinite dilution. The first minimum of the solute-solute effective potential $w(\sigma)/kT = -\ln g(\sigma)$ is now

$$\frac{w(\sigma)}{kT} = -\ln\left[\frac{1}{1-\eta} + \frac{3\eta}{2(1-\eta)^2}\sigma^* + \frac{\eta^2}{2(1-\eta)^3}(\sigma^*)^2\right] \tag{4.26}$$

since $\xi_3 = \pi\rho_{\rm v}\sigma_{\rm v}^3/6 = \eta$ in the limit of $\rho \to 0$.

We can also yield the analytical expressions for B, B'', v, and χ from Eq. (4.23) because the Helmholtz free energy density f is related to the equation of state by[116]

$$f = \bar{\rho}kT\int_0^{\bar{\rho}} \frac{1}{\rho'}\left[\frac{p}{\rho' kT} - 1\right]d\rho' \tag{4.27}$$

with $\bar{\rho} = \sum_i \rho_i$. On substitution of Eq. (4.23) into Eq. (4.27),

$$f = \bar{\rho}kT\left[\left(\frac{\xi_2^3}{\xi_0\xi_3^2} - 1\right)\ln(1-\xi_3) + \frac{3\xi_1\xi_2}{\xi_0(1-\xi_3)} + \frac{\xi_2^3}{\xi_0\xi_3(1-\xi_3)^2}\right]. \tag{4.28}$$

The derivation was explained elsewhere,[29]–[31] so we only show the final results of the analytical expressions for $1/kT\chi$, $v - kT\chi$, and B'':

$$\frac{1}{kT\chi} = \rho_{\rm v}\left[1 + \frac{6\eta^2+8\eta}{(1-\eta)^3} + \frac{6\eta^3}{(1-\eta)^4}\right]. \tag{4.29}$$

$$v - kT\chi = kT\chi\left[\frac{\eta}{1-\eta} + \frac{3\eta}{(1-\eta)^2}\sigma^* + \left[\frac{3\eta^2+3\eta}{(1-\eta)^2} + \frac{6\eta^2}{(1-\eta)^3}\right](\sigma^*)^2 + \left[\frac{2\eta}{1-\eta} + \frac{6\eta^2-\eta}{(1-\eta)^2} + \frac{6\eta^3+2\eta^2}{(1-\eta)^3} + \frac{6\eta^3}{(1-\eta)^4}\right](\sigma^*)^3\right]. \quad (4.30)$$

$$B'' = \frac{\eta}{2\rho_v}\left[\frac{8}{1-\eta}(\sigma^*)^3 + \left[\frac{6}{\eta}\ln(1-\eta) + \frac{6\eta+6}{(1-\eta)^2}\right](\sigma^*)^4 + \left[-\frac{12}{\eta}\ln(1-\eta) - \frac{12}{1-\eta} + \frac{12\eta}{(1-\eta)^3}\right](\sigma^*)^5 + \left[\frac{6}{\eta}\ln(1-\eta) + \frac{4}{1-\eta} + \frac{2}{(1-\eta)^2} + \frac{6\eta^2-4\eta}{(1-\eta)^3} + \frac{6\eta^2}{(1-\eta)^4}\right](\sigma^*)^6\right]. \quad (4.31)$$

Eqs. (4.30) and (4.31) suggest that when σ is sufficiently large, $v - kT\chi$ and B'' should be proportional to σ^3 and σ^6, respectively. B is obtained from Eqs. (4.29)-(4.31) coupled with Eq (4.3).

4.3 RESULTS AND DISCUSSION

First, we compare the solute-solute effective potentials $w(r)$ derived from the integral equation theory with those obtained from the MC simulation. Figure 4.2(a) shows the MC and HNC results of $w(r)$ for pairs of solute particles with hard-sphere diameters $\sigma^* = \sigma/\sigma_v$ = 1, 2, 3, and 4. The contact minimum decreases with increasing σ, which is consistent with Eq. (4.1) obtained from the AO theory.[12] Figure 4.2(a) indicates that $w(r)$ by the HNC approximation is in good agreement with the simulation result. However, the HNC result underestimates the contact minimum $w(\sigma)/kT$ compared with the MC result: The former is $w(\sigma)/kT$ = -1.45, -2.16, -2.83, and -3.46 for σ^* = 1, 2, 3, and 4, respectively, while the latter is $w(\sigma)/kT$ = -1.24, -1.87, -2.19, and -2.92 at σ^* = 1, 2, 3, and 4.

Figure 4.2(b) displays $w(r)$ by the MHNC approximation.[11] The MHNC result is in excellent agreement with the MC result, especially at the contact distance: $w(\sigma)/kT$ = -1.22, -1.78, -2.28, and -2.75 for σ^* = 1, 2, 3, and 4, respectively. Figures 4.2(a) and

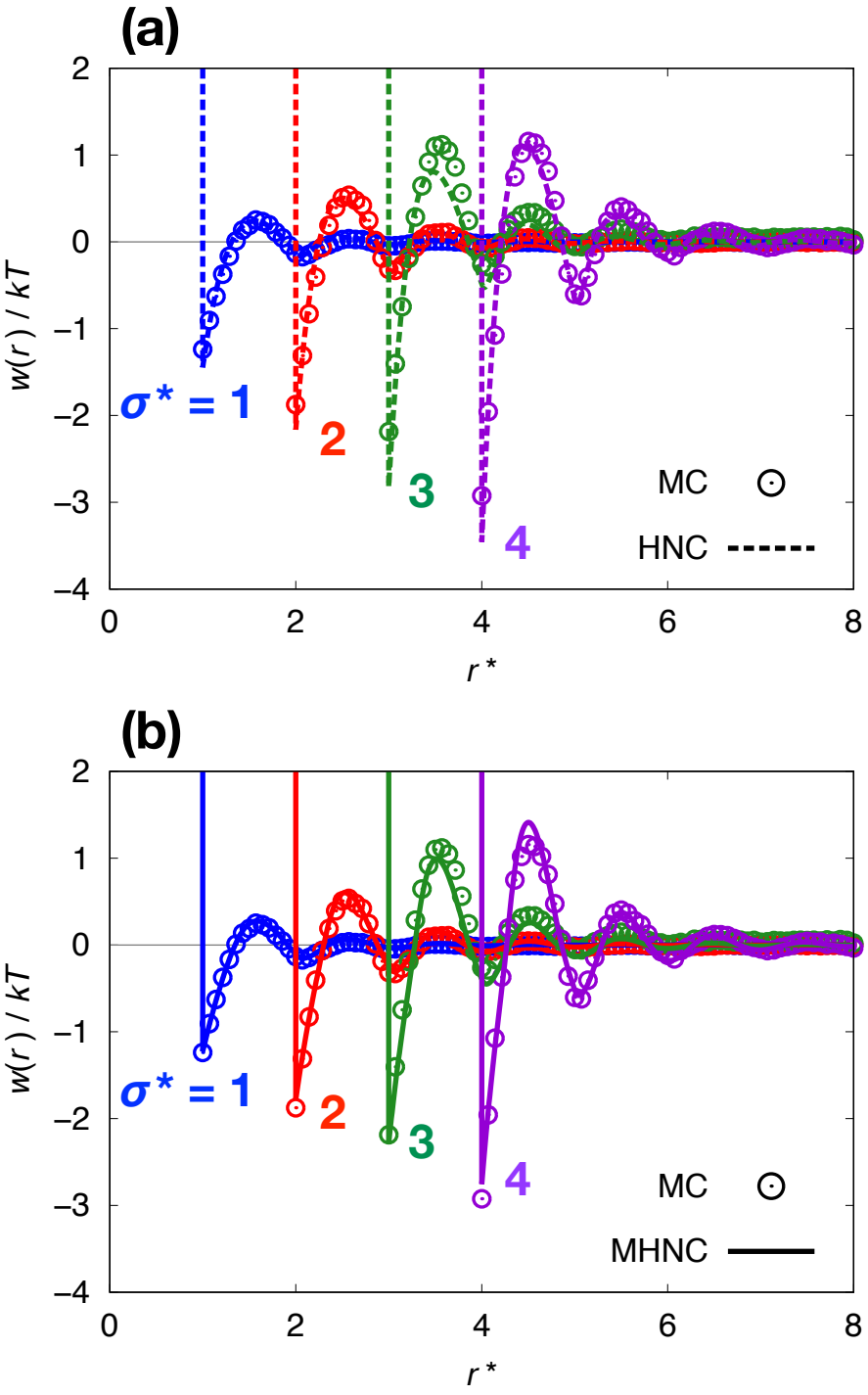

Figure 4.2: The potentials $w(r)$ of mean force between two hard-sphere particles of different diameters σ^* at the reduced solvent number density $\rho^* = 0.7343$. The hard-sphere diameters σ^* of solute particles are 1, 2, 3, and 4. The circles in (a) and (b) are the results obtained from the MC simulation. The dashed curves in (a) and the solid curves in (b) are the numerical results derived from the integral equation theory using the HNC and MHNC approximations, respectively.

(b) suggest that the MHNC approximation is better than the HNC approximation as the closure relation to solve the OZ equations.

Now we examine $w(r)$ for larger-size particles. Figure 4.3(a) shows the MHNC result for hard-sphere particles with σ^* ranging from 1 to 7 together with the AO potential Eq. (4.22). Remarkably, the MHNC result of the first minimum $w(\sigma)/kT$ agrees well with the AO result. Figure 4.3(b) is a plot of $w(\sigma)/kT$ against σ^*, which clearly shows the consistency of the MHNC and AO results.

This figure also includes the HNC result and the analysical expression Eq. (4.26) derived from the BMCSL equation of state.[13], [14] One can see that $w(\sigma)/kT$ by the HNC approximation is lower than that by the MHNC approximation. The BMCSL result is almost the same as the MHNC result for hard-sphere particles with $\sigma^* = 1$, 2, and 3, but for $\sigma^* \geq 4$, the former overestimates $w(\sigma)/kT$ compared with the latter.

The AO potential in Eq. (4.22) does not have peaks except at the contact distance, such as the first maximum and the second minimum, against the solute-solute distance r. The former maximum corresponds to the desolvation barrier, and the latter minimum is referred to the solvent-separated minimum. At the solvent-separated distance, the monolayer structure of the solvent separates two solute particles. The desolvation barrier is thus the potential energy to overcome to make the transition from the monolayer-separated state to the contact state. Mao et al. obtained these maximum and minimum from the analytical calculation for the depletion force between large spheres by considering up to the third order in the volume fraction of the solvent.[124]

Figure 4.3(a) displays that as the particle size increases, the desolvation barrier increases while the solvent-separated minimum decreases. The increment of the desolvation barrier with σ is consistent with the results for hydrophobic polyatomic sheets,[32] hydrocarbons,[4] and LJ particles[65], [113] in water. However, the σ dependence of the second minimum is different from the result for the aqueous solution: The solvent-separated minimum for the LJ particles in water increases with increasing particle size.[65], [113] The increase of the solvent-separated minimum would be characteristic of the hydrophobic interaction: Water molecules confined by two large hydrophobic solutes form a monolayer

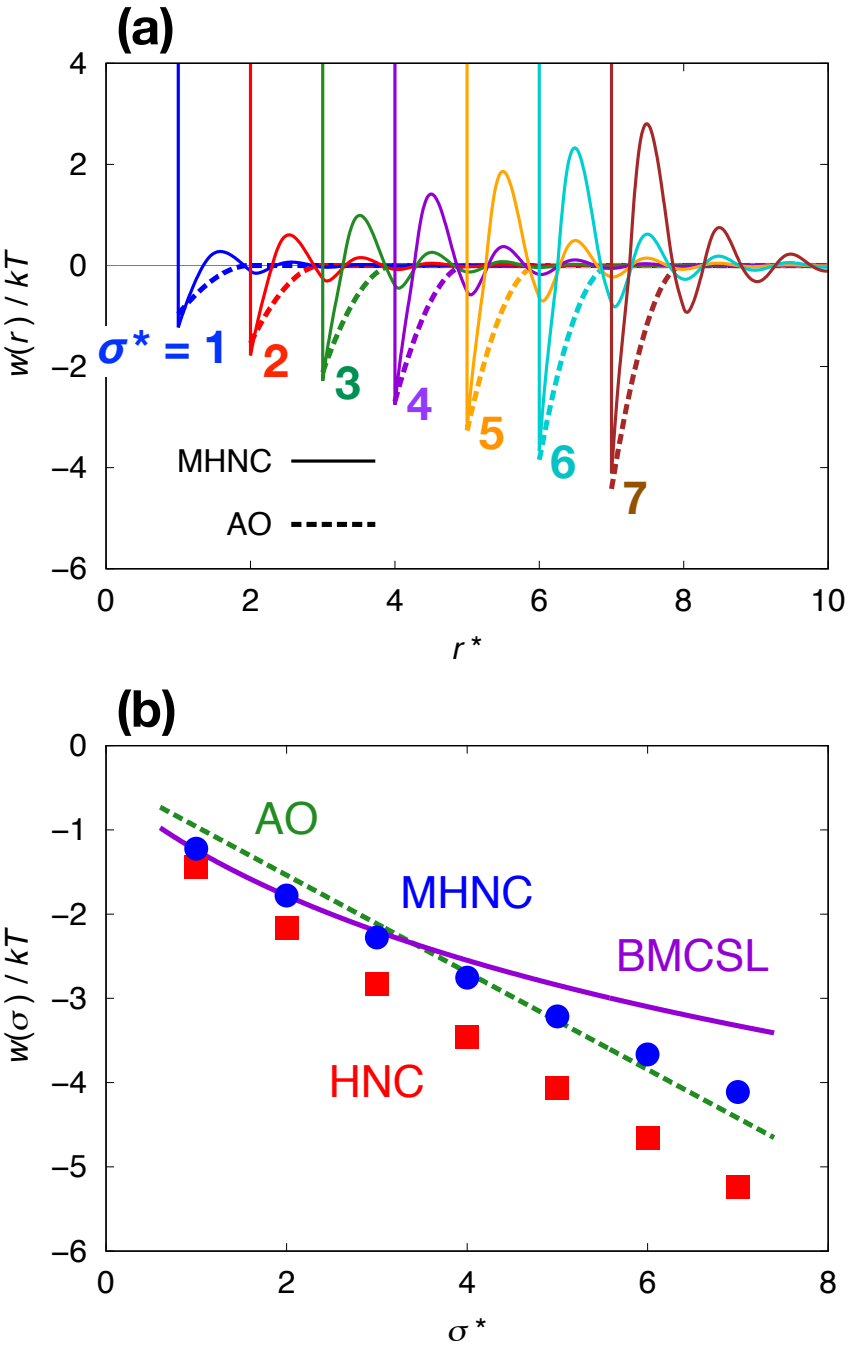

Figure 4.3: (a) The effective potentials $w(r)$ for pairs of hard-sphere particles with $\sigma^* =$ 1, 2, 3, 4, 5, 6, and 7. The solid curves are the numerical results derived from the integral equation theory using the MHNC approximation. The dashed curves are Eq. (4.22) obtained from the AO theory. (b) The plot of the contact minimum $w(\sigma)$ against σ^*. The dashed and solid lines represent the AO result Eq. (4.1) and the BMCSL result Eq. (4.26), respectively. The circles and squares are the numerical results by the MHNC and HNC approximations, respectively.

hydrogen-bond network, but it is energetically unstable (see Chapter 3).

Next, we examine the σ dependence of the osmotic second virial coefficient B. Figure 4.4(a) is a plot of B against σ^*. The AO theory shows that B is negative and that magnitude increases with σ. The AO result suggests that the inter-particle effective interaction is attractive, and its strength is enhanced as the particle size increases.

The BMCSL result obtained from Eqs. (4.29)-(4.31) coupled with Eq. (4.3) shows the opposite trend to the AO result: B is positive and increases with σ. Earlier studies pointed out that the BMCSL result is not accurate when the ratio of solute and solvent diameters is large.[111], [125]

Unlike the AO and BMCSL results, the osmotic B by the MHNC approximation has a non-monotonic σ dependence: In the σ^* range from 1 to 5, B is positive and becomes greater with σ, i.e., the effective interaction is repulsive and stronger as the particle size increases. On the other hand, $B \simeq 0$ for $\sigma^* = 6$ and $B < 0$ for $\sigma^* = 7$, so B decreases with increasing σ^* from 5 to 7. The HNC result of B shows a similar trend as the MHNC result: B is positive for the particles with $\sigma^* \leq 4$ but negative for $\sigma^* \geq 5$.

Why does the osmotic B change non-monotonically against σ? Here, we quantify the short r range contribution to B:

$$B_i = -2\pi \int_0^{r_i} \left[\exp\left[-\frac{w(r)}{kT} \right] - 1 \right] r^2 dr, \qquad i = 0 \text{ and } 1. \tag{4.32}$$

In Eq. (4.32), r_0 and r_1 are the inter-solute separations r of the first minimum and maximum of $w(r)$, respectively.

Figure 4.4(b) shows the MHNC results of B, B_0, and B_1 as a function of σ^*. Since the direct pair potential $\phi(r)$ is infinite in the range of r shorter than r_0, B_0 is the same as the second virial coefficient $B_{\text{gas}} = (2/3)\pi\sigma^3$ for hard-sphere gas with particle diameter σ. B_0 is positive and that magnitude increases with being proportional to the cubic of σ. It is remarkable that B_1 is almost the same value as the osmotic B for all-size particles. Similar results were obtained for the LJ particles in water based on the molecular simulation.[65], [76] Figure 4.4(b) indicates that the magnitude of B and its σ dependence could be largely determined by two contributions: One is the positive (repulsive) contri-

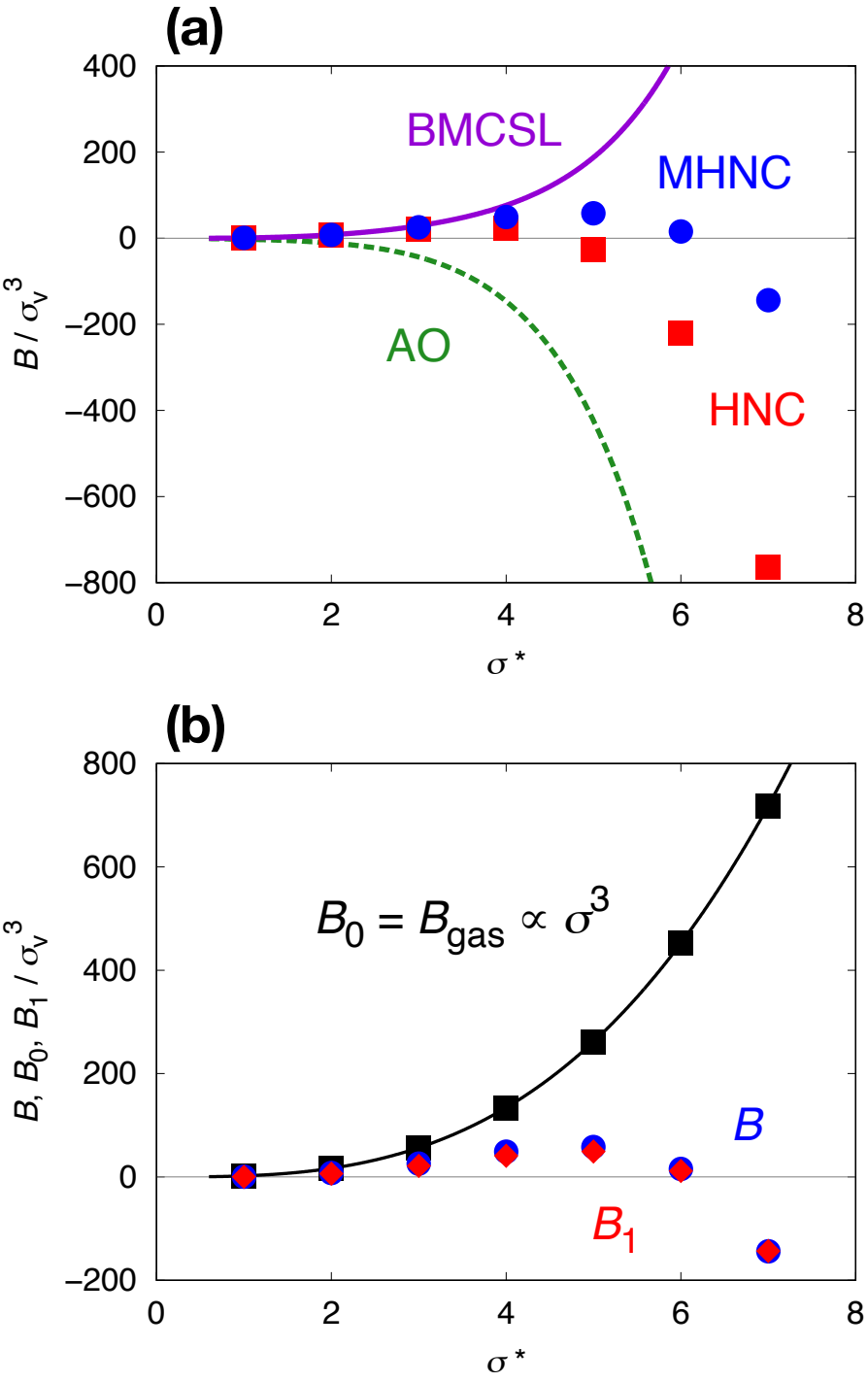

Figure 4.4: (a) The osmotic second virial coefficients B varying with σ^*. The dashed and solid lines are the AO and BMCSL results, respectively. The circles and squares represent the MHNC and HNC results, respectively. (b) The MHNC results of B, B_0, and B_1 vs. σ^*. B_0 and B_1 are defined by Eq. (4.32). The circles, squares, and diamonds represent the numerical results of B, B_0, and B_1, respectively. The solid line is the second virial coefficient $B_{\rm gas} = (2/3)\pi\sigma^3$ for hard-sphere gas as a function of its diameter σ.

bution B_0 from the direct pair potential $\phi(r)$, and the other is the negative (attractive) contribution $B_1 - B_0$ from $w(r)$ in the short-range $r_0 < r < r_1$.

From now on, we show the numerical results using the MHNC approximation and compare them with the analytical solutions derived from the BMCSL equation of state. Figure 4.5(a) displays the MHNC result of the solute-solute direct correlation functions $c_{\mathrm{uu}}(r)$ for pairs of solute particles with σ^* ranging from 4 to 16. $c_{\mathrm{uu}}(r)$ is negative in the range $r^* < \sigma^*$, but one can find a peak at $r^* = \sigma^*$. The inset in Figure 4.5(a) shows that the peak value $c_{\mathrm{uu}}(\sigma)$ is positive and increases as the particle diameter σ^* increases.

$c_{\mathrm{uu}}(r)$ is related to the coefficient B'' in the virial expansion of the osmotic pressure at fixed T and the solvent number density. Figure 4.5(b) is a log-log plot of B'' against σ^*. B'' is positive for all-size particles, which is consistent with the previous study.[28] The positive B'' means that the solute excess chemical potential increases with increasing the number of solutes at a fixed volume of the system (see Eq. (4.4)). The magnitude of B'' increases with σ^*, suggesting that the insertion of a solute particle into a fixed-volume system becomes harder as the particle size increases.

Figure 4.5(b) also includes the analytical expression Eq. (4.31) for B'' obtained from the BMCSL equation of state. Surprisingly, the BMCSL result is in excellent agreement with the MHNC numerical result: The latter is slightly larger than the former, but the relative error between them is up to 2.3 %. The highest-order term in the BMCSL expression for B'' as a function of σ is the 6th-power term. Therefore, the analytical and numerical results suggest the power-law behavior $B'' \propto \sigma^6$ for large-size particles.

Next, Figure 4.6(a) displays the solute-solvent total correlation functions $h_{\mathrm{uv}}(r)$ for solute particles with different diameters σ^*. The first peak height of $h_{\mathrm{uv}}(r)$ becomes higher with increasing σ, but that change is small for $\sigma^* \geq 10$. Nakamura et al. obtained similar results up to $\sigma^* = 50$ at almost the same solvent number density.[120] Figure 4.6(b) is a plot of $v - kT\chi = -\int h_{\mathrm{uv}}(r) d\boldsymbol{r}$ against σ^*, together with the BMCSL analytical expression Eq. (4.30). As well as the consistency of the analytical and numerical results of B'', the BMCSL result is in excellent agreement with the MHNC result. The latter is slightly larger, but the relative error between these results is up to 1.6 %. Both results

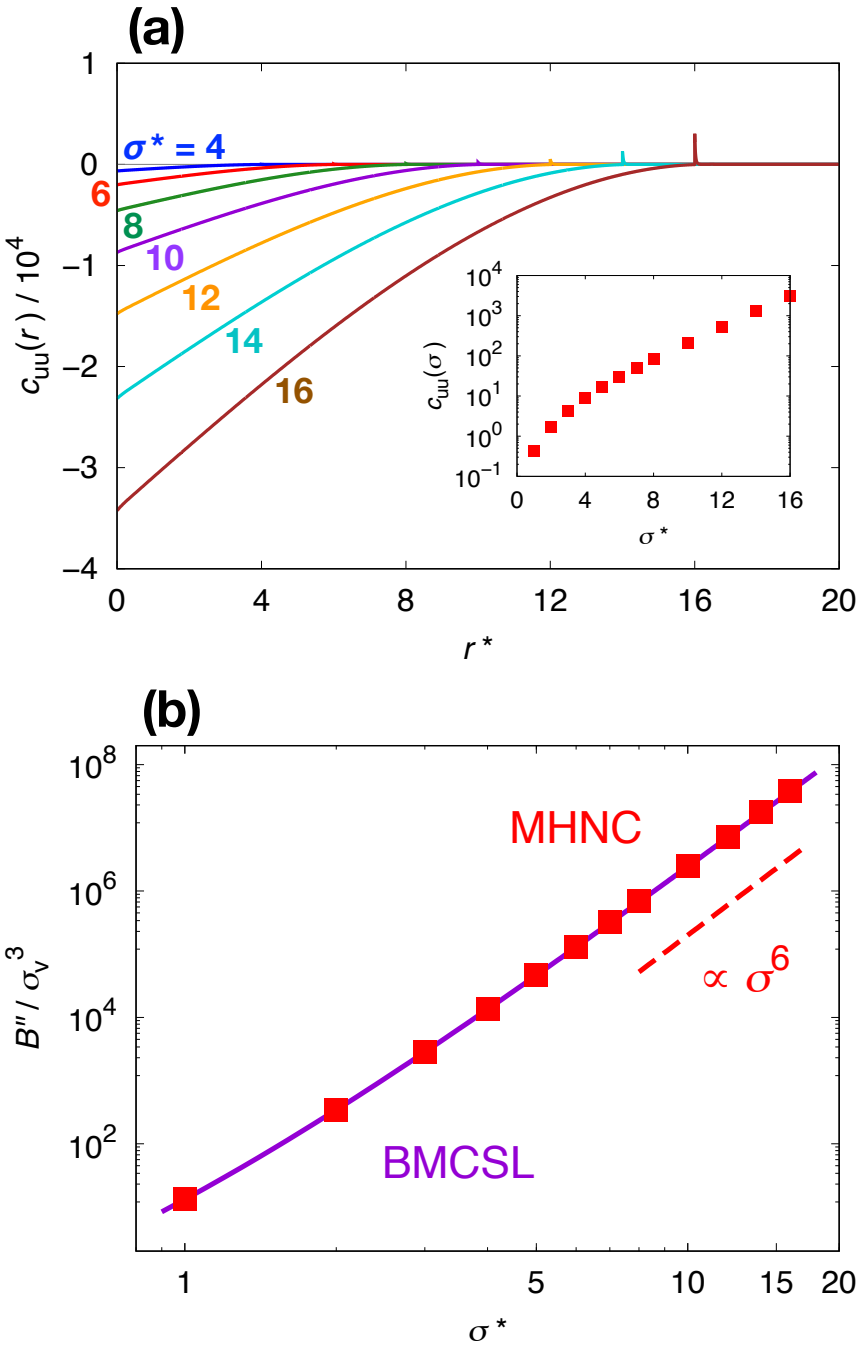

Figure 4.5: (a) The direct correlation functions $c_{uu}(r)$ for pairs of hard-sphere particles of different sizes. The solute diameters are $\sigma^* = 4$, 6, 8, 10, 12, 14, and 16. Note that the vertical axis is $c_{uu}(r)$ divided by 10000. The inset shows the peak value of $c_{uu}(r)$ against σ^* in a semi-log scale. (b) The log-log plot of $B'' = -(1/2)\int c_{uu}(r)d\boldsymbol{r}$ against σ^* ranging from 1 to 16. Squares represent the numerical result by the MHNC approximation. The solid line is Eq. (4.31) derived from the BMCSL equation of state. The dashed line is a straight line with a slope of 6.

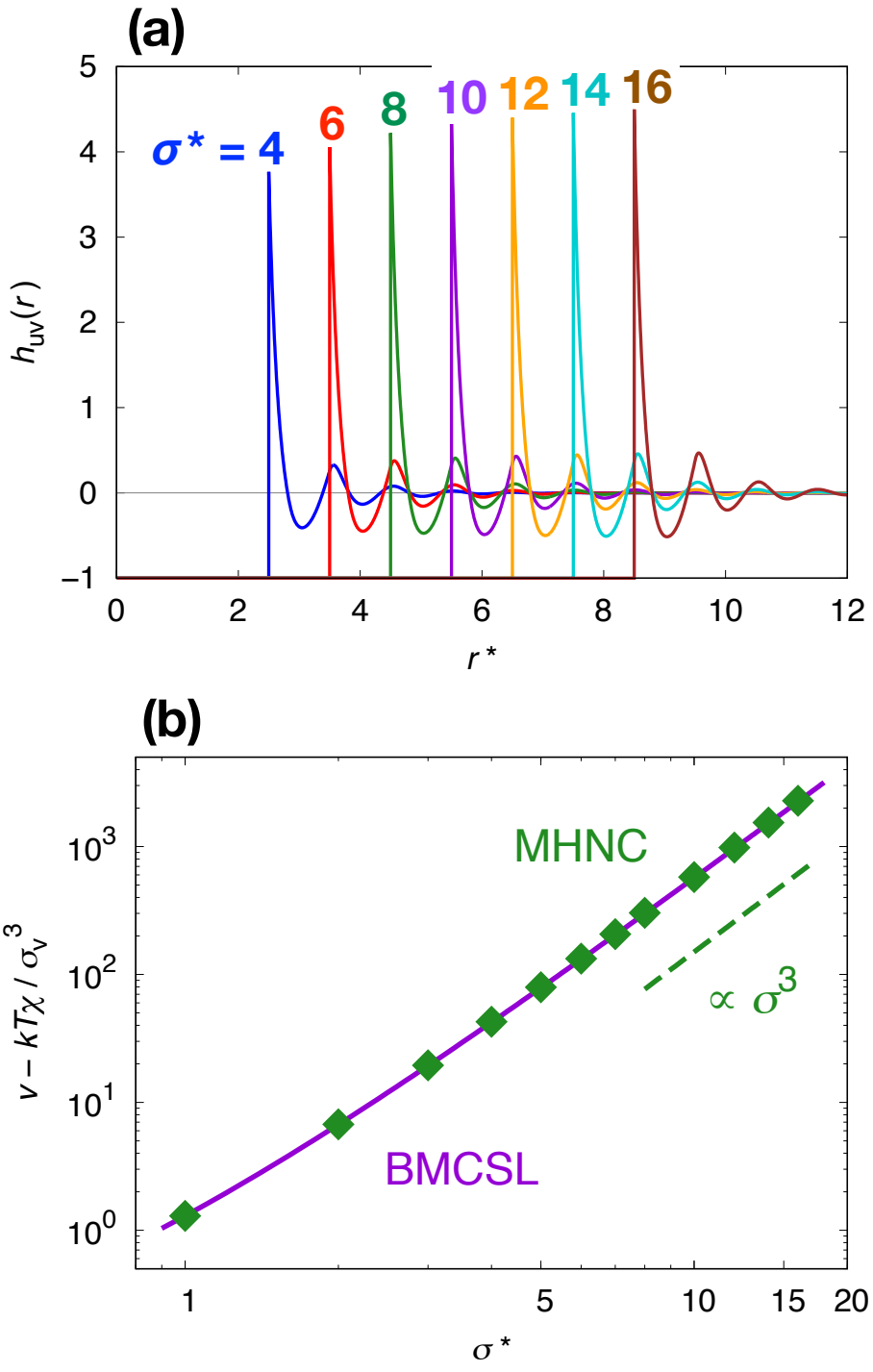

Figure 4.6: (a) The total correlation functions $h_{\rm uv}(r)$ for pairs of a solute particle and solvent particles. The solute diameter σ^* varies from 4 to 16 in 2 increments. (b) The log-log plot of $v - kT\chi = -\int h_{\rm uv}(r)d\boldsymbol{r}$ against σ^* ranging from 1 to 16. The diamonds represent the MHNC result, and the solid line is the BMCSL result Eq. (4.30). The dashed line is a straight line with a slope of 3.

indicate $v \propto \sigma^3$ for large-size solute particles, which is consistent with a physical point of view for the partial molecular volume v of the solute. Note that $v \gg kT\chi$ since the isothermal compressibility term $kT\chi$ is about $0.07\sigma_{\rm v}^3$ at $\rho^* = 0.7343$.

The osmotic B can be calculated by two routes: One is the volume integral of $\exp[-w(r)/kT]$ -1, and the other is the difference between B'' and $(v - kT\chi)^2/2kT\chi$. Figure 4.7(a) shows the absolute values of B depending on σ^*. The MHNC numerical results of B are that obtained from Eq. (4.2), but Eq. (4.3) coupled with the values of B'' (shown in Figure 4.5(b)), $v - kT\chi$ (in Figure 4.6(b)), and $kT\chi \simeq 0.07\sigma_{\rm v}^3$ also gives almost the same results.

In the σ^* range from 1 to 5, the inter-particle effective interaction becomes more repulsive with increasing σ. On the other hand, B for $\sigma^* \geq 7$ is negative, and that magnitude ascends with particle size. The BMCSL analytical results, obtained from Eqs. (4.29)-(4.31) coupled with Eq. (4.3), differ from the MHNC numerical results: B is positive for all-size particles and increases with increasing σ. The MHNC and BMCSL results of $|B|$ might appear to be close to each other for large particles, but they are completely different because their signs are opposite for the particles with $\sigma^* \geq 7$.

Figures 4.5(b) and 4.6(b) display that the BMCSL results of B'' and $v - kT\chi$ are in excellent agreement with the MHNC results of them. The relative errors among the two results are about 2 % for B'' and 3 % for $(v - kT\chi)^2/2kT\chi$. Nevertheless, why is the analytical expression for B not in agreement with the MHNC numerical result?

Cerdeirina et al. clarified that the first and second terms in Eq. (4.3) are largely canceled to give the osmotic B.[28] Figure 4.7(b) is a log-log plot of the absolute values of each term in Eq. (4.3) against σ^*. B'' and $(v - kT\chi)^2/2kT\chi$ are both positive and almost the same values. In the σ^* range from 1 to 6, B is positive because the magnitude of B'' is larger than that of $(v - kT\chi)^2/2kT\chi$. In contract, B is negative for $7 \leq \sigma^* \leq 16$, so the magnitude of B'' is smaller than that of $(v - kT\chi)^2/2kT\chi$. Interestingly, their magnitudes are 10^2 or 10^3 times larger than the magnitude of B. This result suggests that the relative errors with a few percent would have a considerable effect on the resulting $B = B'' - (v - kT\chi)^2/2kT\chi$.

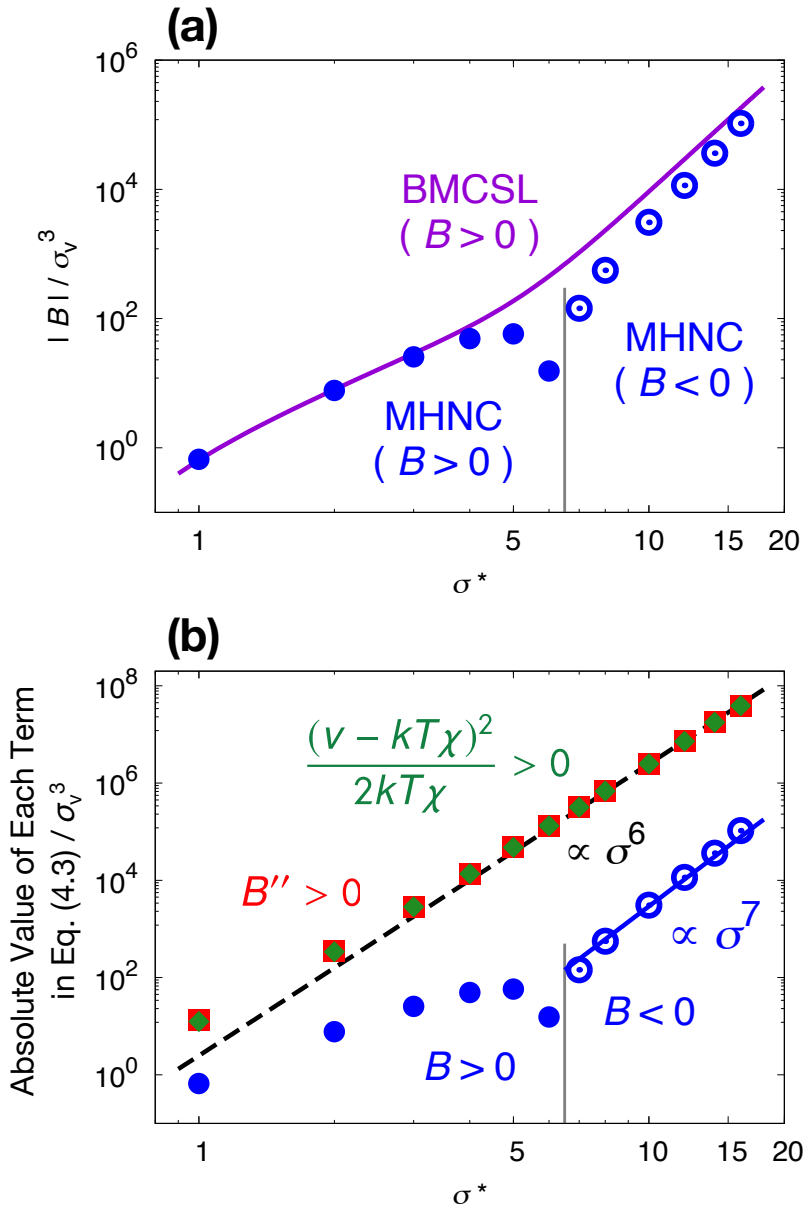

Figure 4.7: (a) The log-log plot of the absolute values of the osmotic B as a function of σ^*. The circles are the numerical results by the MHNC approximation. Note that the MHNC result of B is positive for $\sigma^* \leq 6$ while negative for $\sigma^* \geq 7$. The solid line is the analytical expression derived from the BMCSL equation of state. The BMCSL result of B is positive for all-size particles. (b) The log-log plot of the absolute values of each term in Eq. (4.3) against σ^*. Numerical data are obtained using the MHNC approximation. The circles, squares, and diamonds represent $|B|$, $B'' > 0$, and $(v - kT\chi)^2/2kT\chi > 0$, respectively. The dashed line is the linear fit of B'' vs. σ^* with a slope of 6 in the σ^* range from 7 to 16. The solid line is the linear fit of $|B|$ vs. σ^* with a slope of 7 in the same σ^* range.

Now we discuss the particle size dependence of each term in Eq. (4.3). Figure 4.7(b) clearly shows that B'' and $(v - kT\chi)^2/2kT\chi$ increase with increasing σ, and they are proportional to the 6th power of σ. The log-log plot of $|B|$ vs. σ^* in the σ^* range from 7 to 16 shows a nearly linear relationship. B is thus related to σ^* through the power-law relationship $B \propto \sigma^\alpha$, but the best estimate of exponent α is 7, not 6. Similar power law behavior was obtaind for the LJ particles in water based on the MD simulation.[65], [113] As shown in Figure 4.4(b), the relationship between the gas virial coefficient B_{gas} and the diameter σ is $B_{\text{gas}} \propto \sigma^\alpha$ with $\alpha = 3$, so $B \propto \sigma^\alpha$ with $\alpha = 7$ is characteristic in a solution, not in a vacuum. However, the power law behavior of B against σ does not match the σ dependence of B'' and $(v - kT\chi)^2/2kT\chi$.

Does the power law behavior $B \propto \sigma^\alpha$ with $\alpha = 7$ hold for much larger-size particles? Figure 4.8(a) is the MHNC result of B for hard-sphere particles with σ^* ranging from 1 to 50. This figure clearly shows that the power law behavior does not hold for $\sigma^* > 20$. The exponent α in $B \propto \sigma^\alpha$ should be greater than 7 for much larger particles.

The deviation from the power law behavior $B \propto \sigma^7$ is due to the σ dependence of B''. Figure 4.8(b) is a log-log plot of the "absolute values" of B'' against σ^*. For $\sigma^* \leq 30$, B'' is positive and increases with being proportional to the 6th power of σ. On the other hand, B'' decreases with increasing σ^* from 35 to 50, and for the particles with $\sigma^* =$ 45 and 50, it becomes negative. Since the second term in Eq. (4.3) is always negative, B could be a significantly negative value when B'' is negative, and so B deviates from $B \propto \sigma^\alpha$ with $\alpha = 7$.

However, $B'' < 0$ is physically strange because of Eq. (4.4): The negative B'' means that the solute excess chemical potential μ^* decreases with increasing the number of solutes at a fixed-volume system. Figure 4.8(b) also suggests that in the σ^* range from 35 to 50, the insertion of a solute particle into a fixed-volume system becomes easier as the particle size increases. The solvation free energy μ^* for hard-sphere particles is determined by a cavity creation of a particle with its diameter σ in a pure solvent, so the magnitude of B'' should increase with increasing σ. Therefore, the numerical results of B'' for $\sigma^* =$ 40, 45, and 50 might be incorrect.

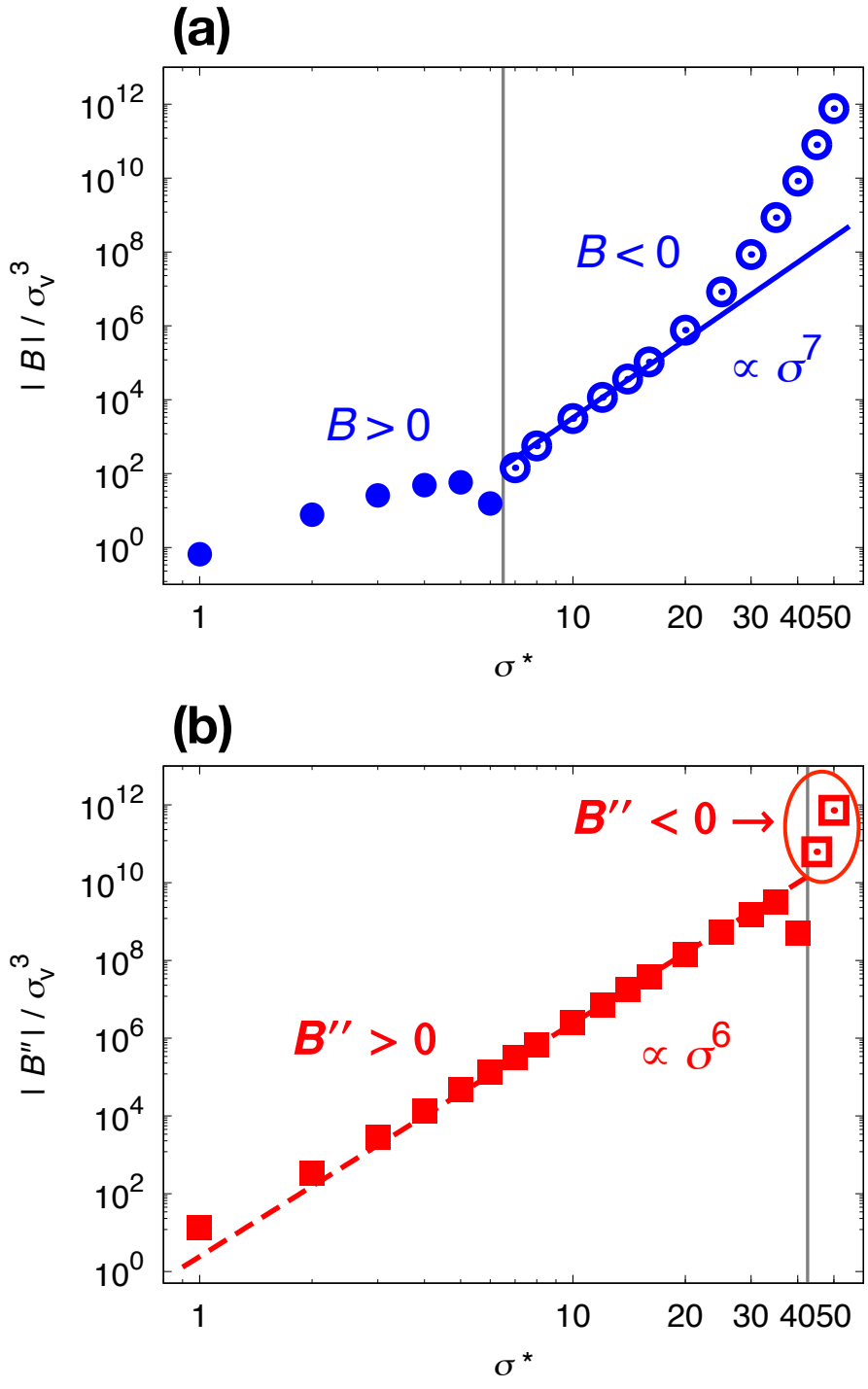

Figure 4.8: (a) The log-log plot of the absolute values of B against σ^* ranging from 1 to 50. Note that B is positive for $\sigma^* \leq 6$ while negative for $\sigma^* \geq 7$. The solid line is the linear fit of $|B|$ vs. σ^* with a slope of 7 in the σ^* range from 7 to 16. (b) The absolute values of B'' as a function of σ^*. Note that B'' is positive for $\sigma^* \leq 40$ while negative for $\sigma^* \geq 45$. The dashed line is the linear fit of B'' vs. σ^* with a slope of 6 in the σ^* range from 7 to 16.

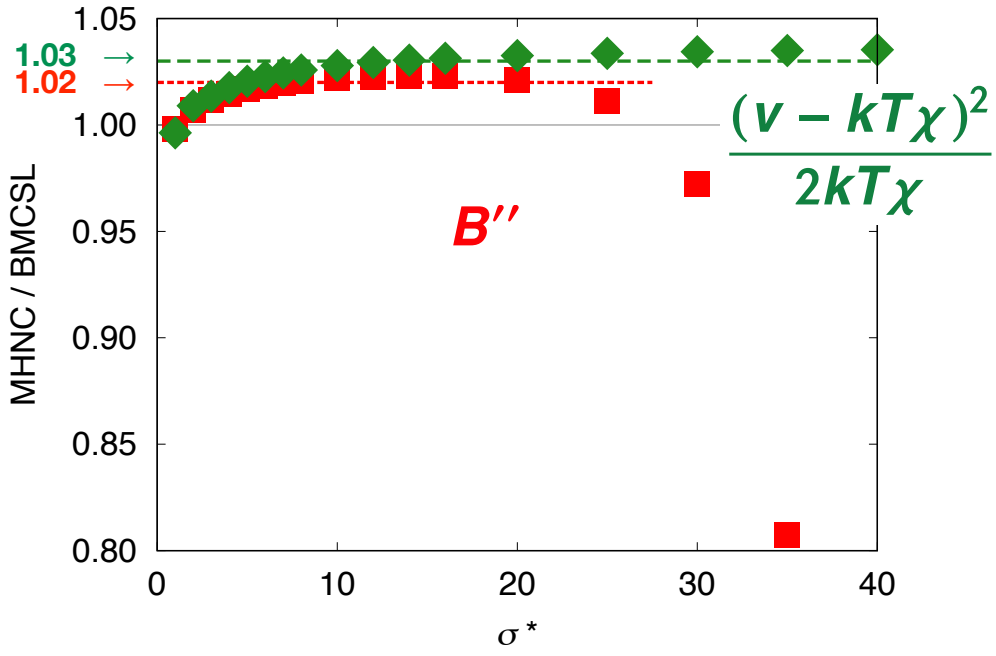

Figure 4.9: The ratio of the MHNC numerical result and the BMCSL analytical result as a function of σ^*. The squares and diamonds represent the ratios of two results for B'' and $(v - kT\chi)^2/2kT\chi$, respectively.

Figure 4.8(a) indicates that the MHNC result of B at $25 \leq \sigma^* \leq 35$ also deviates from the power law behavior $B \propto \sigma^\alpha$ with $\alpha = 7$. To examine this deviation, we take the ratio of the MHNC numerical result and the BMCSL analytical result. Figure 4.9 shows that the ratio of the MHNC and BMCSL results for $(v - kT\chi)^2/2kT\chi$ is nearly 1.03 at $10 \leq \sigma^* \leq 40$, so the MHNC result is about 3 % greater than the BMCSL result. In the σ^* range from 10 to 20, the MHNC result of B'' is about 2 % greater than the BMCSL result. However, the ratio deviates from 1.02 at $\sigma^* = 25$ and it rapidly decreases with increasing σ^* from 25 to 35. As shown in Figure 4.8(a), the deviation of B from the power law $B \propto \sigma^7$ begins at $\sigma^* = 25$. To check the reliability of the MHNC results for the hard-sphere particles with $\sigma^* \geq 25$, we need to compute B and B'' using other reliable approaches.

4.4 CONCLUSIONS

We studied the two-component hard-sphere system of a solute pair immersed in solvent particles to quantify the relationship between the inter-solute effecive pair interaction and the solute size. The strength of the effective interaction is quantified by the potential $w(r)$ of mean force and the osmotic second virial coefficient B. We evaluate $w(r)$ and B for hard-sphere particles of different diameters σ based on the integral equation theory, the Monte Carlo (MC) simulation, the Asakura-Oosawa (AO) theory,[12] and the Boubík-Mansoori-Carnahan-Starling-Leland (BMCSL) equation of state.[13], [14] The comparison with the MC results of $w(r)$ shows that the MHNC closure relation[11] is more suitable than the HNC closure to obtain the correct result derived from the integral equation theory.

Numerical and analytical results show that the first minimum $w(\sigma)$ of the effective potential descends with increasing σ. The decrease of $w(\sigma)$ against σ indicates that the contact pair of solute particles becomes more stable as the particle size increases due to the excluded volume effect.[12] The second (solvent-separated) minimum also decreases with σ, which is inconsistent with the simulation result of $w(r)$ for the Lennard-Jones particles in water:[65], [113] The solvent-separated state of two solute particles in a hard-sphere solvent becomes more stable with increasing σ, whereas this state in water is less stable as the particle size increases.

The numerical result derived from the integral equation theory shows that the osmotic B for small-size particles is positive and ascends with increasing σ. The increase of B is due to the repulsive pair potential between solute particles. For large-size solutes, B is negative and decreases with σ. In this case, the solute-solute effective interaction is attractive and becomes stronger as the solute size increases.

The log-log plot of B and σ indicates the power law behavior $B \propto \sigma^{\alpha}$. The BMCSL analytical expressions for the first and second terms in the thermodynamic identity Eq. (4.3) for B indicate that the exponent α in $B \propto \sigma^{\alpha}$ is 6. The MHNC numerical results of these two terms are in excellent agreement with the BMCSL analytical results with a relative error of a few percent. However, the best estimate of α obtained from the integral

equation theory is 7 in the σ range from $7\sigma_{\mathrm{v}}$ to $16\sigma_{\mathrm{v}}$, and $B \propto \sigma^7$ does not hold for larger σ. The deviation from the power law would be due to the suspicious size dependence of the first term B'' derived from the integral equation theory with the MHNC approximation. We would validate the numerical and analytical results for large solute particles using other reliable approaches, such as the event-chain Monte Carlo algorithms.[126]

Chapter 5

Microheterogeneity in Aqueous 1-Propanol Solutions due to the Hydrophobic Interaction

Abstract

1-Propanol and water are miscible over the entire concentration range at room temperature and pressure. However, numerous studies show that the concentration fluctuation of the aqueous 1-propanol solution becomes the most at low alcohol concentrations. Based on the molecular simulation, we clarify that the hydrophobic interaction between nonpolar groups of alcohol molecules is a significant factor in the microheterogeneity of the solutions at low mole fractions x_{P} of 1-propanol. Radial distribution functions indicate the concentration heterogeneity on nanometer-length scales in the aqueous solutions with low x_{P}. Cluster analysis shows that 1-propanol molecules form percolation clusters due to the hydrophobic interaction at $x_{\mathrm{P}} \geq 0.15$. Water molecules also form the hydrogen-bonding percolation cluster. We find that the percolation transitions by 1-propanol and water occur independently at $x_{\mathrm{P}} = 0.15$ and 0.5, respectively.

5.1 INTRODUCTION

Hydrophobic interactions are the effective interactions between nonpolar solutes, or nonpolar groups of amphipathic molecules, in aqueous solutions. These interactions are the driving forces for various self-assemblies of surfactants, such as micelles, vesicles, and lamellae, and play a role in the structural stability and function of proteins in vivo. Understanding the nature of hydrophobic interactions between molecules with apolar moieties is considerable not only for fundamental research but also for applied research.

Alcohol molecules have hydrophilic and hydrophobic parts. In aqueous solutions, these molecules form hydrogen bonds with water and other alcohol molecules through their hydroxyl group. They also interact with other alcohols via the hydrophobic interaction. Because of this amphipathicity, alcohol/water mixtures, which are simple two-component systems, have been studied over the years. Of particular interest are aqueous solutions of short-chain monohydric alcohols, such as methanol, ethanol, 1-propanol, 2-propanol, and *tert*-butyl alcohol: These alcohols are miscible with water over the entire concentration range at room temperature.

Several physical quantities of aqueous alcohol solutions exhibit anomalous concentration dependence. The Kirkwood-Buff integral,[7] which is related to the concentration fluctuation of solutions, reaches a maximum at low mole fractions of alcohol.[127]–[129] It is well-known that there is microheterogeneity in these mixtures, a microscale heterogeneous structure (not macroscopic phase separation) with associations of the same molecular species.

Numerous experimental studies have investigated the mixed states, concentration fluctuations, and microscopic structural changes of aqueous alcohol solutions based on the X-ray scattering,[127]–[131] Raman spectroscopy,[132] dielectric relaxation measurement,[133]–[136] ultrasonic wave,[137] terahertz time-domain spectroscopy,[138] thermodynamic measurements,[139]–[145] and theoretical calculations.[146]–[148] These investigations show that many physical quantities take maxima or minima at low alcohol concentrations. The dynamical properties,[149] microheterogeneity,[150]–[155] and clustering[156]–[162] of these mixtures are also examined based on the molecular simulation. Several studies have focused on

clustering and percolation in the aqueous solutions using both experiments and simulations.[163]–[169]

Molecular simulation studies show that alcohol molecules alone do not form percolation clusters by hydrogen bonding, and the percolation transition of water occurs at high concentrations of alcohol.[158]–[162], [164], [167]–[169] Although numerous studies focused on the hydrogen bonding, to our knowledge, there are only two investigations on clustering and percolation due to the hydrophobic interaction between alcohol molecules.[164], [165] The measurement of the isobaric heat capacity suggests that the hydrophobic moieties of amphiphiles would be the origin of the anomalous behavior of these aqueous solutions.[145], [170] The present paper aims to clarify the importance of hydrophobic interactions, especially at low alcohol concentrations.

We focus on the 1-propanol molecule because it has the longest carbon chain among miscible monohydric alcohols and so the hydrophobic interaction between these nonpolar parts could affect the properties of the aqueous solution. Experimental and theoretical studies have indicated that in the range of the mole fractions x_{P} of 1-propanol from 0.1 to 0.3, the concentration fluctuation of the 1-propanol/water mixture becomes the most, and the microscopic structure of this solution changes significantly.[128], [130]–[132], [135]–[145], [147]–[149] The molecular simulation study also clarifies the concentration heterogeneity on nanometer-length scales at $x_{\mathrm{P}} = 0.2$ and 0.3.[153] The percolation transition by water occurs at $x_{\mathrm{P}} = 0.4$, but 1-propanol molecules do not form the percolation cluster through hydrogen bonding at any concentration.[169] Here, we investigate the microheterogeneity in the 1-propanol/water mixture due to the hydrophobic interaction between alcohol molecules at low 1-propanol concentrations.

5.2 COMPUTATIONAL DETAILS

5.2.1 Molecular Dynamics Simulation

We performed isobaric-isothermal molecular dynamics (MD) simulations of the model systems to study the microheterogeneity in the aqueous 1-propanol solution. The TraPPE-

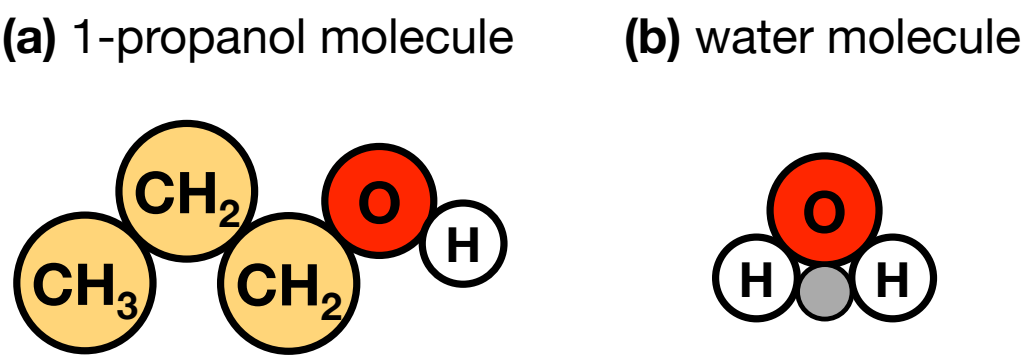

Figure 5.1: Molecular structures of (a) the TraPPE-UA model[171] for 1-propanol molecule and (b) the TIP4P/2005 model[53] for water molecule. A gray circle of water model is the dummy site.

UA[171] and TIP4P/2005[53] potential functions represent the intermolecular interactions between 1-propanol molecules and water molecules, respectively. Figure 5.1 shows the model structures of 1-propanol and water molecules. The intermolecular potentials of these models consist of the Lennard-Jones (LJ) and Coulomb potentials. The cutoff distance of the LJ potential is 1.4 nm, and the Lorentz-Berthelot rule gives the LJ parameters between different atoms. The long-range part of the Coulomb potential is corrected based on the particle mesh Ewald method with a real-space cutoff of 1.4 nm.

GROMACS 2018.3[56] was the software to perform the molecular simulations of the model aqueous solutions at the temperature $T = 293$ K and the pressure $p = 1$ bar. T and p were maintained by the Nosé-Hoover and Parrinello-Rahman methods, respectively. The mole fractions x_{P} of 1-propanol are 0, 0.1, 0.15, 0.2, 0.3, 0.4, 0.5, 0.6, and 1. The total number of 1-propanol and water molecules in each cubic cell is 16000, and we applied the three-dimensional periodic boundary condition to this cell. The duration time of the production run is 100 ns, and the time step interval of each simulation is 1 fs. The configurations of 1-propanol and water molecules were sampled every 0.5 ps to calculate the radial distribution functions between these molecules. For the cluster and percolation analyses, we used the trajectories that recorded the coordinates of all molecules every 10 ps.

Table 5.1 shows the numbers N_{P} and N_{W} of 1-propanol and water molecules, respec-

Table 5.1: The number N_{P} of 1-propanol molecules, the N_{W} of water molecules, the density ρ obtained from the simulation, and the experimental value[172] ρ_{exp} for the aqueous solutions of 1-propanol with different mole fractions x_{P}.

x_{P}	N_{P}	N_{W}	ρ / g cm^{-3}	ρ_{exp} / g cm^{-3}
0	0	16000	1.00238 ± 0.00002	0.99821
0.1	1600	14400	0.95368 ± 0.00014	0.95616
0.15	2400	13600	0.93146 ± 0.00013	-
0.2	3200	12800	0.91293 ± 0.00015	0.91803
0.3	4800	11200	0.88472 ± 0.00008	0.89051
0.4	6400	9600	0.86370 ± 0.00003	0.86976
0.5	8000	8000	0.84734 ± 0.00004	0.85383
0.6	9600	6400	0.83411 ± 0.00002	0.84071
1	16000	0	0.79694 ± 0.00002	0.80428

tively, the solution densities ρ obtained from the simulation, and the reference values ρ_{exp}.[172] For each aqueous solution, the simulation result of ρ is in good agreement with ρ_{exp}: The relative errors between ρ and ρ_{exp} are less than 1 %. Therefore, the model potential functions[53], [171] used in the present study can well reproduce the density of aqueous 1-propanol solutions and its concentration dependence at room temperature and pressure.

5.2.2 Cluster Analysis

We analyze the clustering due to the hydrophobic interaction between the carbon chains of 1-propanol molecules following the previous study for the micellization of sodium hexyl sulfate:[173] Two 1-propanol molecules form the same cluster if the distance between any one of the nine pairs of carbon atoms is less than or equal to 0.4 nm. We also examine the hydrogen-bonding cluster of water molecules: Two water molecules are hydrogen-bonded if the distance between their oxygen atoms is less than 0.35 nm and the angle between the hydrogen and two oxygen atoms is less than or equal to 30 degrees.[101]–[103]

Based on these definitions of clustering, we calculate the number distribution $n_i(s)$ of

clusters[174] for the aqueous 1-propanol solutions with $x_{\mathrm{P}} = 0.1$, 0.15, 0.2, 0.3, 0.4, 0.5, and 0.6:

$$n_i(s) = \frac{\langle N_{\mathrm{cluster}}(s) \rangle}{N_i}, \tag{5.1}$$

where s is the number of molecules constituting one cluster, N_i is the total number of molecules of species i, and $N_{\mathrm{cluster}}(s)$ is the number of clusters of size s in each configuration. $\langle \cdots \rangle$ denotes the time average.

In the present work, the number distribution of clusters in the 1-propanol/water mixture is compared with that in the hypothetical two-component system to reveal the specific nature of clustering in the aqueous solution. The hypothetical system assumes that some molecules in pure water ($x_{\mathrm{P}} = 0$) or pure 1-propanol ($x_{\mathrm{P}} = 1$) are molecule α, and the remaining molecules are molecule β. For example, if 1600 molecules in pure 1-propanol are considered molecule α and the remaining 14400 molecules are molecule β, we can regard this system as the hypothetical two-component system with the mole fraction $x_{\alpha[\mathrm{P}]}$ of molecule α being 0.1.

We denote $n_{\mathrm{P}}(s)$ as the number distribution of clusters of 1-propanol molecules in aqueous 1-propanol solutions and $n_{\alpha[\mathrm{P}]}(s)$ as that of molecule α in pure 1-propanol. The comparison of $n_{\mathrm{P}}(s)$ and $n_{\alpha[\mathrm{P}]}(s)$ is for the systems with $x_{\mathrm{P}} = x_{\alpha[\mathrm{P}]} = 0.1$, 0.15, 0.2, 0.3, 0.4, 0.5, and 0.6. Similarly, $n_{\mathrm{W}}(s)$ is the number distribution of clusters of water molecules in the aqueous systems, and $n_{\alpha[\mathrm{W}]}(s)$ is that of molecule α in pure water. We compare $n_{\mathrm{W}}(s)$ and $n_{\alpha[\mathrm{W}]}(s)$ at $x_{\mathrm{W}} = x_{\alpha[\mathrm{W}]} = 0.4$, 0.5, 0.6, 0.7, 0.8, 0.85, and 0.9, where $x_{\mathrm{W}} = 1 - x_{\mathrm{P}}$ is the mole fraction of water in the solution and $x_{\alpha[\mathrm{W}]}$ is that of molecule α in the hypothetical system.

5.2.3 Percolation Analysis

There are numerous studies of percolation in lattice,[174], [175] simple liquids,[176]–[182] and aqueous solutions.[158]–[161], [164], [165], [167]–[169], [183]–[186] They determined the density or concentration of the percolation transition based on the $n_i(s)$, the percolation probability, and the fractal dimension. Critical exponents have also been obtained for several systems to confirm the scaling rule for the percolation transition.[174]

To determine the concentration of the percolation transition, we calculate the percolation probability P, the probability that a cluster percolates in a three-dimensional direction. First, we identify the largest-size cluster in each equilibrium configuration. Next, we assume the system whose volume is eight times larger (twice the length of each side) than the original cubic cell by placing seven copies of that cell, and again, we identify the largest-size cluster in this system. If the size s of the largest cluster in the copy system is eight times larger than s of the largest cluster in the original system, P is equal to 1, and otherwise, $P = 0$. We obtain the time-averaged values $\langle P \rangle$ of the probability P as a function of the concentration and compare them for the aqueous 1-propanol solution and the hypothetical two-component system.

5.3 RESULTS AND DISCUSSION

Figure 5.2 shows the snapshots of aqueous 1-propanol solutions of three different concentrations. Note that these snapshots are only one of the equilibrium configurations in the 100 ns production run. One can see the microheterogeneity of these solutions: 1-Propanol molecules aggregate locally, even though the number of those molecules is less than that of water molecules. Figure 5.2(a) suggests that at the 1-propanol mole fraction $x_{\mathrm{P}} = 0.1$, alcohol molecules form some medium-sized clusters. On the other hand, Figures 5.2(b) and (c) indicate that one large cluster is in each aqueous solution with $x_{\mathrm{P}} = 0.2$ and 0.3. Especially at $x_{\mathrm{P}} = 0.3$, this large cluster expands like a network. These mole fractions are in agreement with the concentration range where the mixed state of aqueous 1-propanol solutions changes significantly.[128], [130]–[132], [135]–[145], [147]–[149]

Now we examine the radial distribution functions $g_{ij}(r)$ for pairs of atoms i and j of 1-propanol or water molecules in the aqueous 1-propanol solutions. The 1-propanol concentrations x_{P} are 0, 0.1, 0.15, 0.2, 0.3, 0.4, 0.5, 0.6, and 1.

Figure 5.3(a) displays $g_{\mathrm{CC}}(r)$ for pairs of terminal carbon atoms of 1-propanol molecules. One can see that $g_{\mathrm{CC}}(r)$ has a broad peak with a maximum at $r \approx 0.4$ nm, and the height of this peak decreases with increasing x_{P}. Figure 5.3(b) shows that $g_{\mathrm{PP}}(r)$ for pairs of oxygen atoms of 1-propanol molecules has a sharp peak at $r \approx 0.27$ nm. This peak

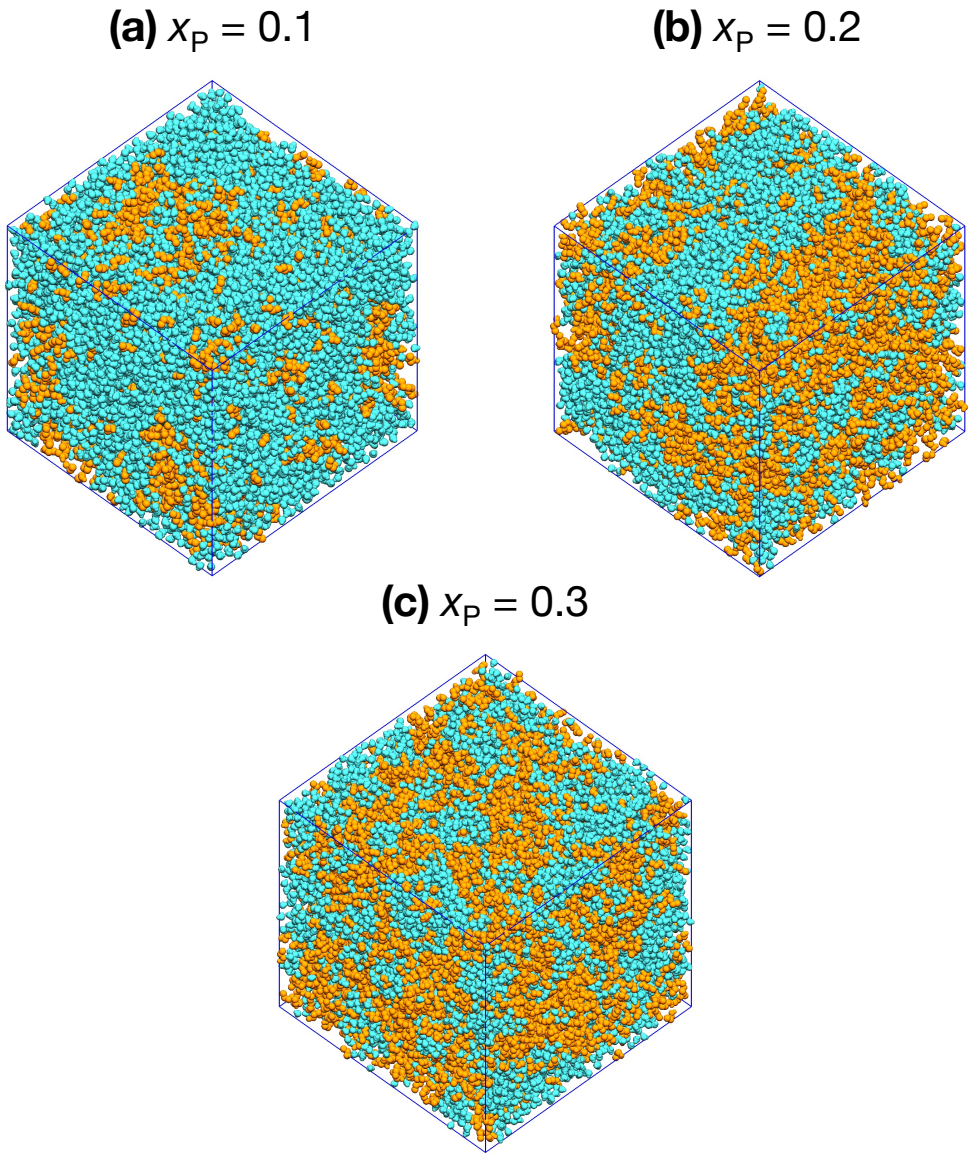

Figure 5.2: Snapshots of aqueous 1-propanol solutions at 1-propanol mole fractions x_P = (a) 0.1, (b) 0.2, and (c) 0.3. 1-Propanol and water molecules are shown in orange and blue, respectively. Each snapshot is the final configuration of the 100 ns production run.

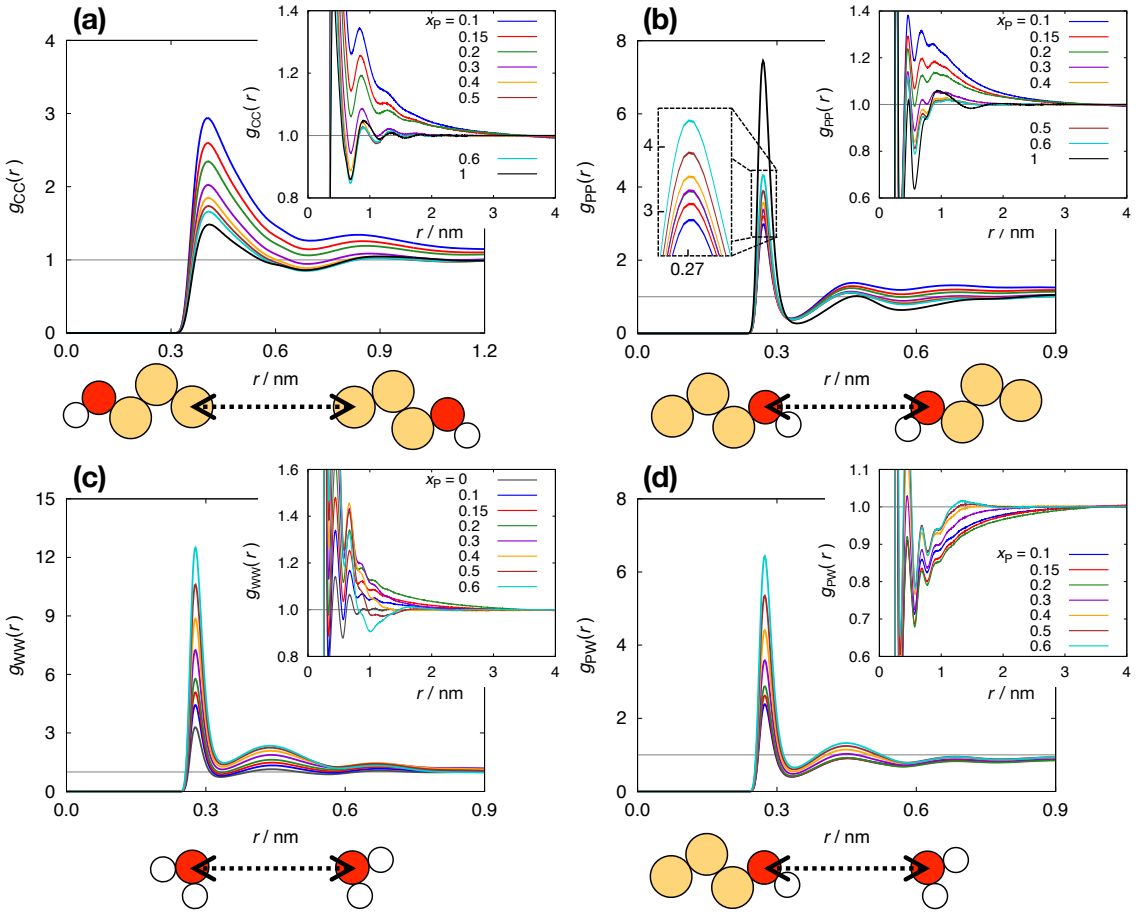

Figure 5.3: Radial distribution functions $g_{ij}(r)$ for pairs of (a) terminal carbon atoms of 1-propanol, (b) oxygen atoms of 1-propanol, (c) oxygen atoms of water, and (d) oxygen atoms of 1-propanol and water molecules in the aqueous 1-propanol solutions. Each curve represents the result at $x_{\mathrm{P}} = 0$ (dark gray), 0.1 (blue), 0.15 (red), 0.2 (green), 0.3 (violet), 0.4 (orange), 0.5 (brown), 0.6 (light blue), or 1 (black). The inset in the upper right of each figure is the enlarged view of $g_{ij}(r)$ at long distances r.

is slightly higher with increasing x_P, so the concentration dependence of the first peak height of $g_{PP}(r)$ is opposite to that of $g_{CC}(r)$. These results suggest that at lower x_P, the hydrophobic interaction between the nonpolar groups of 1-propanol molecules becomes more attractive, while the hydrogen bond between the hydroxyl groups of 1-propanol is less likely to be formed.

Figure 5.3(c) shows $g_{WW}(r)$ for pairs of oxygen atoms of water molecules. The sharp peak of $g_{WW}(r)$ at $r \approx 0.27$ nm increases with increasing x_P. Similar x_P dependence is also obtained from $g_{PW}(r)$ for pairs of oxygen atoms of 1-propanol and water molecules, as shown in Figure 5.3(d). Both results indicate that the hydrogen bonds between water-water and 1-propanol-water molecules are likely to be formed with increasing alcohol concentration.

The upper-right insets of Figures 5.3(a), (b), (c), and (d) are the enlarged views to examine the long-range behavior of $g_{ij}(r)$. In the aqueous solutions with $x_P = 0.1$, 0.15, and 0.2, the distribution functions deviate from 1 even at $r = 2 \sim 3$ nm,, suggesting the concentration heterogeneity on nanometer-length scales. Perera obtained similar results at $x_P = 0.2$ and 0.3 performing the molecular simulation of massive systems with the total number of molecules being 128000.[153] Note again that $x_P = 0.1$, 0.15, and 0.2 are in the concentration range where the mixed state of the aqueous 1-propanol solution changes significantly.

In the r range from 0.4 to 3 nm, $g_{CC}(r)$ and $g_{PP}(r)$ are greater than 1 in the aqueous solutions with $x_P = 0.1$, 0.15, and 0.2. The positive deviation from 1 at large distances is the most at $x_P = 0.1$ and decrease with increasing x_P from 0.1 to 0.4. The inset in Figure 5.3(c) also shows that in the long range of r, the positive deviation of $g_{WW}(r)$ from 1 increases with increasing x_P up to 0.2, but it decreases with x_P from 0.2 to 0.4. In contrast, $g_{PW}(r)$ is less than 1 in the r range from 0.3 to 3 nm at $x_P = 0.1$, 0.15, and 0.2. The magnitude of this negative deviation is the most at $x_P = 0.2$.

The concentration dependence of the deviations of $g_{ij}(r)$ from 1 is qualitatively consistent with the x_P dependence of the Kirkwood-Buff (KB) integrals,[7] $G_{ij} = \int [g_{ij}(r) - 1] d\tau$ with $d\tau$ being the infinitesimal volume element, for aqueous 1-propanol solutions:[128] The

propanol-propanol KB integral G_{PP} is positive in the x_{P} range from 0.05 to 0.3 and takes a maximum at about $x_{\mathrm{P}} = 0.15$. The water-water KB integral G_{WW} is also positive and increases with increasing x_{P} from 0.05 to 0.25, but it decreases as x_{P} increases from 0.25 to 0.91. On the other hand, the propanol-water KB integral G_{PW} is negative, and that magnitude is the largest in between $x_{\mathrm{P}} = 0.15$ and 0.2.

In summary, we find a nanometer-scale concentration heterogeneity in the aqueous 1-propanol solutions with $x_{\mathrm{P}} = 0.1$, 0.15, and 0.2. Figures 5.3(a) and (b) show the opposite trends for the x_{P} dependence of the first peak heights of $g_{\mathrm{CC}}(r)$ and $g_{\mathrm{PP}}(r)$: The former ascends while the latter descends with decreasing x_{P}. This result suggests that, especially at lower x_{P}, the hydrophobic interaction between the hydrophobic groups of 1-propanol molecules has a greater effect on the microscopic structures of the aqueous solution than the hydrogen bond between the hydroxyl groups.

The next subject is the clustering due to the hydrophobic interaction between 1-propanol molecules. Figure 5.4(a) shows the number distributions $n_{\mathrm{P}}(s)$ of clusters due to the hydrophobic interaction between the carbon chains of 1-propanol molecules in the aqueous solutions. The $n_{\mathrm{P}}(s)$ of medium-sized clusters with $s < 1000$ decreases as the concentration x_{P} increases. In contrast, $n_{\mathrm{P}}(s)$ has a peak at $s > 1000$ except for the result of $x_{\mathrm{P}} = 0.1$: The peak position is around $s = 1700$, 2600, 4300, 6000, 7600, and 9200 at $x_{\mathrm{P}} = 0.15$, 0.2, 0.3, 0.4, 0.5, and 0.6, respectively. The total number N_{P} of 1-propanol molecules in the solution is 2400, 3200, 4800, 6400, 8000, and 9600 at $x_{\mathrm{P}} = 0.15$, 0.2, 0.3, 0.4, 0.5, and 0.6, respectively. Therefore, more than 70 % of 1-propanol molecules in the aqueous solutions form one cluster. This cluster would be the percolation cluster, and Figure 5.4(a) suggests that the percolation transition might occur at around $x_{\mathrm{P}} = 0.15$.

We compare $n_{\mathrm{P}}(s)$ for the aqueous solution with the number distribution $n_{\alpha[\mathrm{P}]}(s)$ for the hypothetical two-component system. The clustering in the hypothetical system is due to the effective interaction between molecule α in pure 1-propanol. Even at the same mole fractions x_{P} and $x_{\alpha[\mathrm{P}]}$, the plots of $n_{\mathrm{P}}(s)$ and $n_{\alpha[\mathrm{P}]}(s)$ as a function of cluster size s are very different. Figure 5.4(b) shows that there are no distributions of the clusters whose s is more than 1000, except at $x_{\alpha[\mathrm{P}]} = 0.5$ and 0.6. The $n_{\alpha[\mathrm{P}]}(s)$ has a peak only for $x_{\alpha[\mathrm{P}]} = 0.6$,

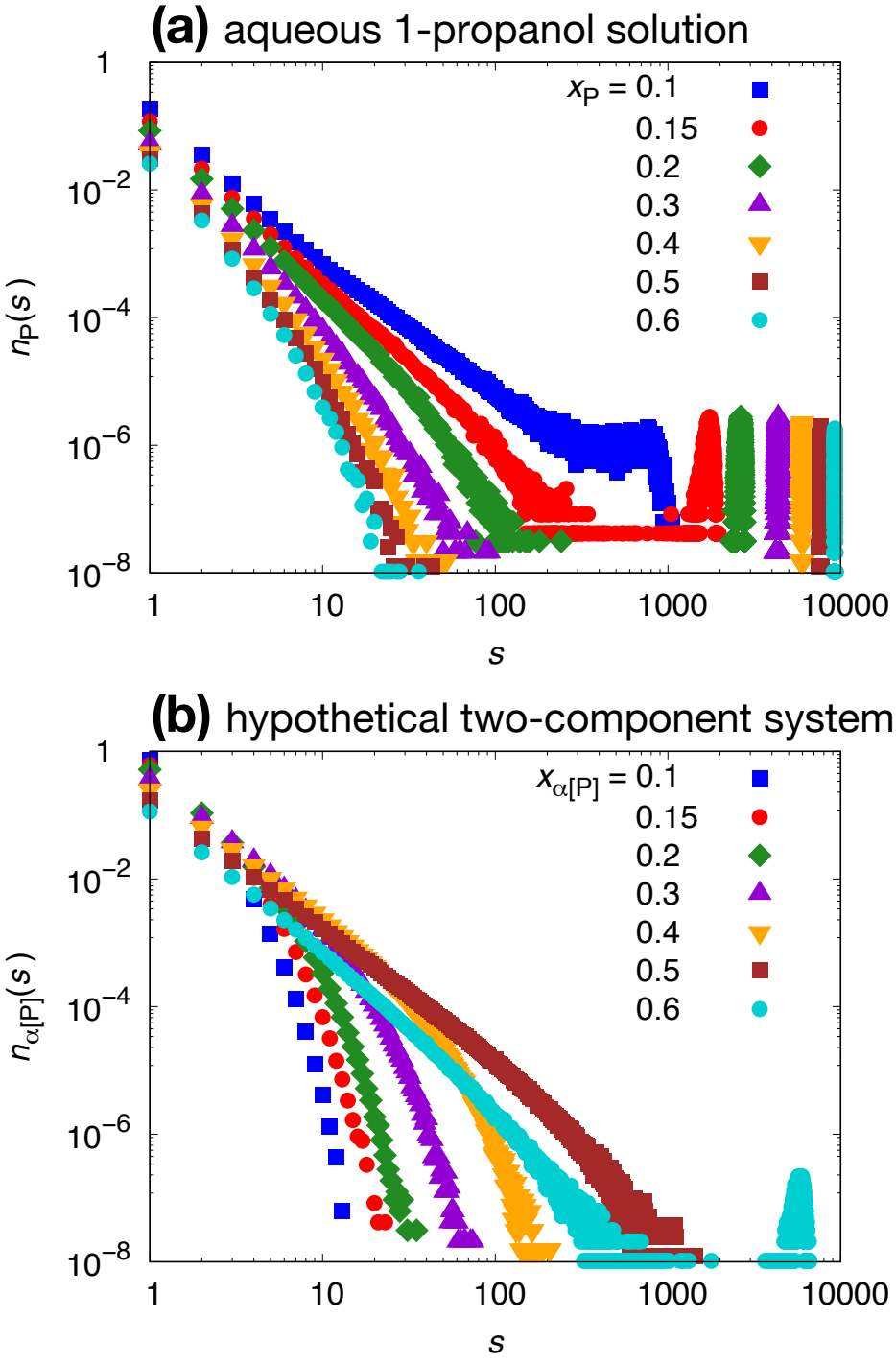

Figure 5.4: (a) The number distributions $n_{\mathrm{P}}(s)$ of clusters of 1-propanol molecules in aqueous 1-propanol solutions. Each plot represents the result at $x_{\mathrm{P}} = 0.1$ (blue square), 0.15 (red circle), 0.2 (green diamond), 0.3 (violet triangle), 0.4 (orange inverted triangle), 0.5 (brown square), or 0.6 (light blue circle). (b) The number distributions $n_{\alpha[\mathrm{P}]}(s)$ of clusters of molecule α in pure 1-propanol. The mole fractions $x_{\alpha[\mathrm{P}]}$ of molecule α are the same as x_{P} of the aqueous solutions.

indicating that in the concentration range of $x_{\alpha[\mathrm{P}]}$ from 0.1 to 0.5, clusters of molecule α do not percolate. Therefore, $x_{\mathrm{P}} = 0.15$, at which 1-propanol molecules in the aqueous solution begin to form the percolation cluster, is a significantly lower concentration than in the hypothetical system.

Now we examine the clustering due to the hydrogen bonding between water molecules. Figure 5.5(a) displays the number distributions $n_{\mathrm{W}}(s)$ of clusters of water molecules in the aqueous 1-propanol solution. One can see that $n_{\mathrm{W}}(s)$ of small-sized clusters with s less than 100 increases with decreasing the mole fraction x_{W} of water. In the s range more than 1000, $n_{\mathrm{W}}(s)$ has a peak at each concentration except for the results of $x_{\mathrm{W}} = 0.5$ and 0.4: The peak position is around $s = 14400$, 13500, 12700, 10900, and 8800 at $x_{\mathrm{W}} = 0.9$, 0.85, 0.8, 0.7, and 0.6, respectively. The total number N_{W} of water molecules is 14400, 13600, 12800, 11200, and 9600, so $90 \sim 100$ % of water molecules in the aqueous solutions form a percolation cluster. Pethes et al. have already found these peaks for the systems consisting of totally 4000 molecules.[169]

The comparison of $n_{\mathrm{W}}(s)$ for the aqueous solution and $n_{\alpha[\mathrm{W}]}(s)$ of clusters of molecule α in pure water shows that they are similar to each other. This result is significantly different from the comparison of $n_{\mathrm{P}}(s)$ and $n_{\alpha[\mathrm{P}]}(s)$ due to the clustering of 1-propanol molecules. Figure 5.5(b) indicates that the number distribution $n_{\alpha[\mathrm{W}]}(s)$ of small-sized clusters increases with decreasing the mole fraction $x_{\alpha[\mathrm{W}]}$ of molecule α. The peak position of $n_{\alpha[\mathrm{W}]}(s)$ is around $s = 14400$, 13500, 12700, 10900, 8700, and 5300 at $x_{\alpha[\mathrm{W}]} = 0.9$, 0.85, 0.8, 0.7, 0.6, and 0.5, respectively.

The cluster analysis based on the number distribution $n_i(s)$ of clusters of size s clarifies a specific nature of clustering due to the hydrophobic interaction between the hydrophobic groups of 1-propanol molecules. In the aqueous solution, more than 70 % of 1-propanol molecules form a percolation cluster at $0.15 \leq x_{\mathrm{P}} \leq 0.6$, this concentration range is significantly lower than in the hypothetical two-component system. On the other hand, the number distributions of the hydrogen-bonding clusters of water molecules are not much different in the aqueous solution and the hypothetical system.

Next, we identify the concentration of the percolation transition based on the percola-

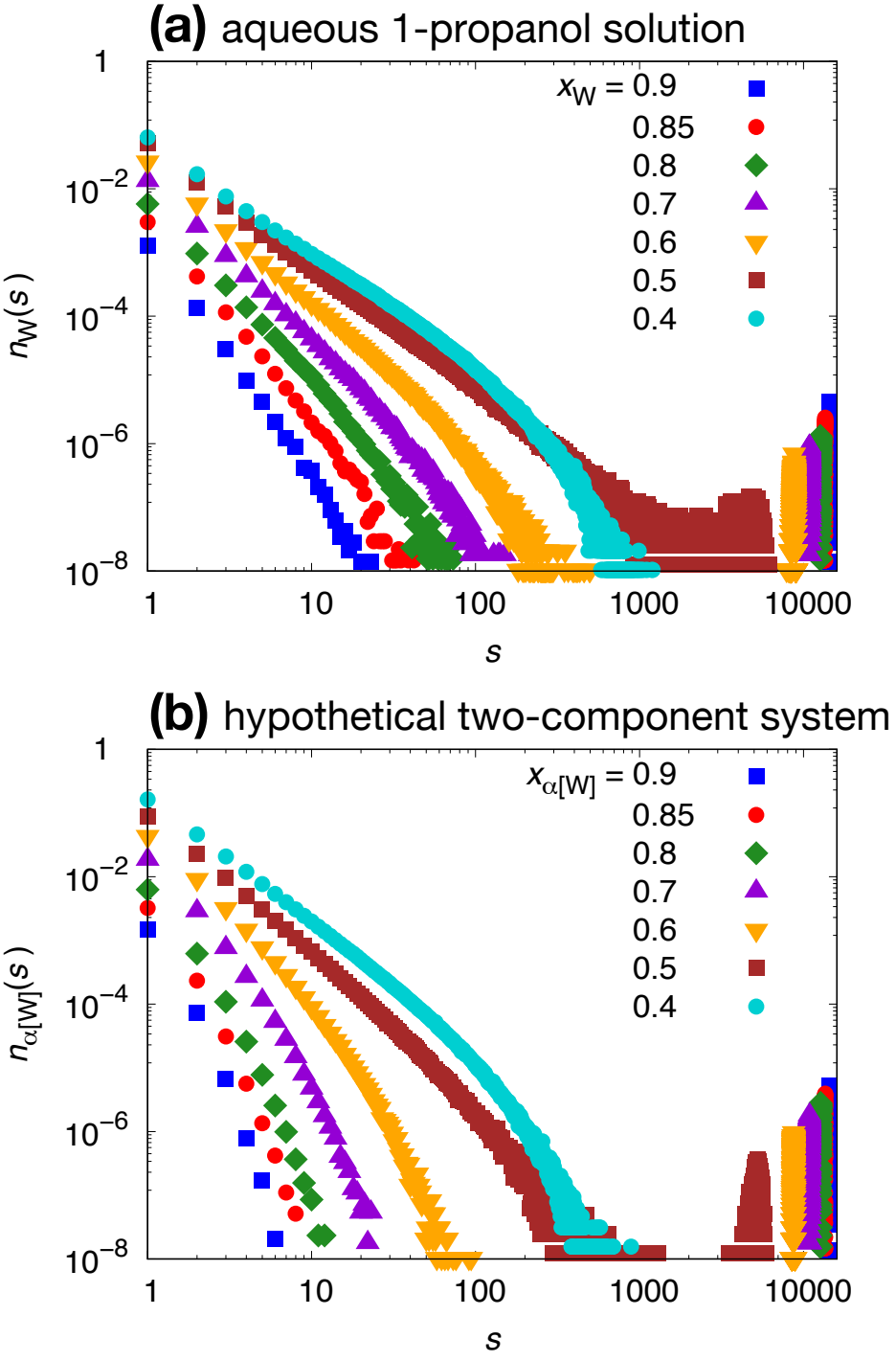

Figure 5.5: (a) The number distributions $n_{\mathrm{W}}(s)$ of clusters of water molecules in aqueous 1-propanol solutions. Each plot represents the result at the mole fraction of water, $x_{\mathrm{W}}(= 1-x_{\mathrm{P}}) = 0.9$ (blue square), 0.85 (red circle), 0.8 (green diamond), 0.7 (violet triangle), 0.6 (orange inverted triangle), 0.5 (brown square), or 0.4 (light blue circle). (b) The number distributions $n_{\alpha[\mathrm{W}]}(s)$ of clusters of molecule α in pure water. The mole fractions $x_{\alpha[\mathrm{W}]}$ of molecule α are the same as x_{W} of the aqueous solutions.

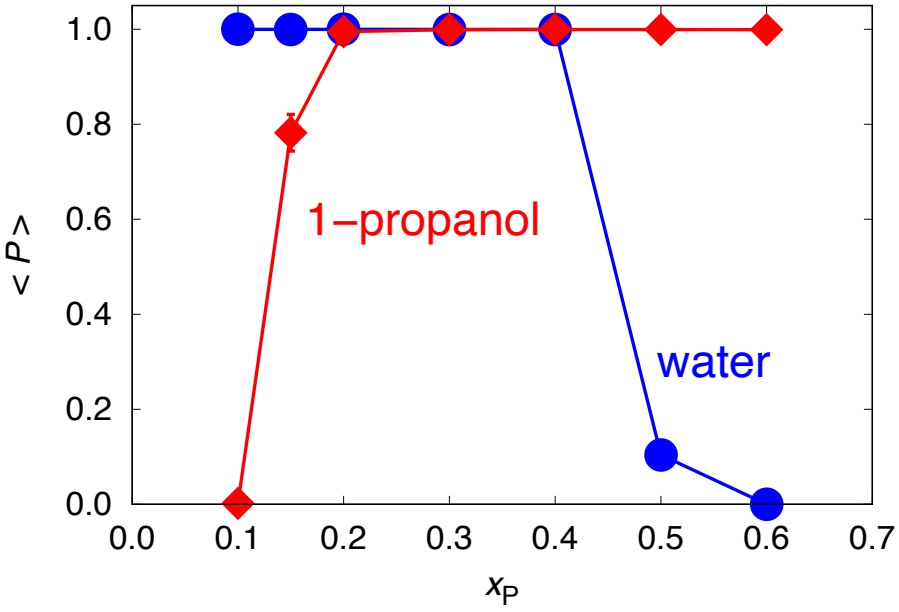

Figure 5.6: Percolation probability $\langle P \rangle$ of the max-sized cluster in the aqueous 1-propanol solution as a function of x_{P}. Red diamonds and blue circles represent $\langle P \rangle$ for the clustering of 1-propanol and water molecules, respectively.

tion probability P. Figure 5.6 is a plot of the time-averaged value $\langle P \rangle$ of the probability P for the clusters of 1-propanol and water as a function of x_{P}. This figure shows that the percolation transitions of 1-propanol and water occur at $x_{\mathrm{P}} = 0.15$ and 0.5, respectively. Especially in the x_{P} range from 0.15 to 0.5, 1-propanol and water molecules form separate percolation clusters.

Dougan et al. have already clarified similar behavior in the aqueous methanol solution:[164] Methanol and water molecules form independent percolating networks in the aqueous solution with the mole fraction x_{M} of methanol from 0.27 to 0.54. We compare the mole fractions at which alcohol molecules begin to form a percolation cluster. $x_{\mathrm{P}} = 0.15$ for the aqueous 1-propanol solutions is lower than $x_{\mathrm{M}} = 0.27$ for the aqueous methanol solution. Therefore, the percolation transition due to the hydrophobic interaction between alcohol molecules would occur at lower concentrations as the carbon chain length increases.

Here, the concentration dependence of $\langle P \rangle$ for the aqueous 1-propanol solution is compared with that for the hypothetical two-component system. We examine the mole

and volume fraction dependencies of $\langle P \rangle$: The comparison based only on the mole fraction x_i is not enough because the size of a 1-propanol molecule is a few times larger than that of a water molecule. In the case of the hypothetical two-component system, the volume fraction of molecule α is the same as the mole fraction.

The volume fraction ϕ_i of component i is defined as

$$\phi_i = \frac{n_i \bar{V}_i}{V}, \tag{5.2}$$

where n_i and $\bar{V}_i$ are the amount of substance and the partial molar volume of component i, respectively, and $V = \sum_i n_i \bar{V}_i$ is the total volume of a solution. In the case of binary solutions of components 1 and 2, the partial molar volumes $\bar{V}_1$ and $\bar{V}_2$ can be expressed by[187]

$$\bar{V}_1 = \frac{M_1}{\rho(x_2)} \left[1 + \frac{x_2(M_2 - M_1) + M_1}{M_1} \, \frac{x_2}{\rho(x_2)} \, \frac{\mathrm{d}\rho(x_2)}{\mathrm{d}x_2} \right] \tag{5.3}$$

and

$$\bar{V}_2 = \frac{M_2}{\rho(x_2)} \left[1 - \frac{x_2(M_2 - M_1) + M_1}{M_2} \, \frac{1 - x_2}{\rho(x_2)} \, \frac{\mathrm{d}\rho(x_2)}{\mathrm{d}x_2} \right]. \tag{5.4}$$

In Eqs. (5.3) and (5.4), M_i is the molar mass of component i, and $\rho(x_2)$ is the density of a solution as a function of the mole fraction x_2 of component 2.

Now we consider that component 1 is water and component 2 is 1-propanol. The expression $\rho(x_\mathrm{P})$ for the density of the aqueous 1-propanol solution as a function of x_P at 293 K is[187]

$$\rho(x_\mathrm{P}) = -0.01387 x_\mathrm{P}^4 - 0.17163 x_\mathrm{P}^3 + 0.47518 x_\mathrm{P}^2 - 0.48503 x_\mathrm{P} + 0.99823. \tag{5.5}$$

The numerical data of ρ obtained from the MD simulation are in excellent agreement with the experimental values[172] (see Table 5.1), so we use Eq. (5.5) to calculate the volume fractions ϕ_P and $\phi_\mathrm{W} = 1 - \phi_\mathrm{P}$ of 1-propanol and water, respectively.

Table 5.2 shows ϕ_P and ϕ_W for the aqueous solutions with $x_\mathrm{P} = 0.1$, 0.15, 0.2, 0.3, 0.4, 0.5, and 0.6. One can see that the values of mole and volome fractions are very different. For example, $\phi_\mathrm{P} \simeq \phi_\mathrm{W}$ when $x_\mathrm{P} = 0.2$ and $x_\mathrm{W} = 0.8$. Therefore, the volume

Table 5.2: The volume fractions $\phi_{\rm P}$ and $\phi_{\rm W}$ of 1-propanol and water, respectively, for the aqueous 1-propanol solutions with $x_{\rm P} = 0.1$, 0.15, 0.2, 0.3, 0.4, 0.5, and 0.6. $\phi_{\rm P}$ and $\phi_{\rm W}$ are obtained from Eq (5.2) coupled with Eqs. (5.3)-(5.5).

$x_{\rm P}$	0.1	0.15	0.2	0.3	0.4	0.5	0.6
$x_{\rm W}$	0.9	0.85	0.8	0.7	0.6	0.5	0.4
$\phi_{\rm P}$	0.31	0.42	0.51	0.65	0.74	0.81	0.87
$\phi_{\rm W}$	0.69	0.58	0.49	0.35	0.26	0.19	0.13

that 1-propanol and water occupy independently in the mixture is the same when the ratio of the numbers of 1-propanol and water molecules is about 1:4.

We show the x_i and ϕ_i dependence of the percolation probability $\langle P \rangle$ for the aqueous 1-propanol solution and the hypothetical two-component systems in Figure 5.7. First, Figure 5.7(a) indicates that 1-propanol molecules in the aqueous solution begin to form the percolation cluster at around $x_{\rm P} = 0.15$ or $\phi_{\rm P} = 0.42$. For the clustering of molecule α in pure 1-propanol, $\langle P \rangle$ rapidly changes at around the concentration $x_{\alpha[\rm P]} = \phi_{\alpha[\rm P]} = 0.58$. These results clarify that the percolation transition due to the hydrophobic interaction between 1-propanol molecules occurs at lower concentrations for either $x_{\rm P}$ or $\phi_{\rm P}$ than in the hypothetical system.

Next, Figure 5.7(b) displays that water molecules in the mixture begin to form the percolation cluster at around $x_{\rm W} = 0.5$ or $\phi_{\rm W} = 0.19$. The percolation transition due to the hydrogen bonding between molecule α in pure water occurs at around the fraction $x_{\alpha[\rm W]} = \phi_{\alpha[\rm W]} = 0.48$. These results indicate that the percolation transition of water in the solution occurs at nearly the same mole fraction in the hypothetical system. In contrast, the comparison of the volume fraction dependence of $\langle P \rangle$ clarifies that the percolation transition of water in the 1-propanol/water mixture occurs at much lower concentration.

The percolation transition in the aqueous 1-propanol solution would be related to the macrosopic and microscopic properties of this solution. Figure 5.6 suggests that $x_{\rm P} = 0.15$ is the concentration of the percolation transition due to the hydrophobic interaction between 1-propanol molecules. This mole fraction is in the concentration range where many physical quantities take maximum or minimum as a function of $x_{\rm P}$, the concentration fluc-

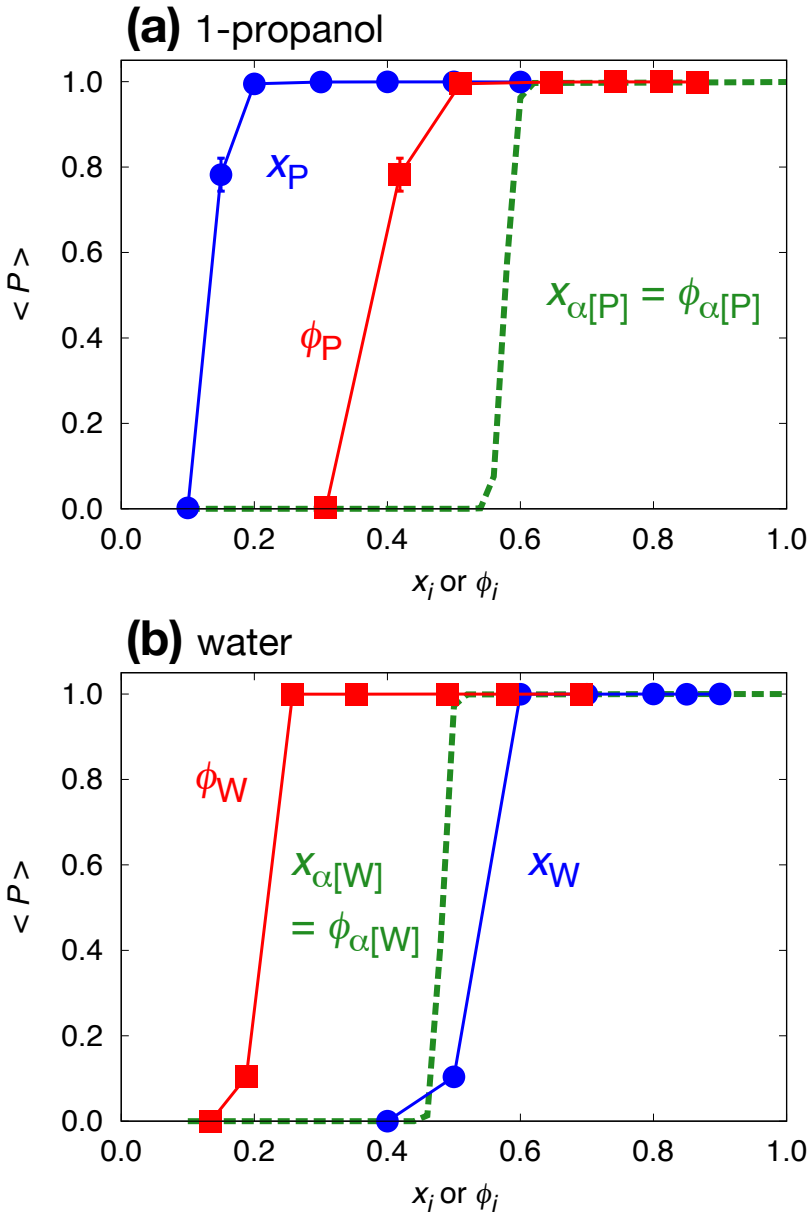

Figure 5.7: Concentration dependence of the percolation probabilities $\langle P \rangle$ for (a) 1-propanol and (b) water. (a) Blue circles and red squares represent $\langle P \rangle$ in the aqueous 1-propanol solution as a function of the mole fraction x_{P} and the volume fraction ϕ_{P}, respectively. The green dashed line is the result of $\langle P \rangle$ in the hypothetical two-component system as a function of the mole fraction $x_{\alpha[\mathrm{P}]}$ of molecule α. In the case of the hypothetical system, $x_{\alpha[\mathrm{P}]}$ is equal to the volume fraction $\phi_{\alpha[\mathrm{P}]}$. (b) Blue circles and red squares represent $\langle P \rangle$ of the clusters of water molecules in the solution as a function of x_{W} and ϕ_{W}, respectively. The green dashed line shows $\langle P \rangle$ of clusters of molecule α in the hypothetical system against the fraction $x_{\alpha[\mathrm{W}]} = \phi_{\alpha[\mathrm{W}]}$.

tuation is the most, and the mixed state changes significantly.[128], [130]–[132], [135]–[145], [147]–[149] At the same concentration, the radial distribution functions deviate from 1 even at long distances (see Figure 5.3). The experimental study also shows that $x_{\mathrm{P}} = 0.14$ and 0.45 are singular points for the x_{P} dependence of the dielectric relaxation time of the aqueous solution.[135] These concentrations are very close to the mole fractions of the percolation transitions of 1-propanol ($x_{\mathrm{P}} = 0.15$) and water ($x_{\mathrm{P}} = 0.5$), respectively.

Finally, we study the excess density $\rho_{\mathrm{ex}}(x_{\mathrm{P}})$ defined by the mole fraction x_{P}, and the $\rho_{\mathrm{ex}}(\phi_{\mathrm{P}})$ defined by the volume fraction ϕ_{P} as

$$\rho_{\mathrm{ex}}(x_{\mathrm{P}}) \equiv \rho - \left[x_{\mathrm{P}}\rho_{\mathrm{P}} + (1 - x_{\mathrm{P}})\rho_{\mathrm{W}}\right] \tag{5.6}$$

and

$$\rho_{\mathrm{ex}}(\phi_{\mathrm{P}}) \equiv \rho - \left[\phi_{\mathrm{P}}\rho_{\mathrm{P}} + (1 - \phi_{\mathrm{P}})\rho_{\mathrm{W}}\right]. \tag{5.7}$$

In Eqs. (5.6) and (5.7), ρ, ρ_{P}, and ρ_{W} are the densities of the aqueous 1-propanol solution, pure 1-propanol ($x_{\mathrm{P}} = 1$), and pure water ($x_{\mathrm{P}} = 0$), respectively.

Figure 5.8(a) shows three results of $\rho_{\mathrm{ex}}(x_{\mathrm{P}})$ obtained from the MD simulation, experimental values,[172] and Eq. (5.5) as a function of the mole fraction. One can see that $\rho_{\mathrm{ex}}(x_{\mathrm{P}})$ is negative and takes a minimum at around $x_{\mathrm{P}} = 0.4$. The concentration reaching this minimum is $x_{\mathrm{P}} = 0.39$ based on the expression Eq. (5.5) for the density ρ. Ghoufi et al. obtained similar concentration dependence for the aqueous ethanol solution, but the alcohol concentration where the excess density reaches its minimum is slightly higher than 0.39.[159]

In contrast, the excess density $\rho_{\mathrm{ex}}(\phi_{\mathrm{P}})$ as a function of ϕ_{P} is positive and reaches a maximum at around $\phi_{\mathrm{P}} = 0.5$, as shown in Figure 5.8(b). The concentration of the maximum is $\phi_{\mathrm{P}} = 0.53$ based on Eq. (5.5). This volume fraction corresponds to the mole fraction $x_{\mathrm{P}} = 0.21$. Wensink et al. obtained similar trends for alcohol/water mixtures as a function of the mass percentage instead of the volume fraction.[149]

In summary, $x_{\mathrm{P}} = 0.39$ and 0.21 are singular points for the mole and volume fraction dependencies of the excess densities of the aqueous 1-propanol solution, respectively.

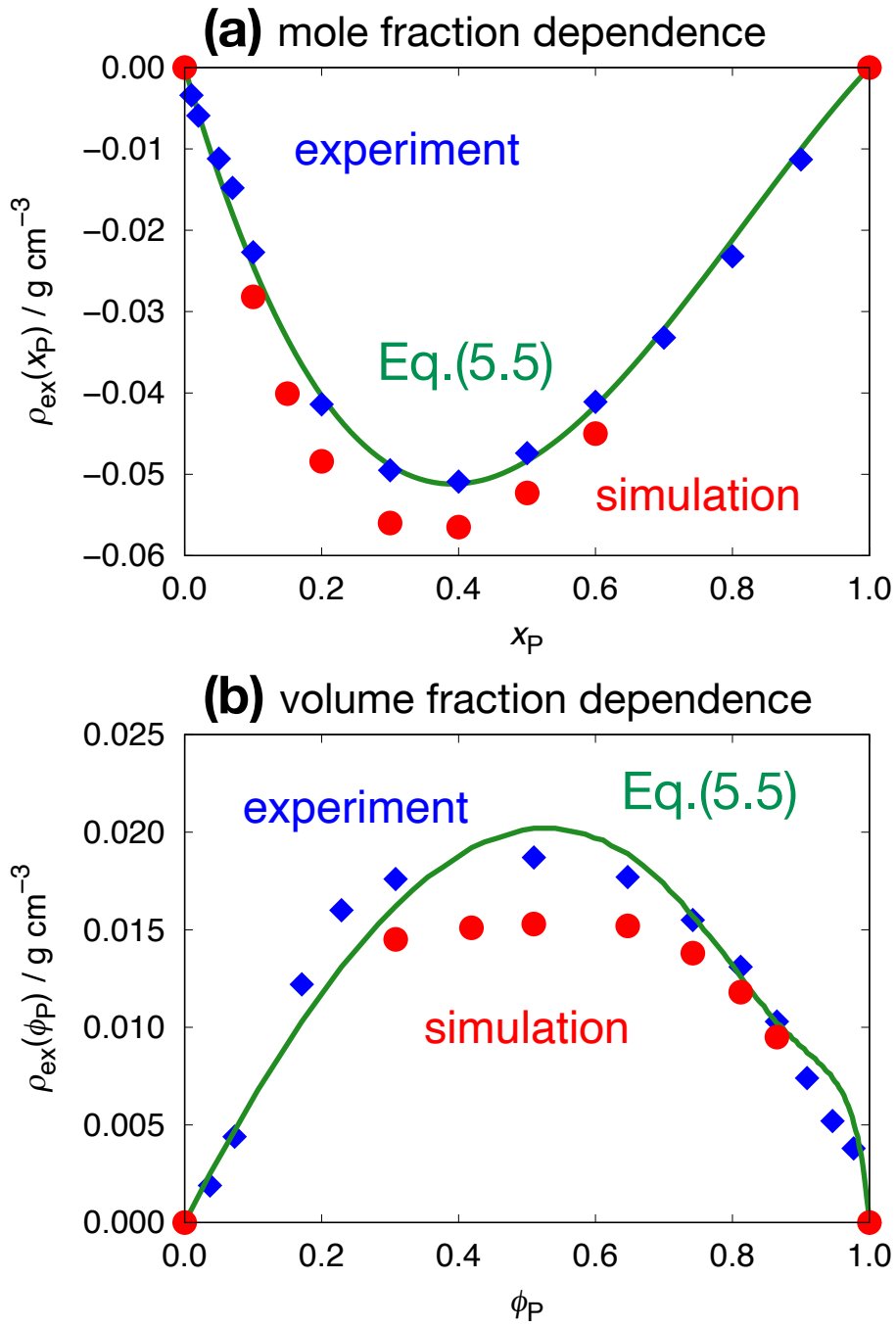

Figure 5.8: Concentration dependence of the excess densities of 1-propanol/water mixture. (a) The excess density $\rho_{ex}(x_P)$ defined by Eq. (5.6) as a function of x_P. (b) The excess density $\rho_{ex}(\phi_P)$ defined by Eq. (5.7) as a function of ϕ_P. Red circles represent the results obtained from the MD simulation. Table 5.1 shows the simulation data of ρ, ρ_P, and ρ_W in Eqs. (5.6) and (5.7). Blue diamonds and green lines are the results obtained from the experimental values[172] and Eq. (5.5), respectively.

These values are close to the concentrations at which the percolation transitions by water and 1-propanol independently occur, as shown in Figure 5.6.

5.4 CONCLUSIONS

We performed molecular dynamics simulations of aqueous 1-propanol solutions with different concentrations x_{P} and clarified the specific nature of the hydrophobic interaction between the carbon chains of 1-propanol molecules.

The first peak height of the radial distribution function $g_{\mathrm{CC}}(r)$ for pairs of terminal carbon atoms of 1-propanol molecules decreases with increasing x_{P}. This trend is opposite to the x_{P} dependence of the peak height of $g_{\mathrm{PP}}(r)$ for pairs of oxygen atoms of 1-propanol. The hydrophobic interaction is thus more dominant than the hydrogen bonding for the effective interaction between 1-propanol molecules in the aqueous solution with low x_{P}. The distribution functions in the mixtures of $x_{\mathrm{P}} = 0.1$, 0.15, and 0.2 deviate from 1 even at long distances r, indicating the concentration heterogeneity on nanometer-length scales.

The number distribution $n_{\mathrm{P}}(s)$ of clusters due to the hydrophobic interaction indicates that 1-propanol molecules form a percolation cluster in the solutions with $x_{\mathrm{P}} \geq 0.15$. The concentration of the percolation transition is significantly lower than that in the hypothetical two-component system. In contrast, $n_{\mathrm{W}}(s)$ of the hydrogen-bonding clusters of water molecules in the 1-propanol/water mixture does not differ from the number distribution in the hypothetical system.

The concentration dependence of the percolation probability $\langle P \rangle$ shows that the percolation transition occurs at $x_{\mathrm{P}} = 0.15$ due to the hydrophobic interaction between 1-propanol molecules and at $x_{\mathrm{P}} = 0.5$ due to the hydrogen bond between water molecules. $x_{\mathrm{P}} = 0.15$ and 0.5 are close to the concentrations at which the Kirkwood-Buff integrals,[128] the dielectric relaxation time,[135] and the excess densities (Figure 5.8) take maximum or minimum against x_{P}. The percolation transition would thus be related to the changes in the concentration fluctuation and the mixed state of the aqueous 1-propanol solution.

The present investigation highlights the importance of hydrophobic interactions be-

tween alcohol molecules for the clustering and percolation in alcohol/water mixtures. We should examine other aqueous solutions of alcohols, such as methanol and ethanol, to clarify the effects of carbon chain size and length on the clustering in these mixtures. The temperature effect on the mixed state of the solutions is, of course, an important subject. The experimental study also shows that 1-propanol and water are phase-separated due to the addition of sodium or potassium chloride into the mixture.[188] Based on these comprehensive works, we would gain a better understanding of hydrophobic interactions between alcohol molecules in the aqueous solutions.

List of Publications

1. Hidefumi Naito, Ryuichi Okamoto, Tomonari Sumi, and Kenichiro Koga, "Osmotic second virial coefficients for hydrophobic interactions as a function of solute size", *The Journal of Chemical Physics*, 2022, **156**, 221104 (5 pages).

2. Hidefumi Naito, Tomonari Sumi, and Kenichiro Koga, "How do water-mediated interactions and osmotic second virial coefficients vary with particle size?", *Faraday Discussions*, 2024, **249**, 440-452.

3. Hidefumi Naito, Tomonari Sumi, and Kenichiro Koga, "The nature of the hydrophobic interaction varies as the solute size increases from methane's to C_{60}'s", *The Journal of Chemical Physics*, 2024, **161**, 214501 (14 pages).

Acknowledgments

This work was supported by JST (Japan Science and Technology Agency), the establishment of university fellowships towards the creation of science technology innovation, Grant Number JPMJFS2128, and by JST SPRING (Support for Pioneering Research Initiated by the Next Generation), Grant Number JPMJSP2126. Part of the computation was performed at the Research Center for Computational Science, Okazaki, Japan (Project: 21-IMS-C125, 22-IMS-C124, 23-IMS-C112, 24-IMS-C106).

Chapter 1 was reproduced from "H. Naito, T. Sumi, and K. Koga, *Faraday Discuss.*, Vol. 249, doi: 10.1039/d3fd00104k (2024)" with permission of the Royal Society of Chemistry. Chapter 2 was reproduced from "H. Naito, T. Sumi, and K. Koga, *J. Chem. Phys.*, Vol. 161, doi: 10.1063/5.0233808 (2024)" with the permission of AIP Publishing.

I am deeply grateful to my supervisor, Professor Kenichiro Koga. His suggestions and comments have always been valuable in advancing my study. We mainly prepared the manuscripts of the three publications listed on the previous page.

I would like to thank Professor Tomonari Sumi of the Muroran Institute of Technology. Discussing the results obtained from molecular simulation and integral equation theory with him was informative.

Acknowledgment should be expressed to Specially Appointed Associate Professor Ryuichi Okamoto of the University of Hyogo. The discovery of the power-law relationship between the osmotic B and the solute diameter σ was based on his theoretical study.

I wish to thank all the former and present members of the Theoretical Physical Chemistry Group, Department of Chemistry, for their constructive advice and frank discussions. They also helped me to learn physics, statistical mechanics, and thermodynamics.

I am also grateful to Sanae Furuta, the secretary of our research group. She has supported me in submitting the documents and applying for the expenses related to the academic conference.

Finally, I express my most heartfelt thanks to my father, Kazuyuki Naito, my mother, Kaori Naito, and my sister, Sae Naito, for their continuous help in my daily life.

Okayama

March 2025

Hidefumi Naito

References

[1] A. Ben-Naim, *Solvent-Induced Interactions and Forces in Protein Folding: Hydrophobic-Hydrophilic Phenomena*, Springer Nature, 2023.

[2] W. Kauzmann, *Adv. Protein Chem.*, 1959, **14**, 1–63.

[3] K. Lum, D. Chandler, and J. D. Weeks, *J. Phys. Chem. B*, 1999, **103**(22), 4570–4577.

[4] E. Sobolewski, M. Makowski, C. Czaplewski, A. Liwo, S. Ołdziej, and H. A. Scheraga, *J. Phys. Chem. B*, 2007, **111**(36), 10765–10774.

[5] M. Makowski, C. Czaplewski, A. Liwo, and H. A. Scheraga, *J. Phys. Chem. B*, 2010, **114**(2), 993–1003.

[6] R. Zangi, *J. Phys. Chem. B*, 2011, **115**(10), 2303–2311.

[7] J. G. Kirkwood and F. P. Buff, *J. Chem. Phys.*, 1951, **19**(6), 774–777.

[8] A. Ben-Naim, *Molecular theory of solutions*, OUP Oxford, 2006.

[9] W. G. McMillan Jr and J. E. Mayer, *J. Chem. Phys.*, 1945, **13**(7), 276–305.

[10] K. Koga, V. Holten, and B. Widom, *J. Phys. Chem. B*, 2015, **119**(42), 13391–13397.

[11] M. Kinoshita, *J. Chem. Phys.*, 2003, **118**(19), 8969–8981.

[12] S. Asakura and F. Oosawa, *J. Chem. Phys.*, 1954, **22**(7), 1255–1256.

[13] T. Boublík, *J. Chem. Phys.*, 1970, **53**(1), 471–472.

[14] G. A. Mansoori, N. F. Carnahan, K. E. Starling, and T. W. Leland Jr, *J. Chem. Phys.*, 1971, **54**(4), 1523–1525.

[15] D. Chandler, *Nature*, 2005, **437**(7059), 640–647.

[16] D. Ben-Amotz, *J. Phys. Chem. Lett.*, 2015, **6**(9), 1696–1701.

[17] D. Ben-Amotz, *Annu. Rev. Phys. Chem.*, 2016, **67**, 617–638.

[18] L. R. Pratt, M. I. Chaudhari, and S. B. Rempe, *J. Phys. Chem. B*, 2016, **120**(27), 6455–6460.

[19] K. Koga, *J. Phys. Chem. B*, 2013, **117**(41), 12619–12624.

[20] K. Koga and B. Widom, *J. Chem. Phys.*, 2013, **138**(11), 114504.

[21] K. Koga and N. Yamamoto, *J. Phys. Chem. B*, 2018, **122**(13), 3655–3665.

[22] M. I. Chaudhari, S. A. Holleran, H. S. Ashbaugh, and L. R. Pratt, *Proc. Natl. Acad. Sci. U.S.A.*, 2013, **110**(51), 20557–20562.

[23] M. I. Chaudhari, D. Sabo, L. R. Pratt, and S. B. Rempe, *J. Phys. Chem. B*, 2015, **119**(29), 9098–9102.

[24] M. I. Chaudhari, S. B. Rempe, D. Asthagiri, L. Tan, and L. R. Pratt, *J. Phys. Chem. B*, 2016, **120**(8), 1864–1870.

[25] H. S. Ashbaugh, K. Weiss, S. M. Williams, B. Meng, and L. N. Surampudi, *J. Phys. Chem. B*, 2015, **119**(20), 6280–6294.

[26] D. Tang, C. Delpo, O. Blackmon, and H. S. Ashbaugh, *J. Chem. Phys.*, 2018, **148**(1), 016101.

[27] B. Widom and R. C. Underwood, *J. Phys. Chem. B*, 2012, **116**(31), 9492–9499.

[28] C. A. Cerdeiriña and B. Widom, *J. Phys. Chem. B*, 2016, **120**(51), 13144–13151.

[29] R. Okamoto and A. Onuki, *J. Chem. Phys.*, 2018, **149**(1), 014501.

[30] R. Okamoto, K. Koga, and A. Onuki, *J. Chem. Phys.*, 2020, **153**(7), 074503.

[31] R. Okamoto and K. Koga, *J. Phys. Chem. B*, 2021, **125**(46), 12820–12831.

[32] K. Koga, X. C. Zeng, and H. Tanaka, *J. Chem. Phys.*, 1997, **106**(23), 9781–9792.

[33] A. Bartosik, M. Wiśniewska, and M. Makowski, *J. Phys. Org. Chem.*, 2015, **28**(1), 10–16.

[34] A. S. Thomas and A. H. Elcock, *J. Phys. Chem. Lett.*, 2011, **2**(1), 19–24.

[35] P. Attard, *J. Chem. Phys.*, 1989, **91**(5), 3083–3089.

[36] T. Biben, P. Bladon, and D. Frenkel, *J. Phys.: Condens. Matter*, 1996, **8**(50), 10799–10821.

[37] R. Dickman, P. Attard, and V. Simonian, *J. Chem. Phys.*, 1997, **107**(1), 205–213.

[38] M. Dijkstra, R. van Roij, and R. Evans, *Phys. Rev. E*, 1999, **59**(5), 5744–5771.

[39] R. Roth, R. Evans, and S. Dietrich, *Phys. Rev. E*, 2000, **62**(4), 5360–5377.

[40] M. Kinoshita, *Chem. Phys. Lett.*, 2002, **353**(3-4), 259–269.

[41] R. Akiyama, Y. Karino, Y. Hagiwara, and M. Kinoshita, *J. Phys. Soc. Jpn.*, 2006, **75**(6), 064804.

[42] R. D. Mountain and D. Thirumalai, *Proc. Natl. Acad. Sci. U.S.A.*, 1998, **95**(15), 8436–8440.

[43] G. Graziano, *J. Chem. Soc., Faraday Trans.*, 1998, **94**(22), 3345–3352.

[44] G. Hummer and S. Garde, *Phys. Rev. Lett.*, 1998, **80**(19), 4193–4196.

[45] S. Rajamani, T. M. Truskett, and S. Garde, *Proc. Natl. Acad. Sci. U.S.A.*, 2005, **102**(27), 9475–9480.

[46] M. V. Athawale, S. N. Jamadagni, and S. Garde, *J. Chem. Phys.*, 2009, **131**(11), 115102.

[47] I. Sinha, S. M. Cramer, H. S. Ashbaugh, and S. Garde, *J. Phys. Chem. B*, 2022, **126**(39), 7604–7614.

[48] D. M. Huang, P. L. Geissler, and D. Chandler, *J. Phys. Chem. B*, 2001, **105**(28), 6704–6709.

[49] D. M. Huang and D. Chandler, *J. Phys. Chem. B*, 2002, **106**(8), 2047–2053.

[50] D. R. Weiss, T. M. Raschke, and M. Levitt, *J. Phys. Chem. B*, 2008, **112**(10), 2981–2990.

[51] A. L. Ferguson, P. G. Debenedetti, and A. Z. Panagiotopoulos, *J. Phys. Chem. B*, 2009, **113**(18), 6405–6414.

[52] V. Hande and S. Chakrabarty, *ACS Omega*, 2022, **7**(3), 2671–2678.

[53] J. L. F. Abascal and C. Vega, *J. Chem. Phys.*, 2005, **123**(23), 234505.

[54] J. D. Weeks, D. Chandler, and H. C. Andersen, *J. Chem. Phys.*, 1971, **54**(12), 5237–5247.

[55] M. G. Martin and J. I. Siepmann, *J. Phys. Chem. B*, 1998, **102**(14), 2569–2577.

[56] M. J. Abraham, T. Murtola, R. Schulz, S. Páll, J. C. Smith, B. Hess, and E. Lindahl, *SoftwareX*, 2015, **1–2**, 19–25.

[57] G. M. Torrie and J. P. Valleau, *Chem. Phys. Lett.*, 1974, **28**(4), 578–581.

[58] G. M. Torrie and J. P. Valleau, *J. Comput. Phys.*, 1977, **23**(2), 187–199.

[59] S. Kumar, D. Bouzida, R. H. Swendsen, P. A. Kollman, and J. M. Rosenberg, *J. Comput. Chem.*, 1992, **13**(8), 1011–1021.

[60] M. Souaille and B. Roux, *Comput. Phys. Commun.*, 2001, **135**(1), 40–57.

[61] J. J. Nicolas, K. E. Gubbins, W. B. Streett, and D. J. Tildesley, *Mol. Phys.*, 1979, **37**(5), 1429–1454.

[62] Y. Kimura and Y. Yoshimura, *Mol. Phys.*, 1991, **72**(2), 279–294.

[63] P. Krüger, S. K. Schnell, D. Bedeaux, S. Kjelstrup, T. J. H. Vlugt, and J.-M. Simon, *J. Phys. Chem. Lett.*, 2013, **4**(2), 235–238.

[64] N. Dawass, P. Krüger, S. K. Schnell, O. A. Moultos, I. G. Economou, T. J. H. Vlugt, and J.-M. Simon, *Nanomaterials*, 2020, **10**(4), 771.

[65] H. Naito, T. Sumi, and K. Koga, *Faraday Discuss.*, 2024, **249**, 440–452.

[66] G. Graziano, *Chem. Phys. Lett.*, 2010, **499**(1-3), 79–82.

[67] G. Graziano, *Chem. Phys. Lett.*, 2017, **685**, 54–59.

[68] L. R. Pratt and D. Chandler, *J. Chem. Phys.*, 1980, **73**(7), 3434–3441.

[69] D. Asthagiri, S. Merchant, and L. R. Pratt, *J. Chem. Phys.*, 2008, **128**(24), 244512.

[70] A. Gao, L. Tan, M. I. Chaudhari, D. Asthagiri, L. R. Pratt, S. B. Rempe, and J. D. Weeks, *J. Phys. Chem. B*, 2018, **122**(23), 6272–6276.

[71] K. Watanabe and H. C. Andersen, *J. Phys. Chem.*, 1986, **90**(5), 795–802.

[72] L. Li, D. Bedrov, and G. D. Smith, *Phys. Rev. E*, 2005, **71**(1), 011502.

[73] T. Sumi and H. Sekino, *J. Chem. Phys.*, 2007, **126**(14), 144508.

[74] T. Sumi and K. Koga, *Sci. Rep.*, 2019, **9**(1), 1–9.

[75] T. Sumi and H. Imamura, *Protein Sci.*, 2021, **30**(10), 2132–2143.

[76] H. Naito, R. Okamoto, T. Sumi, and K. Koga, *J. Chem. Phys.*, 2022, **156**(22), 221104.

[77] L. R. Pratt and D. Chandler, *J. Chem. Phys.*, 1977, **67**(8), 3683–3704.

[78] D. E. Smith and A. D. J. Haymet, *J. Chem. Phys.*, 1993, **98**(8), 6445–6454.

[79] P. Jungwirth and R. Zahradník, *Chem. Phys. Lett.*, 1994, **217**(3), 319–324.

[80] S. W. Rick and B. J. Berne, *J. Phys. Chem. B*, 1997, **101**(49), 10488–10493.

[81] S. W. Rick, *J. Phys. Chem. B*, 2003, **107**(36), 9853–9857.

[82] S. Shimizu and H. S. Chan, *J. Chem. Phys.*, 2000, **113**(11), 4683–4700.

[83] S. Shimizu and H. S. Chan, *J. Am. Chem. Soc.*, 2001, **123**(9), 2083–2084.

[84] D. Paschek, *J. Chem. Phys.*, 2004, **120**(14), 6674–6690.

[85] D. Paschek, *J. Chem. Phys.*, 2004, **120**(22), 10605–10617.

[86] L. Li, D. Bedrov, and G. D. Smith, *J. Chem. Phys.*, 2005, **123**(20), 204504.

[87] G. Graziano, *J. Phys. Chem. B*, 2009, **113**(32), 11232–11239.

[88] G. Graziano, *J. Phys. Soc. Jpn.*, 2016, **85**(2), 024801.

[89] K. Zieba, C. Czaplewski, A. Liwo, and G. Graziano, *Phys. Chem. Chem. Phys.*, 2020, **22**(8), 4758–4771.

[90] R. Zangi and B. J. Berne, *J. Phys. Chem. B*, 2008, **112**(29), 8634–8644.

[91] M. Bogunia, A. Liwo, C. Czaplewski, J. Makowska, A. Giełdoń, and M. Makowski, *J. Phys. Chem. B*, 2022, **126**(3), 634–642.

[92] J. Engstler and N. Giovambattista, *J. Phys. Chem. B*, 2018, **122**(38), 8908–8920.

[93] D. E. Smith, L. Zhang, and A. D. J. Haymet, *J. Am. Chem. Soc.*, 1992, **114**(14), 5875–5876.

[94] A. D. J. Haymet, K. A. T. Silverstein, and K. A. Dill, *Faraday Discuss.*, 1996, **103**, 117–124.

[95] S. W. Rick, *J. Phys. Chem. B*, 2000, **104**(29), 6884–6888.

[96] J. J. Kozak, W. S. Knight, and W. Kauzmann, *J. Chem. Phys.*, 1968, **48**(2), 675–690.

[97] H. Tanaka, *J. Chem. Phys.*, 1987, **86**(3), 1512–1520.

[98] G. Hummer, S. Garde, A. E. Garcia, A. Pohorille, and L. R. Pratt, *Proc. Natl. Acad. Sci. U.S.A.*, 1996, **93**(17), 8951–8955.

[99] N. T. Southall and K. A. Dill, *Biophys. Chem.*, 2002, **101–102**, 295–307.

[100] M. Bogunia and M. Makowski, *J. Phys. Chem. B*, 2020, **124**(46), 10326–10336.

[101] A. Luzar and D. Chandler, *Phys. Rev. Lett.*, 1996, **76**(6), 928–931.

[102] A. K. Soper and M. G. Phillips, *Chem. Phys.*, 1986, **107**(1), 47–60.

[103] J. Teixeira, M.-C. Bellissent-Funel, and S.-H. Chen, *J. Phys.: Condens. Matter*, 1990, **2**(S), SA105–SA108.

[104] K. Koga, *J. Chem. Phys.*, 2002, **116**(24), 10882–10889.

[105] K. Koga and H. Tanaka, *J. Chem. Phys.*, 2005, **122**(10), 104711.

[106] F. Leoni, C. Calero, and G. Franzese, *ACS Nano*, 2021, **15**(12), 19864–19876.

[107] Q. Sun, X. W. Su, and C. B. Cheng, *Chem. Phys.*, 2019, **516**, 199–205.

[108] K. Miyazaki, K. S. Schweizer, D. Thirumalai, R. Tuinier, and E. Zaccarelli, *J. Chem. Phys.*, 2022, **156**(8), 080401.

[109] P. Attard and G. N. Patey, *J. Chem. Phys.*, 1990, **92**(8), 4970–4982.

[110] R. Roth and M. Kinoshita, *J. Chem. Phys.*, 2006, **125**(8), 084910.

[111] J.-P. Simonin, *J. Phys. Chem. B*, 2001, **105**(22), 5262–5270.

[112] C. Barrio and J. R. Solana, *J. Chem. Phys.*, 2000, **113**(22), 10180–10185.

[113] H. Naito, T. Sumi, and K. Koga, *J. Chem. Phys.*, 2024, **161**(21), 214501.

[114] S. Lüdemann, R. Abseher, H. Schreiber, and O. Steinhauser, *J. Am. Chem. Soc.*, 1997, **119**(18), 4206–4213.

[115] A. A. Chialvo and O. D. Crisalle, *J. Chem. Phys.*, 2019, **150**(12), 124503.

[116] J.-P. Hansen and I. R. McDonald, *Theory of Simple Liquids: with Applications to Soft Matter*, Academic Press, 2013.

[117] J. L. Lebowitz, *Phys. Rev.*, 1964, **133**(4A), A895–A899.

[118] D. Henderson and M. Lozada-Cassou, *J. Colloid Interface Sci.*, 1986, **114**(1), 180–183.

[119] D. Henderson, *J. Colloid Interface Sci.*, 1988, **121**(2), 486–490.

[120] Y. Nakamura, S. Arai, M. Kinoshita, A. Yoshimori, and R. Akiyama, *J. Chem. Phys.*, 2019, **151**(4), 044506.

[121] L. Verlet, *Mol. Phys.*, 1980, **41**(1), 183–190.

[122] M. Matsuo, Y. Nakamura, M. Kinoshita, and R. Akiyama, *Physica A*, 2024, **644**(15), 129846.

[123] T. Head-Gordon and G. Hura, *Chem. Rev.*, 2002, **102**(8), 2651–2670.

[124] Y. Mao, M. E. Cates, and H. N. W. Lekkerkerker, *Physica A*, 1995, **222**(1-4), 10–24.

[125] A. Bansal, A. J. Schultz, and D. A. Kofke, *J. Phys. Chem. B*, 2021, **125**(26), 7262–7272.

[126] E. P. Bernard, W. Krauth, and D. B. Wilson, *Phys. Rev. E*, 2009, **80**(5), 056704.

[127] K. Nishikawa, Y. Kodera, and T. Iijima, *J. Phys. Chem.*, 1987, **91**(13), 3694–3699.

[128] H. Hayashi, K. Nishikawa, and T. Iijima, *J. Phys. Chem.*, 1990, **94**(21), 8334–8338.

[129] K. Nishikawa and T. Iijima, *J. Phys. Chem.*, 1993, **97**(41), 10824–10828.

[130] H. Hayashi and Y. Udagawa, *Bull. Chem. Soc. Jpn.*, 1992, **65**(1), 155–159.

[131] T. Takamuku, H. Maruyama, K. Watanabe, and T. Yamaguchi, *J. Solution Chem.*, 2004, **33**(6), 641–660.

[132] K. Yoshida and T. Yamaguchi, *Z. Naturforsch.*, 2001, **56**(8), 529–536.

[133] T. Sato, A. Chiba, and R. Nozaki, *J. Chem. Phys.*, 1999, **110**(5), 2508–2521.

[134] T. Sato, A. Chiba, and R. Nozaki, *J. Chem. Phys.*, 2000, **112**(6), 2924–2932.

[135] T. Sato, A. Chiba, and R. Nozaki, *J. Chem. Phys.*, 2000, **113**(21), 9748–9758.

[136] T. Sato, A. Chiba, and R. Nozaki, *J. Mol. Liq.*, 2002, **101**(1-3), 99–111.

[137] M. Brai and U. Kaatze, *J. Phys. Chem.*, 1992, **96**(22), 8946–8955.

[138] R. Li, C. D'Agostino, J. McGregor, M. D. Mantle, J. A. Zeitler, and L. F. Gladden, *J. Phys. Chem. B*, 2014, **118**(34), 10156–10166.

[139] R. F. Lama and B. C.-Y. Lu, *J. Chem. Eng. Data*, 1965, **10**(3), 216–219.

[140] G. C. Benson and O. Kiyohara, *J. Solution Chem.*, 1980, **9**(10), 791–804.

[141] G. C. Benson, P. J. D'Arcy, and O. Kiyohara, *J. Solution Chem.*, 1980, **9**(12), 931–938.

[142] O. Kiyohara and G. C. Benson, *J. Solution Chem.*, 1981, **10**(4), 281–290.

[143] H. Ogawa and S. Murakami, *Thermochimica Acta*, 1986, **109**(1), 145–154.

[144] S. H. Tanaka, H. I. Yoshihara, A. W.-C. Ho, F. W. Lau, P. Westh, and Y. Koga, *Can. J. Chem.*, 1996, **74**(5), 713–721.

[145] K. Zemánková, J. Troncoso, C. A. Cerdeiriña, L. Romaní, and M. A. Anisimov, *Chem. Phys.*, 2016, **472**, 36–43.

[146] E. Matteoli and L. Lepori, *J. Chem. Phys.*, 1984, **80**(6), 2856–2863.

[147] I. Shulgin and E. Ruckenstein, *J. Phys. Chem. B*, 1999, **103**(5), 872–877.

[148] I. Shulgin and E. Ruckenstein, *J. Phys. Chem. B*, 1999, **103**(13), 2496–2503.

[149] E. J. W. Wensink, A. C. Hoffmann, P. J. van Maaren, and D. van der Spoel, *J. Chem. Phys.*, 2003, **119**(14), 7308–7317.

[150] A. Perera and B. Kežić, *Faraday Discuss.*, 2013, **167**, 145–158.

[151] M. Požar, B. Lovrinčević, L. Zoranić, T. Primorać, F. Sokolić, and A. Perera, *Phys. Chem. Chem. Phys.*, 2016, **18**(34), 23971–23979.

[152] A. Perera, *Pure Appl. Chem.*, 2016, **88**(3), 189–206.

[153] A. Perera, *Phys. Chem. Chem. Phys.*, 2017, **19**(41), 28275–28285.

[154] S. D. Overduin, A. Perera, and G. N. Patey, *J. Chem. Phys.*, 2019, **150**(18), 184504.

[155] M. Ogawa, Y. Ishii, and N. Ohtori, *Chem. Lett.*, 2016, **45**(1), 98–100.

[156] A. B. Roney, B. Space, E. W. Castner, R. L. Napoleon, and P. B. Moore, *J. Phys. Chem. B*, 2004, **108**(22), 7389–7401.

[157] S. K. Allison, J. P. Fox, R. Hargreaves, and S. P. Bates, *Phys. Rev. B*, 2005, **71**(2), 024201.

[158] J. A. B. da Silva, F. G. B. Moreira, V. M. L. dos Santos, and R. L. Longo, *Phys. Chem. Chem. Phys.*, 2011, **13**(14), 6452–6461.

[159] A. Ghoufi, F. Artzner, and P. Malfreyt, *J. Phys. Chem. B*, 2016, **120**(4), 793–802.

[160] O. Gereben and L. Pusztai, *Chem. Phys.*, 2017, **496**, 1–8.

[161] S. Pothoczki, L. Pusztai, and I. Bakó, *J. Phys. Chem. B*, 2019, **123**(35), 7599–7610.

[162] S. Choi, S. Parameswaran, and J.-H. Choi, *Phys. Chem. Chem. Phys.*, 2020, **22**(30), 17181–17195.

[163] S. Dixit, J. Crain, W. C. K. Poon, J. L. Finney, and A. K. Soper, *Nature*, 2002, **416**(6883), 829–832.

[164] L. Dougan, S. P. Bates, R. Hargreaves, J. P. Fox, J. Crain, J. L. Finney, V. Réat, and A. K. Soper, *J. Chem. Phys.*, 2004, **121**(13), 6456–6462.

[165] S. Lenton, N. H. Rhys, J. J. Towey, A. K. Soper, and L. Dougan, *J. Phys. Chem. B*, 2018, **122**(32), 7884–7894.

[166] I. Pethes, L. Pusztai, K. Ohara, S. Kohara, J. Darpentigny, and L. Temleitner, *J. Mol. Liq.*, 2020, **314**, 113664.

[167] S. Pothoczki, I. Pethes, L. Pusztai, L. Temleitner, K. Ohara, and I. Bakó, *J. Phys. Chem. B*, 2021, **125**(23), 6272–6279.

[168] S. Pothoczki, I. Pethes, L. Pusztai, L. Temleitner, D. Csókás, S. Kohara, K. Ohara, and I. Bakó, *J. Mol. Liq.*, 2021, **329**, 115592.

[169] I. Pethes, L. Pusztai, K. Ohara, and L. Temleitner, *J. Mol. Liq.*, 2021, **340**, 117188.

[170] K. Zemánková, J. Troncoso, C. A. Cerdeiriña, and L. Romaní, *Chem. Phys. Lett.*, 2015, **640**, 184–187.

[171] B. Chen, J. J. Potoff, and J. I. Siepmann, *J. Phys. Chem. B*, 2001, **105**(15), 3093–3104.

[172] F.-M. Pang, C.-E. Seng, T.-T. Teng, and M. H. Ibrahim, *J. Mol. Liq.*, 2007, **136**(1-2), 71–78.

[173] M. Sammalkorpi, S. Sanders, A. Z. Panagiotopoulos, M. Karttunen, and M. Haataja, *J. Phys. Chem. B*, 2011, **115**(6), 1403–1410.

[174] D. Stauffer and A. Aharony, *Introduction to Percolation Theory, 2nd Edition*, Taylor & Francis, 1992.

[175] N. Jan, *Physica A*, 1999, **266**(1-4), 72–75.

[176] I. Balberg, N. Binenbaum, and N. Wagner, *Phys. Rev. Lett.*, 1984, **52**(17), 1465–1468.

[177] A. L. R. Bug, S. A. Safran, G. S. Grest, and I. Webman, *Phys. Rev. Lett.*, 1985, **55**(18), 1896–1899.

[178] T. DeSimone, S. Demoulini, and R. M. Stratt, *J. Chem. Phys.*, 1986, **85**(1), 391–400.

[179] I. Balberg and N. Binenbaum, *Phys. Rev. A*, 1987, **35**(12), 5174–5177.

[180] N. A. Seaton and E. D. Glandt, *J. Chem. Phys.*, 1987, **86**(8), 4668–4677.

[181] D. M. Heyes and J. R. Melrose, *Mol. Phys.*, 1989, **66**(5), 1057–1074.

[182] L. V. Woodcock, *AIChE Journal*, 2012, **58**(5), 1610–1618.

[183] A. Oleinikova, I. Brovchenko, A. Geiger, and B. Guillot, *J. Chem. Phys.*, 2002, **117**(7), 3296–3304.

[184] I. Brovchenko, A. Geiger, and A. Oleinikova, *Phys. Chem. Chem. Phys.*, 2004, **6**(8), 1982–1987.

[185] L. Pártay and P. Jedlovszky, *J. Chem. Phys.*, 2005, **123**(2), 024502.

[186] L. B. Pártay, P. Jedlovszky, I. Brovchenko, and A. Oleinikova, *Phys. Chem. Chem. Phys.*, 2007, **9**(11), 1341–1346.

[187] D. A. McQuarrie and J. D. Simon, *Physical Chemistry: A Molecular Approach*, University Science Books Sausalito, California, 1997.

[188] V. Gomis, F. Ruiz, G. De Vera, E. López, and M. D. Saquete, *Fluid Phase Equilibria*, 1994, **98**, 141–147.